CONTROL AND OPERATION OF DC MICROGRID

LI ZHAN

PhD

The Hong Kong Polytechnic University

2025

The Hong Kong Polytechnic University

Department of Electrical and Electronic Engineering

Control and Operation of DC Microgrid

Li Zhan

A thesis submitted in partial fulfilment of the requirements for the degree of Doctor of Philosophy

July 2025

CERTIFICATE OF ORIGINALITY

I hereby declare that this thesis is my own work and that, to the best of my knowledge and belief, it reproduces no material previously published or written, nor material that has been accepted for the award of any other degree or diploma, except where due acknowledgement has been made in the text.

_____ (Signed)

Li Zhan (Name of student)

Abstract

As modern power systems incorporate increasing shares of renewable energy sources (RESs), the demand for flexible, efficient, and resilient power distribution architectures has grown accordingly. DC microgrids (DC MGs)—localized electrical grids that use direct current (DC) for power transmission and distribution—have attracted significant attention due to their reduced conversion losses, compatibility with DC-native sources and loads, and enhanced control performance. However, the intermittency of RESs, the destabilizing influence of constant power loads (CPLs), and harsh operational conditions, such as those encountered in marine environments, pose significant challenges to system stability. This thesis proposes robust nonlinear control architectures to address these challenges, aiming to maximize renewable energy harvesting while maintaining voltage stability under dynamic conditions.

First, an in-depth review of DC MG architectures and practical applications, which lays the theoretical and contextual groundwork for the nonlinear control methodologies developed in the subsequent chapters.

Second, a backstepping controller combined with a nonlinear disturbance observer (NDO) is developed for a novel PV-powered DC MG. This approach mitigates the negative impedance effects of CPLs and ensures maximum power point tracking (MPPT), even under variations in environmental irradiance and temperature. Based on maximum energy harvesting, the proposed controller performs a better dynamic response of bus voltage regulation compared to the traditional dual-PI controller.

Finally, a compound large-signal stabilizer integrating model predictive control (MPC) with high-order NDOs is designed for interleaved multilevel boost DC-DC converters (IMBDCs) in shipboard microgrids (SMGs). The controller addresses parameter drift caused by environmental stresses, achieving rapid voltage regulation (settling time <10 ms) and inter-phase current balancing under large CPL variations, with superior performance over conventional dual-PI controllers.

The proposed strategies are validated through simulations and real-time experiments, contributing to developing resilient, efficient DC MGs for critical applications such as marine electrification and sustainable data centers.

Publications arisen/arising from the thesis

Journal Papers:

1. **Z. Li**, J. Chen, K. Li, Z. Xu, Y. Liu and M. Wang, "Robust Model Predictive Control for Onboard Interleaved Multilevel Boost DC-DC Converter in DC Shipboard Microgrids," in IEEE Transactions on Transportation Electrification, vol. 11, no. 4, pp. 8876-8888, Aug. 2025.
2. J. Chai, M. Wang, **Z. Li** and Z. Xu, "Improved Super-Twisting Sliding Mode Control for Single-Phase T-Type Three-Level Converters Based on Fixed-Time Extended State Observer," in IEEE Transactions on Transportation Electrification, vol. 10, no. 3, pp. 5307-5317, Sept. 2024.
3. **Z. Li**, Z. Xu, S. Yan, and M. Wang, “Nonlinear Control of Interleaved Multilevel Boost Converter for Power Smoothed Maximum PV Energy Harvesting,” being submitted to CSEE Journal of Power and Energy Systems.

Conference Papers:

1. **Z. Li**, M. Wang, Z. Xu and G. Tang, "A comprehensive review of data centre integrated with renewable energy," 12th IET International Conference on Advances in Power System Control, Operation and Management (APSCOM 2022), Hybrid Conference, Hong Kong, China, 2022, pp. 374-379. **[*Best student paper*]**
2. G. Tang, H. Wu, Z. Xu and **Z. Li**, "Two-Stage Robust Optimization for Microgrid Dispatch with Uncertainties," 2023 6th International Conference on Energy, Electrical and Power Engineering (CEEPE), Guangzhou, China, 2023, pp. 497-502.

Acknowledgements

Hereby, I would like to express my deepest gratitude to all those who have supported and guided me throughout my doctoral journey. First and foremost, I am profoundly indebted to my supervisors, Prof. Zhao Xu and Prof. Minghao Wang, whose unwavering mentorship and expertise have been pivotal to the completion of my PhD.

Prof. Xu's dedication to fostering a collaborative academic environment left a lasting impact on my research development. Through meticulously organized monthly group meetings, Prof. Xu not only encouraged open dialogue but also created a rare and invaluable space for intellectual exchange across diverse research areas. Their rigorous feedback consistently identified critical gaps in my methodology and reasoning, challenging me to refine my ideas and approach problems with greater clarity and depth.

Equally instrumental was Prof. Wang, who served as both a mentor and a compass throughout my four-year doctoral journey. Prof. Wang's patience, insight, and unwavering support were evident in our countless discussions, where they guided me through the nuances of experimental design, theoretical analysis, and the broader research trajectory. His ability to balance high-level vision with meticulous attention to detail was invaluable in helping me navigate moments of uncertainty and ultimately shape my articles into their final form.

I am also deeply grateful to my colleagues and lab mates for their camaraderie and support. Their willingness to share knowledge, assist with experiments, and collaboratively troubleshoot challenges greatly enriched my research experience and exemplified the strength of teamwork in overcoming academic hurdles.

Finally, I owe an immeasurable debt of gratitude to my parents. Their unconditional financial and emotional support allowed me to pursue this journey with confidence. Their unwavering belief in my abilities, conveyed through countless calls and messages, became a cornerstone of my resilience.

Table of Contents

List of Figures

List of Tables

Chapter 1 Introduction

1.1 Background

The global energy sector is undergoing a structural transformation toward renewable energy integration, propelled by decarbonization mandates and especially breakthroughs in power electronics and other technologies. This transition is essential to limiting global warming to 1.5°C, in line with the targets set by the Paris Agreement. Global renewable capacity has reached 4448 GW by 2024, with solar PV and wind contributing 67.4% [1]. As illustrated in Fig. 1.1, according to the data from the International Renewable Energy Agency (IRNEA), renewable energy capacity has expanded by 585 GW in 2024, accounting for 92.5% of the global newly-installed power generation [2]. This corresponds to an unprecedented annual growth rate of 15.1%, marking a new record in the history of global renewable energy deployment.

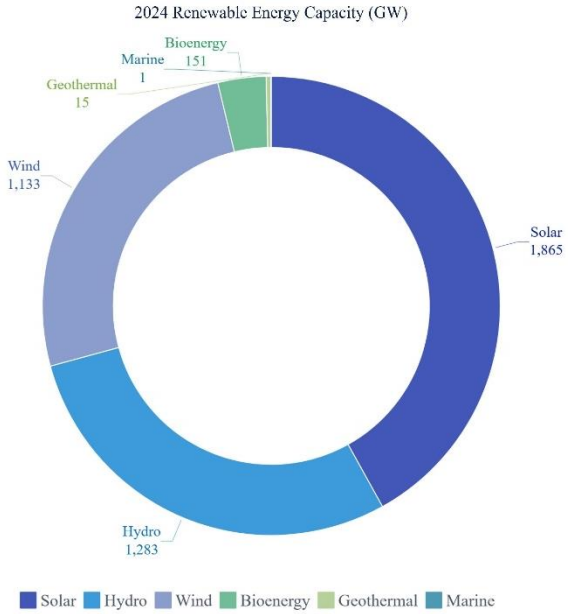

Fig. 1.1 2024 global renewable power capacity [1]

As shown in Fig. 1.2, solar and wind power continued to dominate the expansion of renewable energy in 2024, jointly contributing 96.6% of the newly-added renewable capacity. Among them, solar energy accounts for more than three-quarters of the total, with an additional 451.9 GW of installed capacity and a year-on-year

increase rate of 32.2%. This brought the global cumulative solar capacity to 1,865 GW. Wind energy capacity has been increased by 113 GW, which has an increase rate of 11.1% and leads to a total capacity of 1,133 GW [2].

As depicted in Fig. 1.3, renewable energy accounts for an increasing proportion of the total installed power capacity. By the end of 2024, renewable energy accounted for 46.4% of the global installed power capacity, almost half of the total installed power capacity [2]. According to the *Renewables 2024* report published by the International Energy Agency (IEA) [3], although the growth rate of renewable energy capacity slowed down slightly as compared to 2023, the absolute increased capacity has reached a new historical record. China played a vital role in this development, contributing 60% of the global increase in renewable energy capacity. The global expansion of renewable energy capacity can be attributed to three main factors: declining costs, supportive policy environments, and the growing influence of market mechanisms. In particular, the cost of PV generation continued to decrease due to historically low module prices. While policy remains the key driver of capacity additions, market-driven growth is becoming increasingly prominent [3]. Nevertheless, as illustrated in Fig. 1.4, significant regional disparities remain in the pace of renewable energy deployment. As in previous years, Asia contributed the largest share, with an increase of 421.5 GW in 2024, accounting for 72.0% of the global newly installed capacity. [2]

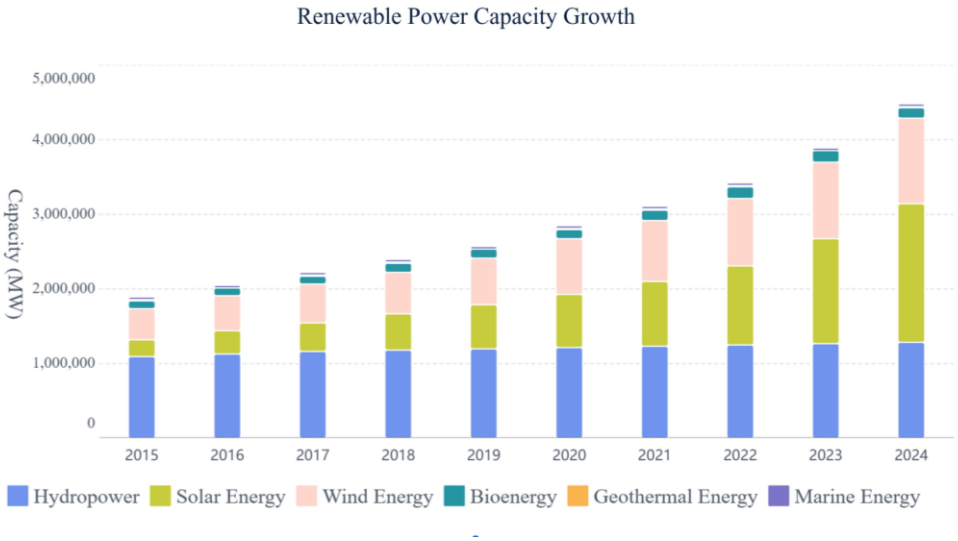

Fig. 1.2 Renewable power capacity growth (MW) [2]

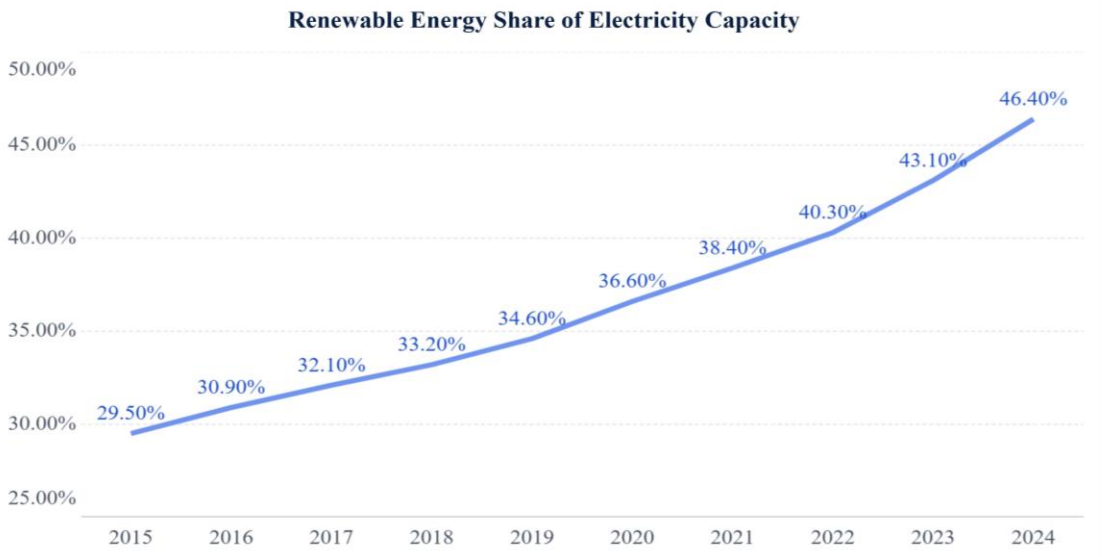

Fig. 1.3 Trend of the share of renewable energy in electricity capacity [2]

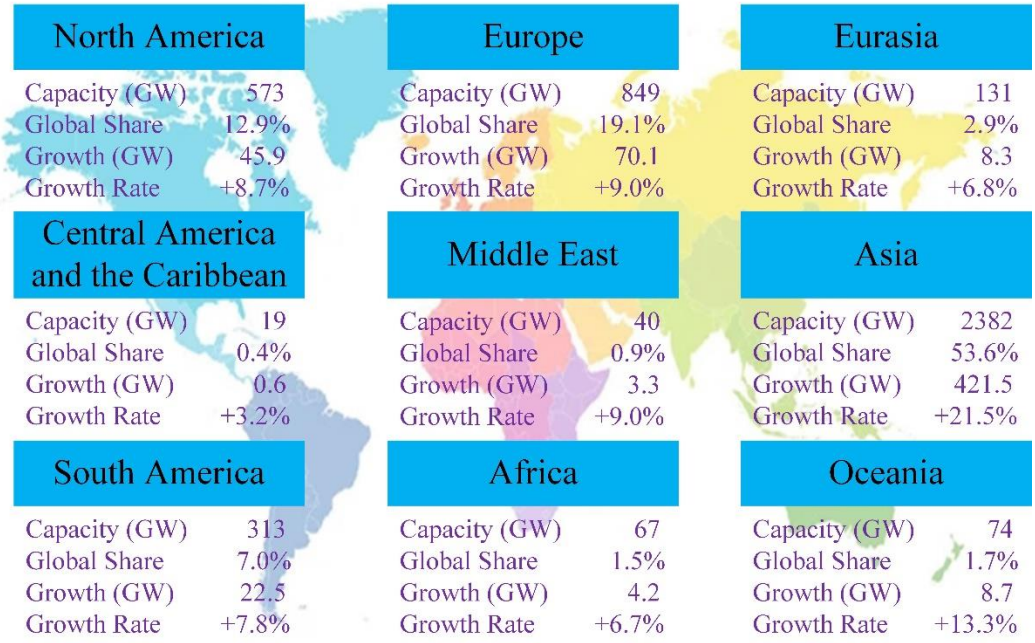

Fig. 1.4 Renewable generation capacity by region (GW) [2]

In summary, renewable energy generation has become deeply integrated into modern power grids, and its penetration is expected to continue increasing in the future. As a result, the substantial impact of renewable energy on grid operations cannot be overlooked.

As the penetration of renewable energy sources (RESs) continues to rise, there is a growing demand for more flexible, efficient, and resilient power distribution architectures. Microgrids, which are localized energy systems comprising distributed generation units (such as RESs), energy storage systems (ESSs), loads, energy

conversion interfaces, and some detection and protection devices, offer a promising solution to meet these evolving requirements. Among microgrids, DC microgrids (DC MGs) have gained increasing attention due to their inherent advantages over traditional AC microgrids. Unlike AC systems, which involve multiple conversion stages and suffer from issues such as reactive power flow, frequency regulation, and harmonic distortion, DC MGs feature a simplified structure with all components coupled directly to a common DC bus [4, 5]. This eliminates the need for frequency synchronization and minimizes power quality concerns, thereby significantly reducing control system complexity [6, 7]. Moreover, DC MGs exhibit higher efficiency and better compatibility with RESs like photovoltaic (PV) arrays and battery energy storage systems (BESSs), which naturally operate in DC [8]. They also interface more effectively with modern electronic loads and electric transportation systems. These benefits make DC MGs particularly well-suited for high-performance applications such as electric ships, data centers, and fast-charging stations, where space constraints, energy efficiency, and voltage stability are critical [9]. Given the increasing prevalence of RESs and the operational challenges they pose to conventional grid structures, DC MGs play a pivotal role within modern power systems, especially in scenarios that demand high power density and decentralized energy management [10].

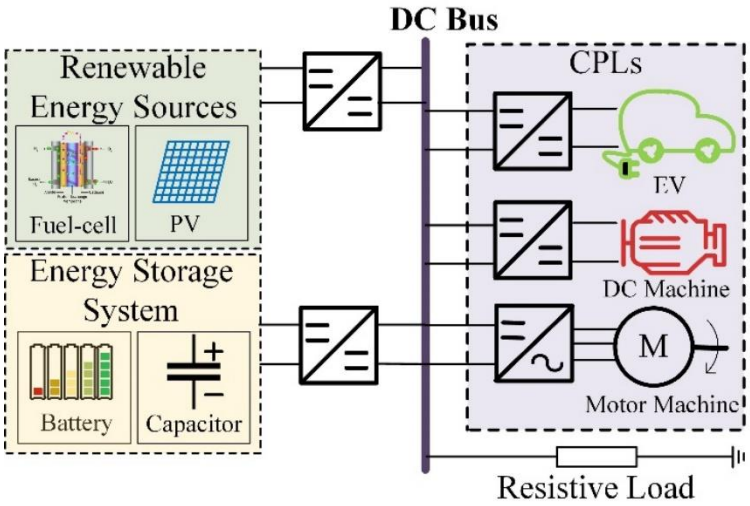

Fig. 1.5 A typical structure of the DC MG

A typical structure of DC MGs is depicted in Fig. 1.5. In order to promote DC MGs, several organizations are committed to developing practical standards, such as

ETSI EN 300 132-3-1 [11], MIL-STD-1399 [12], IEEE DC@Home [9], etc. However, due to the efficient DC converters, the applicable voltage range of DC MGs can be very wide. Typical voltage levels in DC MGs vary depending on application scenarios. For instance, 380 V is commonly adopted in data centers and commercial buildings, while higher levels such as 1,000 V or even up to 1,500 V are used in shipboard or transportation systems [9].

From a historical perspective, while AC microgrids have dominated due to the legacy of centralized AC systems, the growing prevalence of DC-native devices—including servers, LED lighting, and energy storage—has accelerated the adoption of DC MGs [13]. However, alongside these advantages, DC MGs face distinct challenges. One of the most critical issues is the integration of constant power loads (CPLs), which exhibit negative incremental impedance characteristics and can destabilize the voltage under sudden disturbances or faults. This problem is exacerbated by the stochastic and intermittent behavior of RESs, posing significant control and stability challenges, especially in mission-critical applications like data centers, where power quality requirements are extremely stringent [14, 15].

1.2 Research Motivations

With the growing deployment of RESs featuring DC output, the rapid increase in DC loads, and the extensive application of DC-based energy storage systems, DC power grids have garnered significant attention. Their advantages include the ease of integrating RESs and the improvement of overall system efficiency through simplified power conversion between generation and consumption. Despite these benefits, RESs, such as PV systems and wind turbines, are inherently intermittent and geographically distributed. Their power output is highly sensitive to environmental factors such as solar irradiance, ambient temperature, and wind speed. As a result, these sources exhibit stochastic and time-varying characteristics, often following diurnal and seasonal cycles. This variability poses considerable challenges to system stability analysis and the design of robust control strategies.

Another major challenge in DC MG operation stems from the increasing penetration of CPLs. These loads, which are typically regulated by tightly controlled power electronic converters, are commonly found in server farms, electric motor drives, and advanced battery management systems. While CPLs offer enhanced performance on the load side, they exhibit incremental negative impedance behavior. This characteristic can trigger adverse interactions with source-side converters, thereby compromising system stability. As illustrated in Fig. 1.6, the negative impedance profile of CPLs can significantly influence the dynamic response of the system, often resulting in voltage oscillations or even collapse during load transitions or periods of renewable source intermittency.

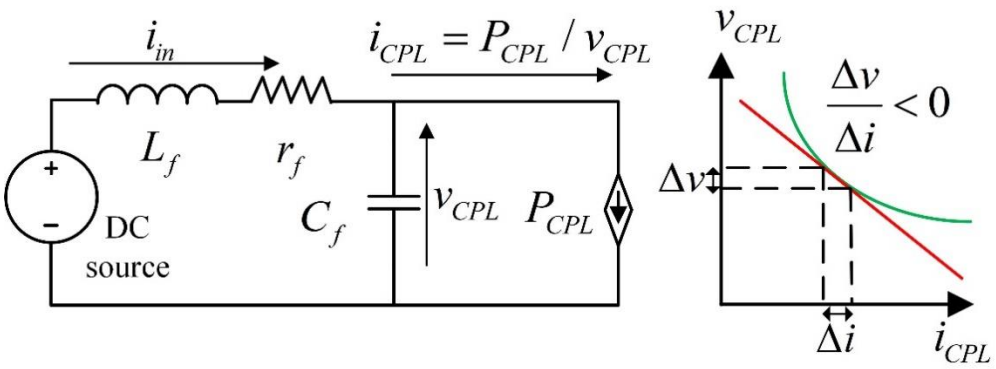

Fig. 1.6 Negative impedance characteristics of CPLs

Moreover, coordination between RESs and CPLs introduces further complexity. For example, maximum power point tracking (MPPT) algorithms for PV and wind systems must dynamically adjust to environmental variations to maximize energy harvest. However, these real-time adjustments interact nonlinearly with the negative impedance behavior of CPLs. The dynamic power demand fluctuations of CPLs can activate their inherent negative impedance characteristics, resulting in high-frequency oscillations in the DC bus voltage. Such voltage fluctuations cause the MPPT algorithms of PV or wind energy sources to deviate from their optimal operating points, significantly reducing the efficiency of renewable energy harvesting. As the energy output decreases, the system becomes less capable of meeting the power demands of CPLs, further exacerbating the bus voltage drop. This voltage decline, in turn, amplifies the negative impedance effect of the CPLs, forming a positive

feedback loop: the lower the voltage, the greater the reduction in system damping caused by the negative impedance, leading to more severe voltage oscillations.

This coupling effect becomes particularly detrimental when the source-load power exchange approaches the system's capacity limit. The interplay between continuous MPPT adjustments and growing voltage instability reinforces each other, eventually driving the system beyond its stability margin and potentially triggering protective mechanisms that force a shutdown. Without timely suppression through active control strategies, this feedback loop will inevitably lead to cascading failures, posing a serious threat to the operational reliability of the entire microgrid. Such issues become especially pronounced when source and load powers approach the system's capacity limit.

Traditional linear control strategies based on small signal models often fail to consider both stability and efficiency because they cannot cover the global dynamic characteristics. Furthermore, the deployment of DC MGs in harsh environments such as ships and offshore platforms has caused the above problems to deteriorate drastically due to hardware parameter drift and environmental interference. With the emphasis on electrification, more and more industries dominated by traditional energy sources are undergoing dramatic changes, with electric vehicles being a good example [16]. Taking the ship electrification system as an example, its special working conditions introduce multiple uncertainties:

- Salt spray and humidity in marine environments degrade insulation and cause considerable migrations in circuit inductance and capacitance.
- Mechanical vibrations lead to time-varying connection impedance in power devices, undermining the performance of controllers that rely on nominal parameters.

In a ship electrification system, conventional PID-based voltage regulators lack the robustness required to handle such large-signal disturbances and uncertainties. Recent advances in nonlinear control theory provide promising avenues to reconcile CPL stability with bus voltage regulation. Adding passive elements like resistors [17], capacitors [18], or LC filters [19] can significantly increase system damping when

using passive damping procedures. However, the incorporation of extra physical components can result in increased weight, expense, and potential loss, while damping is typically restricted by physical limitations.

Approaches leveraging sliding mode control [20], adaptive backstepping [21], and Takagi-Sugeno (TS) fuzzy control [22] have demonstrated improved transient response and large-signal stability margins. However, existing solutions often depend on accurate system modeling or impose restrictive operating constraints, limiting their practical implementation in DC MGs with variable sources and loads. This research gap motivates the development of enhanced nonlinear control architectures capable of maintaining voltage regulation without compromising CPL functionality, particularly under variations in environmental irradiance and temperature of PV arrays or sudden load change events.

1.3 Primary Contributions

Based on the current development on the control and operation of DC MGs with high renewables, the maximum energy acquisition of RESs in DC MGs is required while maintaining a reliable power supply to loads with satisfactory DC bus power quality. In addition, new robust control methods are needed in DC MGs to achieve the stability of the DC bus voltage with load changes or input voltage changes in harsh environments. To address these issues, novel and robust control methods based on observers are proposed in this thesis. The main contributions are summarized as follows.

- A comprehensive review of DC MG architectures and applications is first presented to establish the system-level context for the research. The discussion begins with a historical overview of microgrid evolution and continues with an in-depth classification of DC MG structures, including single-bus, multi-bus, and reconfigurable topologies. For each architecture, advantages, technical challenges, and typical application scenarios are analyzed based on recent literature and real-world deployments. Particular attention is given to emerging

use cases in data centers and shipboard electrical systems, where DC MGs can significantly improve energy efficiency and system integration. This review identifies key technical gaps, such as voltage instability under CPLs, that motivate the advanced nonlinear control methods explored in the following chapters.

- To ensure the stable power supply of loads while maximizing energy harvesting from PV systems, a backstepping controller combined with a nonlinear disturbance observer is designed to mitigate the negative impedance characteristics of the CPL. Even if some panels of the PV system experience variations in environmental irradiance and temperature or malfunction, the working point will change accordingly so that the system can obtain the maximum energy under that condition. Power deficits or surpluses are balanced by an energy storage system, ensuring a reliable supply to sensitive loads.
- A compound large-signal stabilizer is proposed for the Interleaved Multilevel Boost DC-DC Converter (IMBDC) to regulate the DC shipboard microgrids (DC SMGs) with high CPL penetration. The proposed method employs a high-order nonlinear disturbance observer to track real-time parameter variations caused by environmental stress (e.g., salt spray, mechanical vibration), effectively mitigating performance degradation due to line impedance drift. The IMBDC topology also facilitates efficient voltage boosting from RES inputs to load levels.

Finally, there are three publications derived from this thesis, including two journal articles and one conference paper. Please refer to the publication list for details.

Chapter 2 A Comprehensive Review of DC Microgrid Architectures and Applications

2.1 Introduction

The concept of the microgrid was first formally proposed in 2002 by Lasseter as a solution to enhance the reliability, flexibility, and efficiency of electric power systems in the face of increasing penetration of distributed energy resources (DERs) [23]. A microgrid refers to a localized energy system that can operate either connected to the main utility grid or in an islanded mode. The initial development focus was largely on AC microgrids, owing to the historical dominance of AC power infrastructure. AC equipment was already mature and widely available, and it was also easier to connect AC microgrids to the existing power grid.

AC microgrids gained significant attention and development during the early 2000s, primarily driven by the need to integrate variable renewable energy sources (RESs), improve power quality, and support grid resilience during outages [24-27]. This is due to the fact that AC microgrids can effectively integrate distributed generation and storage. Standardized control strategies, such as droop control and hierarchical energy management, enabled stable operation under both grid-tied and islanded conditions [25, 28-30]. However, as power electronic technologies advanced and the proportion of DC-native sources and loads grew rapidly, limitations of AC-based architectures began to emerge, such as frequent AC-DC and DC-AC conversions, synchronization challenges, and reactive power management.[4, 31]

In response, DC microgrids (DC MGs) have attracted growing interest over the past decade. With the increasing deployment of photovoltaic (PV) panels, battery energy storage systems (BESS), fuel cells, and constant power loads (CPLs) such as server farms and electric propulsion drives, DC MGs offer a more direct and efficient means of power distribution. One of the first DC MG topologies was proposed in 2004 for a 10kW DC MG-based distribution power generation system [32].

A typical DC MG consists of the following key components:

1) **Distributed generation (DG):** The DG units serve as the primary energy sources in the system. These commonly include PV panels, fuel cells, small-scale wind turbines connected via AC/DC rectifiers, and sometimes diesel generators interfaced through DC-DC converters. Among them, PV arrays are particularly well suited for DC MGs due to their inherently DC output, which reduces the need for intermediate conversion stages.
2) **Energy storage systems (ESSs):** The ESSs play a crucial role in balancing supply and demand, ensuring voltage stability, and enabling peak shaving or load leveling. Typical ESS configurations include lithium-ion batteries, flow batteries, or supercapacitors, which are interfaced with the DC bus through bidirectional DC-DC converters. These converters allow the ESS to both absorb excess energy during generation surpluses and release energy when the load exceeds generation, thereby supporting the microgrid's dynamic performance and resilience.
3) **DC loads:** DC loads are the primary energy consumers within the microgrid. These may include a wide range of equipment such as constant power loads (CPLs), electric vehicle chargers, LED lighting, HVAC systems with DC drives, and data center servers. Among them, due to CPL's negative incremental impedance characteristics, it is necessary to carefully design control and protection strategies to address particular stability challenges.
4) **Energy management system (EMS):** An intelligent and responsive EMS governs the microgrid's operational coordination. The EMS performs functions such as real-time power flow optimization, source and load scheduling, state-of-charge monitoring, and fault detection. In more advanced configurations, the EMS may also support islanding detection, black start capability, and demand response functions [33].

Given their advantages in efficiency, scalability, and compatibility with modern energy technologies, DC MGs are increasingly being adopted across a diverse range of application scenarios [34], such as Telecommunication stations [35, 36],

distributed generation [37], Electric Vehicle (EV) charging stations [38], commercial and residential houses [39], data centers [40], and maritime electric ships [41, 42].

In the field of data centers, DC MGs offer a streamlined power supply path to DC-native equipment such as servers, storage systems, and network devices, significantly reducing energy conversion losses and improving overall power utilization effectiveness. In remote or off-grid areas, particularly those relying on PV energy, islanded DC MGs provide a self-sufficient power solution by integrating PV arrays, ESSs, and local loads without the need for AC grid infrastructure. These systems often face unique control challenges due to source intermittency and the destabilizing influence of CPLs. Additionally, in maritime and shipboard environments, DC MGs are gaining prominence due to their reduced weight, compact form factor, and superior control precision—qualities that are critical for electric propulsion systems, onboard power distribution, and integration of renewable sources such as onboard solar. These varied application contexts, while distinct in their physical constraints and operational requirements, share a common need for high-performance control strategies to ensure voltage stability, efficient power sharing, and reliable operation under dynamic conditions. Accordingly, the remainder of this chapter will review representative use cases of DC MGs, laying the groundwork for the advanced control approaches presented in the subsequent chapters of this thesis.

2.2 Architectures of DC MGs

Many topologies have been reported in the literature, and this section will evaluate some of the most representative topologies. In general, DC MG topologies can be divided into three categories: single-bus topology, multi-bus topology, and reconfigurable topology [9].

2.2.1 Single-bus DC MGs

The single-bus architecture is the most fundamental and widely adopted configuration in small-scale DC MGs due to its simplicity and cost-effectiveness. As

shown in Fig. 2.1, a typical topology of a single bus DC MG with ESS is portrayed. In this topology, all DERs, ESSs, and loads are connected to a common DC bus. The bus typically operates at a fixed voltage level, which is maintained by regulating the output voltage of interfacing power electronic converters, such as DC-DC or DC-AC converters. These converters adjust their duty cycles or output references based on local measurements (e.g., bus voltage, current) and embedded control algorithms to stabilize the bus voltage under varying load and generation conditions [43-45].

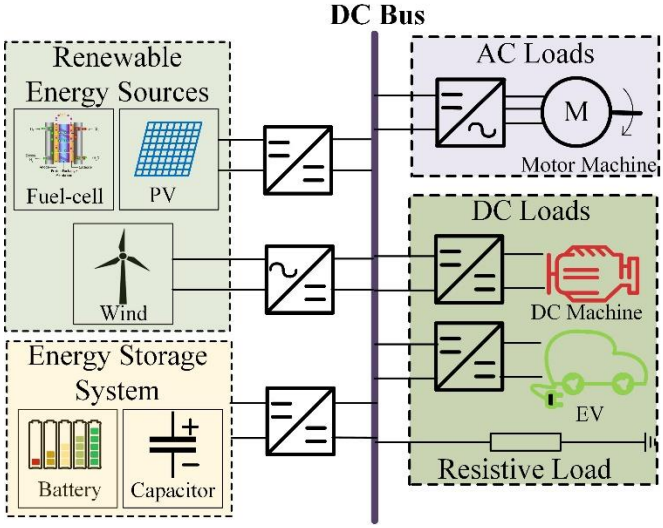

Fig. 2.1 A typical topology of a single-bus DC MG with ESS

The DC bus is typically maintained at standardized voltage levels such as 48 V or 380 V, depending on the application. This structure is especially popular in compact and cost-sensitive systems, such as telecom power supplies, where a 48 V nominal voltage has usually been adopted due to equipment compatibility and safety considerations [46].

The main advantage of the single-bus topology lies in its simplicity of design, minimal wiring requirements, and ease of integration with commercially available power converters.

However, several limitations hinder single-bus DC MGs' scalability and reliability in more demanding applications. First, the entire DC MG system depends on a single electrical backbone, which becomes a single point of failure and restricts fault isolation. Second, maintaining a tightly regulated DC bus voltage is challenging when multiple devices interact on the same bus, especially under dynamic load or

charging conditions. In practical deployments, batteries are often directly connected to the bus to serve as voltage anchors. However, fluctuations in the state of charge (SoC) and internal impedance of the batteries can cause deviations in the bus voltage, making precise voltage regulation difficult [47]. Moreover, in single-bus DC MGs where multiple converters operate in parallel to interface storage or distributed generation units, small discrepancies in voltage sensing or control loop tuning can lead to circulating currents, resulting in converter imbalance, localized overheating, and accelerated degradation of power components. These issues become more pronounced in long-duration islanded operation, where tight coordination is required between converters to avoid instability.

To address these challenges, researchers have proposed modified single-bus configurations, such as introducing dedicated converter interfaces between ESS and the bus, which decouple the bus voltage dynamics and allow for more flexible control strategies [48, 49]. Another enhancement is the bipolar single-bus topology. This structure provides dual voltage rails and enables load-side converters to select from positive, negative, or differential voltage references, thereby improving energy efficiency and load compatibility [50].

Despite these developments, the single-bus architecture remains inherently limited in terms of redundancy and adaptability. In response, more advanced multi-bus and reconfigurable topologies have been introduced to meet the growing demands for scalability, fault tolerance, and complex load management, as discussed in the following sections.

2.2.2 Multi-bus DC MGs

To overcome the scalability and fault-tolerance limitations of single-bus configurations, DC MGs can be structured into multi-bus architectures, where multiple independent DC buses (at potentially different voltage levels) are interconnected via dedicated converters, switches, or direct power cables [51]. As shown in Fig. 2.2, a multi-bus DC MG is connected via a bus converter. This modular

design enhances multi-bus DC MGs' availability, reliability, and robustness, particularly in mission-critical applications.

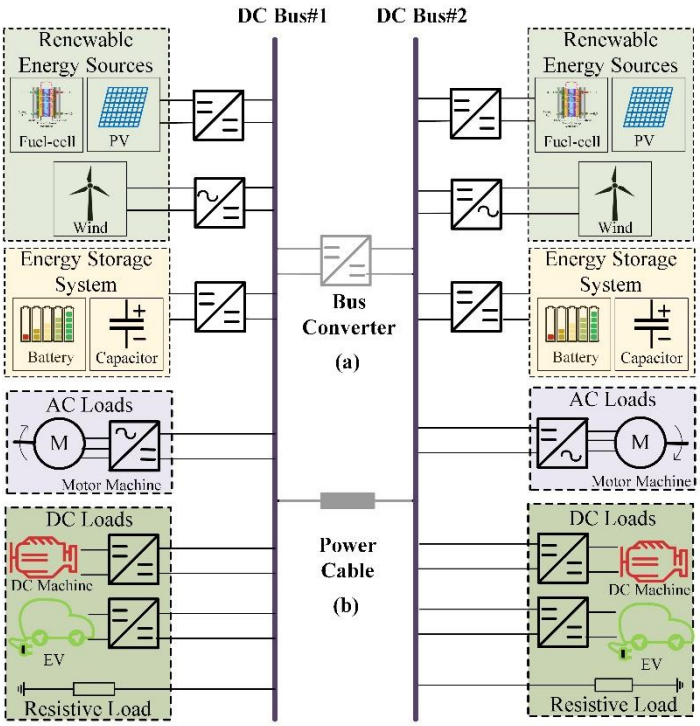

Fig. 2.2 A typical topology of a multi-bus DC MG. (a) different buses connected by DC-DC converters (b) different buses connected by power cables

In some configurations—particularly in industrial plants [52], transportation systems, or DC-powered campuses [53]—DC buses are connected through power cables that allow physical interconnection of multiple zones or subsystems [43]. These links enable power exchange, voltage support, or load sharing between buses without the need for full central coordination. Depending on the control scheme, these cable connections may be passive (e.g., via diode-based current routing) or actively managed through bidirectional converters. A notable example of passive redundancy is presented by Balog and Krein [53], who propose an automated hot-swap system between redundant buses using "auctioneering diodes" in a dual-bus setup. In this architecture, critical loads are equipped with diode-based interface circuits that automatically select the bus with the higher voltage. This ensures seamless switchover and sustained operation even if one bus fails or its voltage drops unexpectedly—an approach especially valuable in telecom or data center backup power systems.

For those different bus voltage level DC MGs, traditional small-signal stability

criteria become insufficient when dealing with subsystems containing right-half-plane (RHP) poles or zeros, such as Nyquist or eigenvalue-based methods. To address these challenges, an impedance-based stability criterion has been proposed [51], leveraging generalized Bode plot analysis to evaluate the interaction between interconnected DC buses. In this framework, each DC bus is modeled using a generalized voltage source, a generalized current source, and a two-port impedance representation. This modular modeling approach allows the stability of each bus to be analyzed independently, even in the presence of nonlinearities and destabilizing loads such as CPLs. Moreover, intermittent bus converters are employed to connect buses operating at different voltage levels, enabling power exchange across the MGs while preserving bus-level regulation and enhancing robustness. The proposed method is generalizable and can be extended to single-bus DC MGs or clusters of interconnected MGs.

2.2.3 Reconfigurable topology of DC MGs

To further enhance the fault tolerance and operational flexibility of DC MGs, particularly in multi-bus configurations, researchers have introduced the concept of the ring-bus topology [54]. As shown in Fig. 2.3, a typical ring-bus topology DC MG consists of RESs, ESSs, AC loads, and DC loads. Intelligent Electronic Devices (IEDs) control every node and its neighboring nodes as switches.

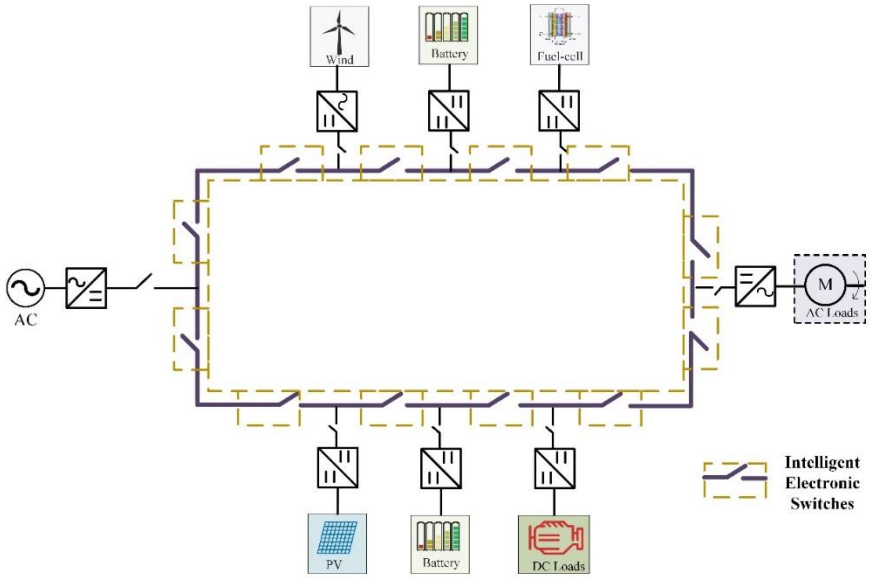

Fig. 2.3 A typical ring-bus topology DC MG [54]

This architecture has many advantages. The most significant advantage is that it provides redundant power paths, significantly improving system reliability. When any bus fails, the IED first detects and isolates the faulty bus from the system, and the rest of the ring network can still supply power to the load through the backup path.

In addition to the ring bus topology, there are two other structures that can improve the stability of the DC MG [36]. The key is that both structures provide redundant designs for possible faults in the DC MG.

As shown in Fig. 2.4, a mesh-type DC MG consists of various AC grids and RESs to supply the power to the DC MG. This structural redundancy ensures that even in the event of a line fault or component failure, alternate paths can continue to supply power to affected zones, thereby enhancing the system's fault tolerance and overall availability. Such mesh-based designs are increasingly adopted in high-voltage DC systems, especially in large-scale infrastructures like offshore wind farms, urban underground DC distribution, and sub-transmission networks [55, 56].

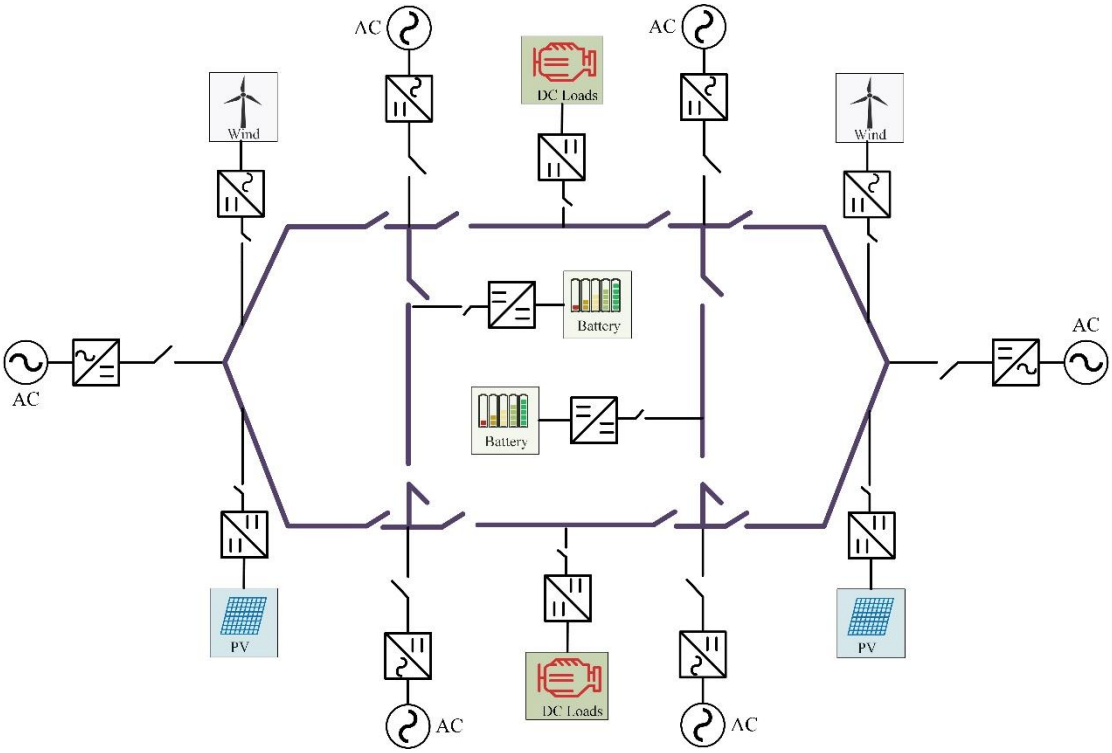

Fig. 2.4 A typical mesh-type topology DC MG [55]

Another DC MG architecture called zonal DC MG can enhance the reliability of the DC MG, which is shown in Fig. 2.5 [57].

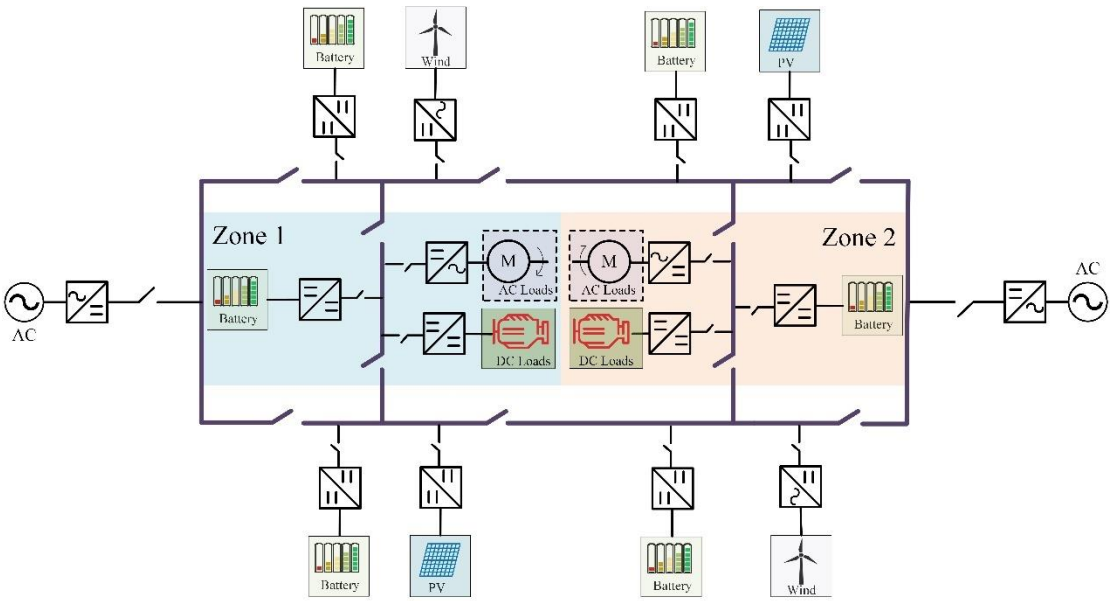

Fig. 2.5 A typical zonal-type topology DC MG [57, 58]

In this architecture, the overall distribution system is divided into multiple electrically independent zones, where each zone is responsible for supplying a local group of loads. Crucially, each zone is connected to two redundant DC buses, typically supplied by upstream AC grids and distributed DC-AC energy sources, forming a symmetrical and cascaded microgrid structure.

This architecture provides significant advantages in terms of reliability, maintainability, and scalability. The dual-bus design allows power to be rerouted within a zone in the event of a fault. For example, if a failure occurs in the upper bus of a given zone, intelligent switching mechanisms (such as opening the upper-side switches and maintaining the lower-side paths) allow the loads to continue receiving power via the alternate feeder. This localized fault-handling capability ensures that failures do not propagate throughout the entire system, thereby preserving the stability and continuity of service for unaffected zones.

In summary, the architectural development of DC MGs has progressed from the basic single-bus configuration to more advanced forms such as multi-bus, ring, mesh, and zonal structures. Each of these topologies reflects the growing demand for improved reliability, scalability, and resilience in modern electrical distribution systems. Single-bus architectures are often favored for their simplicity and ease of implementation, making them suitable for small-scale or low-power systems. In

contrast, multi-bus and ring configurations provide enhanced redundancy and fault isolation capabilities. Mesh networks offer flexible power routing and operational continuity, while zonal architectures support modular expansion and localized fault management through the integration of redundant feeders and distributed resources.

The choice of architecture is closely linked to system-level objectives, including load criticality, physical layout, control complexity, and future scalability. These foundational design strategies directly influence the performance and suitability of DC MGs in various application scenarios. In the following section, we turn our attention to the practical deployment of DC MGs across a range of fields. Specific examples include standalone PV systems supplying CPLs and shipboard power systems operating under dynamic maritime conditions.

2.3 Applications of DC MGs

The increasing penetration of distributed RESs and the growing need for efficient, resilient, and modular power systems have accelerated the adoption of DC MGs across various application domains. Due to their native compatibility with DC-based generation and loads, as well as their reduced conversion losses and simpler control schemes, DC MGs have become a promising alternative to conventional AC systems in many scenarios. Their architectural flexibility, as discussed in the previous section, enables engineers to tailor configurations to the specific requirements of different environments.

In practice, DC MGs have been widely deployed in both stationary and mobile contexts. For example, they are used to power remote or off-grid PV systems where maintaining voltage stability under CPLs is critical. In maritime applications, shipboard DC MGs have emerged as a solution to accommodate dynamic operational conditions, nonlinear loads, and strict reliability requirements. In data centers, DC distribution offers improved energy efficiency, simplified power conversion, and easier integration of renewable energy and energy storage systems. Each of these applications leverages different aspects of DC MG technology to meet performance,

safety, and sustainability goals.

2.3.1 Shipboard DC MGs

DC MGs have found wide applications in modern transportation systems due to their high efficiency, compactness, and compatibility with DC-native loads. In particular, electric vehicle (EV) fast-charging stations [59], railway traction systems[60], aerospace platforms [61], and all-electric aircraft [62] have increasingly adopted DC-based power architectures to reduce conversion stages and enable high power density. The growing demand for electrification, combined with the proliferation of renewable energy and energy storage technologies, has further accelerated this trend.

In recent years, the concept of DC MGs has extended to maritime systems, where ships are evolving from conventional AC-based platforms to more flexible shipboard DC MGs [41]. This transition is driven by several advantages offered by DC architectures: the elimination of synchronization issues, reduced copper losses, higher energy efficiency, and easier integration of renewable sources and ESSs. Moreover, DC systems allow for more efficient propulsion, simplified distribution, and a more modular design approach that suits the spatial constraints and dynamic nature of ship operations [42, 63].

Current shipboard DC MGs are typically deployed in naval vessels, offshore support ships, hybrid ferries, and cruise ships, where high power demands and mission-critical operations require enhanced system stability and fault tolerance. For example, zonal architectures divide the ship into independent power regions with redundant DC buses, improving survivability and fault isolation. Fast transient support using battery-supercapacitor hybrid ESSs, combined with DC-DC converters, enables stable operation under pulsed or CPLs [64].

A representative example of shipboard DC MG implementation is ABB’s Onboard DC Grid system. By replacing conventional AC switchboards and transformers with a common DC bus, this system significantly reduces the weight and

space requirements of shipboard power distribution. It allows variable-speed operation of diesel generators, improving fuel efficiency and reducing emissions by up to 20–27% under typical operating conditions [65]. The modular DC architecture also simplifies the integration of multiple power sources, including batteries and fuel cells, enabling peak shaving, dynamic load support, and enhanced operational flexibility. In addition, ABB's system employs fast DC protection devices and intelligent energy management, ensuring high reliability and safety even under fault conditions. These advantages make DC-based architectures an attractive solution for modern electric and hybrid-electric vessels [66].

Despite these advantages, shipboard DC MGs face unique technical challenges. One major issue is the voltage instability induced by CPLs such as electric propulsion, radar, and weapon systems. These loads introduce negative incremental impedance, making the DC bus susceptible to oscillations and collapse during fast power transitions. Moreover, marine environments are highly dynamic, with frequent mode switching (e.g., docking, cruising, maneuvering), which demands adaptive control strategies. Traditional droop control often lacks sufficient dynamic response, prompting researchers to explore nonlinear control methods to enhance robustness and response speed. This issue is discussed in detail in Section 2.3.3.

Shipboard DC MGs represent one of the most promising applications of DC MG technology, particularly in maritime sectors striving for electrification, operational flexibility, and enhanced energy efficiency. By enabling the integration of renewable sources, advanced ESSs, and high-performance propulsion, DC-based architectures significantly reduce weight, improve conversion efficiency, and simplify power distribution. However, the unique challenges posed by the shipboard environment include tightly coupled CPLs, rapid dynamic mode transitions, and harsh operating conditions. Recent studies have explored nonlinear and adaptive control techniques to stabilize the DC bus voltage under such constraints. Looking ahead, the future of shipboard DC MGs will increasingly rely on intelligent, model-based, and disturbance-resilient control frameworks that can dynamically adjust to uncertain and time-varying load conditions. In this context, a control strategy that combines Model

Predictive Control (MPC) with a Nonlinear Disturbance Observer (NDO) emerges as a compelling solution, capable of accurately predicting system behavior while actively compensating for unknown disturbances. Chapter 4 presents the design and validation of such an approach, demonstrating its potential to significantly enhance the stability and reliability of next-generation shipboard DC MG systems.

2.3.2 Data Centers with DC MG

With the increasing demand for data processing and transmission, data centers have emerged as one of the largest energy consumers globally [67]. According to the International Energy Agency (IEA), data centers currently account for approximately 1.5% of global electricity consumption. With the ongoing proliferation of hyperscale data centers in recent years, electricity consumption in this sector continues to rise sharply, posing significant challenges to grid stability and energy sustainability [68]. In a typical data center, only about half of the total power consumption is used by IT equipment such as servers, storage systems, and networking devices, while the remaining energy is consumed by supporting infrastructure, including cooling systems, power distribution networks, and auxiliary lighting. [67, 69]. Due to the continuing demand for efficient and reliable power delivery in data centers, both industry and academia have increasingly focused on the development of energy-efficient solutions based on DC MG architectures. Unlike traditional AC-based systems, which involve multiple stages of AC-DC and DC-AC conversions, DC MGs provide a more streamlined and loss-minimizing approach to power distribution, particularly in environments where most end-use equipment, such as servers, storage devices, and cooling units, inherently operate on DC power. This paradigm shift is motivated not only by the desire to improve Power Usage Effectiveness (PUE) [70] but also by the growing integration of RES and ESS, which naturally align with DC infrastructure. As a result, DC MGs are becoming a promising technological foundation for building next-generation green data centers that demand high efficiency, scalability, and resilience. Fig. 2.6 shows the typical data center with a DC MG structure.

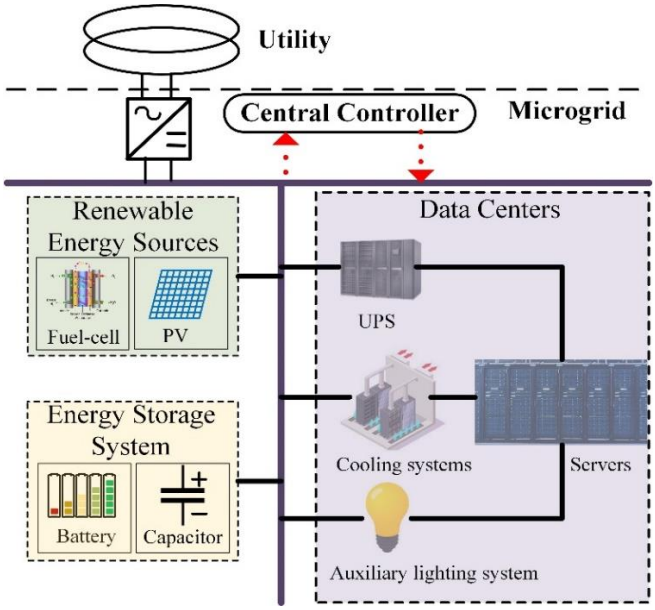

Fig. 2.6 A simplified DC MG structure of a data center [71]

An Uninterruptible Power Supply (UPS), usually comprising batteries or fuel cells, is connected to the intermediate DC bus to ensure resilience during power outages. In a conventional AC-based data center setup, incoming AC power from the grid is first rectified into DC to charge the UPS, then inverted back into AC to supply the Power Distribution Units (PDUs). These PDUs, in turn, feed server racks equipped with Power Supply Units (PSUs) that once again convert AC into DC voltages suitable for computing loads [72]. This multi-stage AC-DC-AC-DC conversion chain introduces about 23% to 25% energy losses and generates excess heat [36]. According to Lawrence Berkeley National Laboratory (LBNL), compared to a standard 415 V AC setup, the 380 V DC configuration resulted in 7% higher overall energy efficiency, 15% lower capital expenditure, 33% reduction in physical space requirements, and up to 36% lower total cost of ownership [40]. These gains are achieved not only through electrical efficiency improvements but also due to simplified system design, lower cooling loads, and reduced infrastructure complexity.

There is a sample in Hangzhou, China. The Alibaba Qiandao Lake Data Center [73] stands out as a model of sustainable and integrated energy design. It is powered by a combination of rooftop PV panels and hydropower, ensuring a significant share of its electricity comes from renewable sources. To maximize energy efficiency, the facility employs high-efficiency transformers and UPS systems, which are seamlessly

integrated with a 240V DC MG that directly powers the servers, minimizing energy losses from conversions. Additionally, the data center utilizes deep lake water from Qiandao Lake as a natural cooling solution, significantly reducing the need for mechanical cooling. In periods of low solar irradiance or insufficient hydropower generation, the system can automatically switch to the main utility grid, ensuring uninterrupted operation. This hybrid infrastructure exemplifies a highly efficient, low-carbon data center design tailored to local renewable resources.

Collectively, these findings underline the promising future of DC MG architectures in data center applications, especially in an era of growing demand for energy efficiency, sustainability, and seamless integration with renewable energy sources. As more IT equipment becomes inherently DC-powered and as data centers increasingly adopt on-site PV and ESS, the shift to DC distribution is poised to become a foundational trend in building the next generation of green and high-performance data centers.

2.3.3 Stability Challenges in DC MG Applications

DC MGs deployed in mission-critical environments, such as data centers and shipboard power systems, must ensure high levels of operational stability under dynamic and uncertain conditions. In both cases, the power system must respond to rapid load variations, maintain voltage regulation within tight tolerances, and provide uninterrupted service during faults or reconfiguration events. However, ensuring the stable operation of a DC MG remains a significant challenge, especially under high penetration of CPLs and intermittent RESs [74].

In practical DC MG applications, many power electronic loads can be modeled as CPLs. For instance:

1) Data Centers: Servers and communication equipment are typically powered by tightly regulated DC-DC converters or PSUs. These converters adjust their input current to maintain a constant output power to IT equipment, making their input characteristics behave as CPLs [74].

2) Shipboard: Propulsion motors, radar systems, and other electronically controlled actuators use power converters that tightly regulate power delivery, especially under varying mechanical or operational conditions, effectively behaving as CPLs [75].

CPLs exhibit a negative incremental impedance characteristic when viewed from the DC bus. As shown in Fig. 2.7, the current of the CPL is drawn by its input voltage.

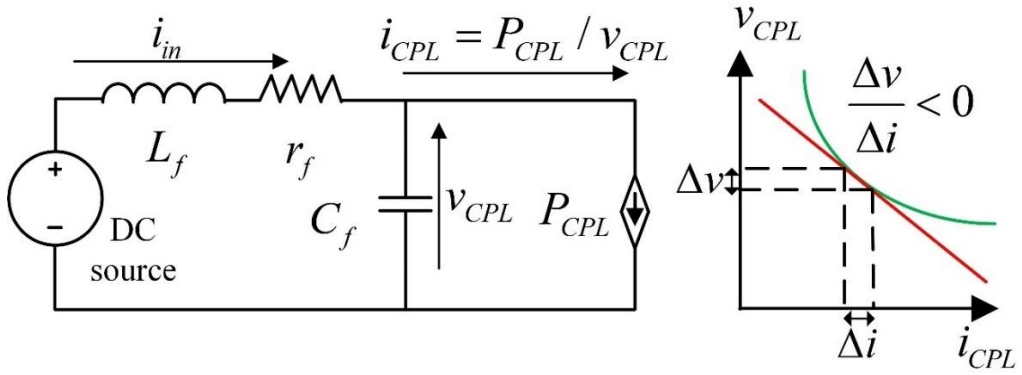

Fig. 2.7 The characteristics of the CPL

For a given operating point, the rate of change of current is

$$\frac{\partial i_{CPL}}{\partial v_{CPL}} = -\frac{P_{CPL}}{v_{CPL}^2} \tag{2.1}$$

At the above operating point, the V-I curve of CPL can be approximated by a straight line tangent to the curve.

$$i_{CPL} = -\frac{P_{CPL}}{v_{CPL,operating}^2} v_{CPL} + 2\frac{P_{CPL}}{v_{CPL,operating}} \tag{2.2}$$

where $v_{CPL,operating}$ represents the voltage value of the operating point. The negative sign indicates that when the bus voltage slightly drops, the CPL draws more current to keep *P* constant, which further decreases the bus voltage. This positive feedback loop can destabilize the system, leading to high-frequency oscillations or even voltage collapse, especially in low-inertia and weakly damped DC MGs [76].

To address these issues, researchers have explored both topology-level and control-level solutions. On the topology design side, Hou et al. [77] proposed a Partial Power Processing (PPP) converter system for islanded DC MGs. This structure enables RESs and ESSs to be connected to the bus through a dual active bridge (DAB)

to achieve local energy processing. Compared with Full Power Processing, only a part of the energy in this structure is processed by DAB, which greatly reduces the design pressure of the power processor, improves the overall efficiency of the system, and reduces the size and loss of components. The research also designs an improved PI control strategy for the DAB-based PPP converter that can achieve rapid voltage support through a local power regulation mechanism, even when RES output changes, energy storage voltage fluctuates, or load changes.

On the control side, several methods have been introduced to improve dynamic performance. The fast dynamics of power electronic converters, along with the highly nonlinear nature of CPLs and renewable sources, make traditional PI control approaches less effective. Advanced approaches such as sliding mode control (SMC) [78-80], passive-based control (PBC) [81, 82], and MPC [83-85] have been actively researched. These strategies aim to counteract the nonlinear destabilizing effects of CPLs. Among these control methods, the use of a disturbance observer has shown strong robustness against parameter uncertainty and input voltage fluctuations [78, 80]. The addition of the disturbance observer allows the controller to obtain the changes of load and bus voltage in DC MGs in a timely and accurate manner.

Among the various nonlinear control approaches developed to stabilize shipboard DC MGs under the influence of CPLs, SMC has emerged as a robust method due to its strong disturbance rejection and fast transient response. By enforcing a high-frequency switching action around a predefined sliding surface, SMC ensures that the system state converges to desired voltage levels despite large load variations [86]. In [87], the proposed controller integrates a Finite-Time Disturbance Observer (FTDO) with a Fixed-Time Terminal Sliding Mode Controller (FTTSMC) to reliably stabilize a DC-DC converter feeding an uncertain CPL in shipboard conditions. First, the FTDO estimates the rapid variations in CPL power within a guaranteed finite time, capturing real-time load disturbances effectively. Using this disturbance estimate, the FTTSMC then drives the DC bus voltage towards its reference value with fixed-time convergence, meaning stability is achieved in a time bound that does not depend on initial conditions—an especially important

property under sudden load changes.

Another robust control method applied in shipboard DC MGs that has caught researchers' attention is the PBC strategy. PBC is a high-gain nonlinear control method rooted in the principle of energy conservation, where the energy supplied to the system equals the sum of energy stored and energy dissipated [88]. The passivity property offers an alternative framework to analyze and stabilize nonlinear systems, especially under destabilizing influences such as CPLs, by ensuring that the system behaves like a passive energy processor. In [82], the authors proposed a robust PBC strategy for stabilizing a shipboard DC MG equipped with interleaved bidirectional DC-DC converters feeding uncertain CPLs. The control design leverages the concept of strict passivity to ensure that the closed-loop system exhibits dissipative behavior by using virtual damping resistances to restructure the system's energy, counteracting the negative incremental impedance introduced by CPLs. To improve robustness, the controller incorporates feedback terms to handle parameter uncertainties and external disturbances. This approach is particularly suitable for shipboard environments, where load dynamics are fast and system reliability is critical.

Existing control strategies for stabilizing DC MGs with high penetration of CPLs have demonstrated varying degrees of effectiveness. SMC offers strong robustness against parameter uncertainties and external disturbances but may suffer from chattering issues and is sensitive to measurement noise. PBC provides a systematic framework for ensuring global stability by shaping the system's energy function. However, its performance strongly depends on accurate system modeling and may be difficult to implement under rapidly changing operating conditions. These limitations indicate that existing approaches are either overly model-dependent, lack fast large-signal response capability, or cannot guarantee robust performance under strong nonlinearities introduced by CPLs.

2.4 Conclusion

In summary, this chapter has reviewed the structural evolution and practical

applications of DC MGs across a range of emerging scenarios, including energy-critical facilities such as data centers and shipboard power systems. Various architectures—from simple single-bus to advanced reconfigurable topologies—have been explored for their potential to improve efficiency, enhance reliability, and facilitate seamless integration with renewable energy sources and DC-native loads. These developments illustrate the growing maturity of DC MGs as a viable and scalable solution for modern power distribution.

However, as DC MGs become more complex and widely deployed, new challenges have emerged, particularly in maintaining voltage stability under dynamic load conditions and mitigating the destabilizing effects of CPLs. Addressing these challenges requires not only robust system architectures but also the development of advanced control strategies that can dynamically regulate system behavior under uncertainty.

To address these issues, the next two chapters present advanced control strategies tailored to these needs. Chapter 3 focuses on a disturbance observer-based backstepping control approach for a multilevel boost converter to maximize PV energy harvesting under varying environmental and load conditions. Chapter 4 introduces a robust voltage regulation framework based on MPC, enhanced by a high-order NDO, to ensure stable DC bus performance in the face of CPL-induced instability and other uncertainties.

Together, these two chapters provide system-level solutions to the control challenges identified in this review and further advance the practical implementation of DC MGs in next-generation power systems.

Chapter 3 Nonlinear Control of Multilevel Boost Converter for Maximum PV Energy Harvesting in DC MG

3.1 Introduction

In recent years, the increasing penetration of renewable energy sources and the widespread application of power electronic loads have posed significant challenges to the stability, flexibility, and efficiency of traditional power distribution systems. The inherently intermittent and unpredictable nature of renewable generation, such as photovoltaic (PV) and wind power, introduces large fluctuations in both voltage and power balance. To address these issues, direct current (DC) microgrids have been proposed as a promising alternative to traditional power architectures. Fig. 3.1 shows a typical structure of a DC Microgrid. A DC microgrid (DC MG) typically consists of distributed energy sources such as PV and wind generation, energy storage systems (ESS), and various types of DC loads. This architecture offers improved energy efficiency, enhanced compatibility with DC-native components, and greater flexibility for control and operation.

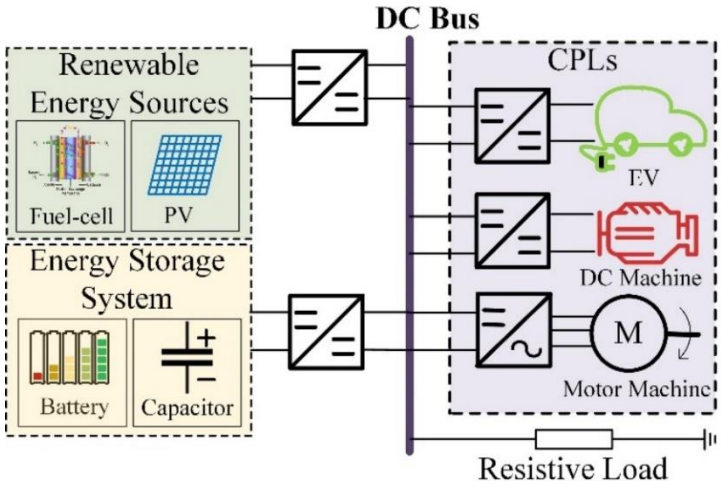

Fig. 3.1 A typical structure of a DC Microgrid

Compared to AC systems, DC MGs offer several advantages, including reduced

conversion losses, improved system efficiency, simplified integration with renewable sources, and better compatibility with modern electronic loads [13]. Additionally, DC MGs provide enhanced controllability and modularity, which makes them especially suitable for applications requiring a flexible and reliable power supply. It is particularly suitable for remote or off-grid applications, where stable and efficient power delivery is essential.

Among renewable sources, PV systems are widely utilized due to their ease of deployment and scalability. Ideally, it is preferable to operate each PV panel at its respective maximum power point (MPP) for achieving the maximum PV energy harvesting. Environmental factors such as irradiance and temperature variations will affect the MPP, necessitating the use of feasible maximum power point tracking (MPPT) algorithms.

To meet the high voltage terminal loads, boost converters are applied to connect the power source and loads. However, a conventional boost converter has a limited voltage boosting ratio due to the parasitic resistance of the filtering components. Besides, a large output electrolytic capacitor is compulsorily required to enable a smooth DC bus voltage, increasing the volume and degrading the reliability [89]. A multilevel boost converter (MBC) connected to stacked capacitors is a suitable alternative to increase the voltage boost ratio [90]. It provides an efficient means to boost voltage and maintain a stable power supply.

However, a critical challenge arises from the nature of typical data center loads. These are often composed of tightly regulated power converters that behave as constant power loads (CPLs), exhibiting negative impedance characteristics. Their negative equivalent impedance significantly affects the stability of power systems in response to voltage fluctuations, particularly for PV-powered DC MGs [91]. A decrease in bus voltage due to insufficient PV generation leads to an increase in CPL current, which further aggravates the voltage drop, forming a detrimental feedback loop. Conversely, a voltage rise results in decreased current draw, causing instability in the opposite direction. It creates a detrimental voltage feedback loop [92], greatly decreasing the voltage stability margin of the system [93].

To mitigate this issue and ensure reliable power delivery, energy storage systems (ESS) are commonly integrated into DC MGs. During periods of excess PV generation, surplus energy is stored in the ESS. Conversely, when PV output is insufficient, the ESS discharges to compensate for the shortfall. This coordinated operation helps balance supply and demand, allowing the PV to remain at its MPPT while maintaining load stability.

Nonetheless, integrating CPLs, ESS, and MBC into a unified system introduces complex nonlinear dynamics that challenge conventional control strategies. To address this challenge, various voltage control methods have been proposed. In the passive damping method, the system's damping is increased by connecting a resistor or inductor in parallel to the bus or load terminal of the DC MG, thereby alleviating the voltage oscillation caused by the CPL load [94]. However, passive damping increases component size and cost, which increases system loss and reduces overall efficiency. In addition, passive damping has limited performance when facing large-scale CPL or dynamic loads. In contrast to passive damping methods, the active damping method emulates the damping effect through power electronic devices and control algorithms, thereby improving the stability of the system without adding additional physical components. The active damping system measures the current or voltage signal of the CPL and generates a compensation signal through a digital control algorithm to adjust the operating point of the load, thereby attenuating voltage oscillation [95].

There are also other nonlinear control strategies to eliminate the negative impedance characteristics of CPL and achieve the purpose of stabilizing the bus voltage. Model predictive control (MPC) is a forward-looking control method based on dynamic system models. It has been widely used to control complex power systems in recent years. In CPL-integrated DC MGs, the MPC can predict the trajectory of voltage fluctuations in advance and actively adjust the control signals of power electronic equipment to suppress instability [96]. However, the MPC method has high requirements on the hardware computational capacity, which limits its application. Sliding Mode Control (SMC) is a highly robust nonlinear control method.

This method first defines a sliding surface, which represents the desired dynamic behavior of the system. By designing the control law, the state variables of the system (such as voltage and current) converge to and slide along the sliding surface until the system reaches the steady-state value [97]. Feedback linearization is a technique that converts a nonlinear system into a linear system through state feedback. In this method, the system dynamics are linearized by selecting appropriate control inputs, facilitating the control law design [98]. Additionally, Lyapunov-based approaches provide rigorous theoretical foundations for analyzing system stability [99]. Ref. [98] introduces the Lyapunov stability theory to ensure that the system can reach the desired voltage level. This control strategy can also add disturbance observers to eliminate potential errors when performing real-time state monitoring, such as voltage and current [100]. In [101], a distributed CPL load stability control strategy is proposed. By introducing a master-slave control architecture, the global stability of the DC MG under CPL load is successfully achieved.

To simultaneously achieve voltage stability and maximum energy harvesting in PV-powered DC MGs, this chapter proposes a robust control strategy integrating a backstepping controller with a nonlinear disturbance observer (NDO). The key contributions of this chapter can be summarized as follows:

1) **System architecture design:** A comprehensive DC MG architecture is established, consisting of PV arrays, MBC, CPLs, ESS, and other loads, enabling flexible and stable power delivery for data center applications.
2) **Nonlinear control strategy:** A novel backstepping controller integrated with an NDO is developed to suppress CPL-induced negative impedance effects and ensure DC bus voltage stability under large-signal disturbances.
3) **Lyapunov-based stability proof:** The global asymptotic stability of the proposed control system is rigorously demonstrated via Lyapunov theory, ensuring robust voltage regulation under time-varying load conditions.
4) **Simulation verification:** Comparative simulation studies show that the proposed method significantly outperforms traditional dual-PI control in terms of voltage stability, particularly under fluctuating CPL demand.

3.2 Model of A PV-supplied DC MG

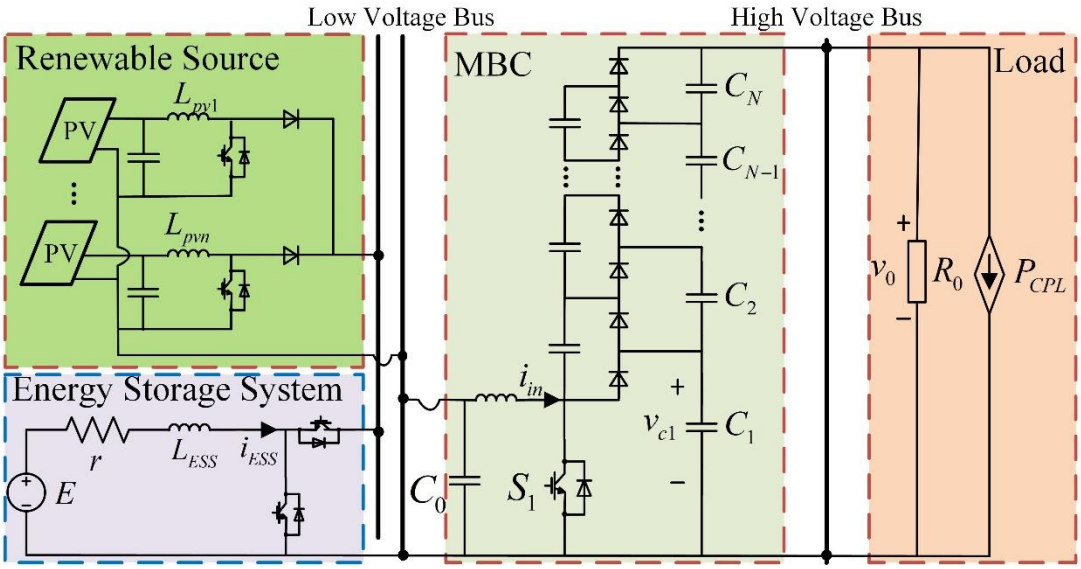

Fig. 3.2 The simplified topology of MBC with CPL for PV-supplied DC MG system

The simplified topology of MBC with CPL for PV-supplied DC MG system is shown in Fig. 3.2. Multiple PV panels are connected in parallel to the MBC, enabling each panel to independently operate at its MPP. Even if some PV panels experience variations in environmental irradiance and temperature or faults, the PV power plant can still achieve the MPPT. An N-level switched-capacitor circuit is connected to the output side of the converter, providing a high voltage conversion ratio and improved efficiency. Furthermore, the ESS can absorb excess energy to ensure maximum energy harvesting of the DC MG. And it is able to supplement the energy required on the load side when the energy provided by PV panels is insufficient. It is a vital role for the ESS to achieve a power balance and the reuse of renewable energy.

3.2.1 Modeling of PV panels

PV panels are composed of different PV cells connected in series or parallel. Fig. 3.3 illustrates a single PV cell circuit structure. One critical component in the circuit structure of PV panels is the bypass diode. This diode is placed in parallel with groups of cells to prevent power loss due to variations in environmental irradiance and temperature or malfunctioning cells. A five-parameter model can describe the

electrical characteristics of a PV array module. This model includes a current source I_L generated by illumination, a diode, a series resistance R_s, and a shunt resistance R_{sh}, which characterize the module's current-voltage *I-V* behavior under varying irradiance and temperature conditions.

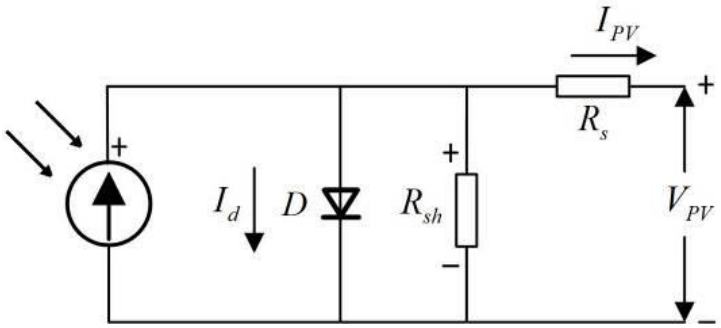

Fig. 3.3 A PV cell circuit

The following equations define the diode I-V characteristics for a single module:

$$\begin{cases} I_d = I_0[\exp(\frac{V_d}{V_T}) - 1] \\ V_T = \frac{kT}{q} \times nl \end{cases} \tag{3.1}$$

where I_d is the diode's current, I_0 is the saturation current of the diode, V_d is the diode's voltage, and *nl* is the diode ideality factor, a number close to 1. k=1.3806×10^{-23} J·K^{-1} is the Boltzmann constant and q=1.6×10^{-19}. The following figure shows the P-V characteristics of PV panels under different irradiance and temperature.

3.2.2 Perturb and Observe (P&O) for MPPT

The P&O algorithm adjusts the output voltage to operate the PVs at MPP. In this way, the module voltage is periodically disturbed. By connecting the converter and changing the duty cycle, the PV panel's output power can be continuously adjusted. The duty ratio of the DC-DC boost converter is given by

$$D_i = 1 - \frac{V_i}{E}\left(i = 1, 2...n\right) \tag{3.2}$$

where *i* is the *i*-th PV panel, *E* is the output voltage of the boost converter, and V_i is the output voltage of the PV panel.

Fig. 3.4 is a flowchart of the P&O method to track the maximum power point. After every fixed perturb step, a judgment is required to determine the next action. If the output power increases: $\Delta P > 0$, it indicates that the direction of reference voltage adjustment is correct. Therefore, the voltage reference can continue to be adjusted in the original direction. Conversely, if the output power is lower than the previous interference: $\Delta P < 0$, the direction of voltage reference adjustment needs to be changed.

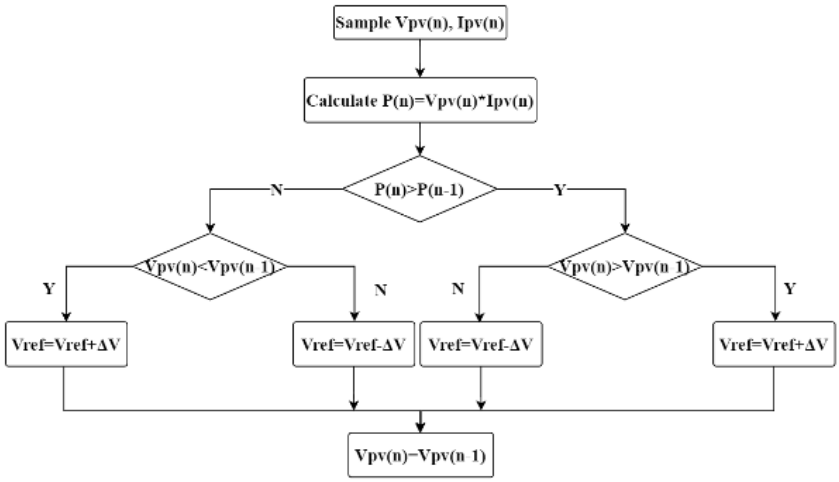

Fig. 3.4 The flowchart of the P&O algorithm

3.2.3 Modeling of the MBC

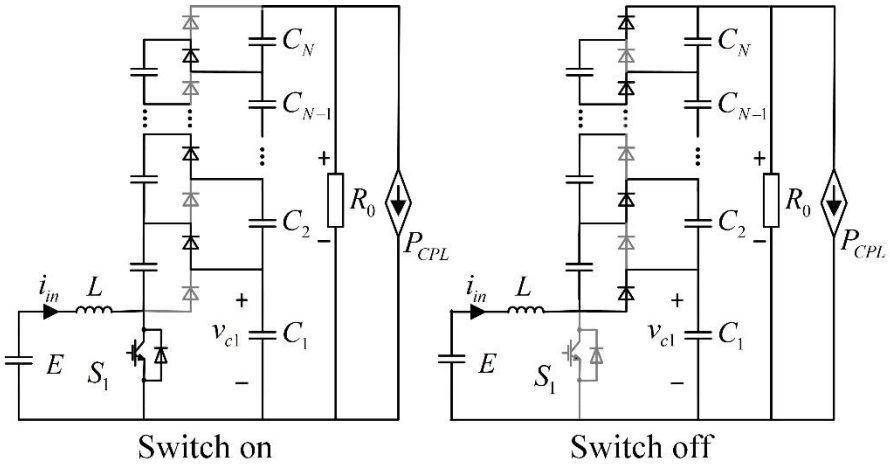

Fig. 3.5 N-level multiphase boost converter

The topological structure of the Nth-order MBC model is shown in Fig. 3.5. It

combines a traditional boost converter and a multiplier diode capacitor circuit. It is possible to simultaneously achieve voltage balance between capacitors and high boost gain. There are two working states that depend on whether the switch is on or off. Hence, the reduced-order model of the MBC can be concluded.

$$\begin{cases} L\dfrac{di_{in}}{dt} = E-(1-d)\dfrac{v_0}{N} \\ C\dfrac{dv_0}{dt} = \dfrac{N}{1+d}[(1-d)i_{in}-\dfrac{v_0}{R_0}-\dfrac{P_{CPL}}{v_0}] \end{cases} \tag{3.3}$$

where L is the value of the inductor, C is the value of the capacitor, E is the input voltage, v_0 is the output voltage which is equal to the DC bus voltage, and d is the duty cycle.

It is worth mentioning that it is easy for the capacitors and inductors to deviate from their nominal values in practical dynamic operating conditions. Due to the inherent uncertainty that is difficult to quantify, it is almost impossible to obtain accurate values online. Without loss of generality, the uncertainty of inductors and capacitors can be considered interference in modeling. Therefore, the reduced order model of MBC can be summarized as

$$\begin{cases} (L+\Delta L)\dfrac{di_{in}}{dt} = E-(1-d)\dfrac{v_0}{N} \\ (C+\Delta C)\dfrac{dv_0}{dt} = \dfrac{N}{1+d}[(1-d)i_{in}-\dfrac{v_0}{R_0}-\dfrac{P_{CPL}}{v_0}] \end{cases} \tag{3.4}$$

where ΔL and ΔC are the uncertainties in inductance and capacitance, respectively. The output power of MBC can be given by

$$P_0 = \frac{v_0^2}{R_0} + P_{CPL} \tag{3.5}$$

3.2.4 Modeling of the ESS

The ESS plays a critical role in maintaining energy balance within the DC MG by dynamically absorbing or supplying power in response to the mismatch between PV generation and load demand. The structure of the ESS is shown in Fig. 3.6. The

bidirectional DC-DC converter is connected to the voltage and the DC low-voltage bus.

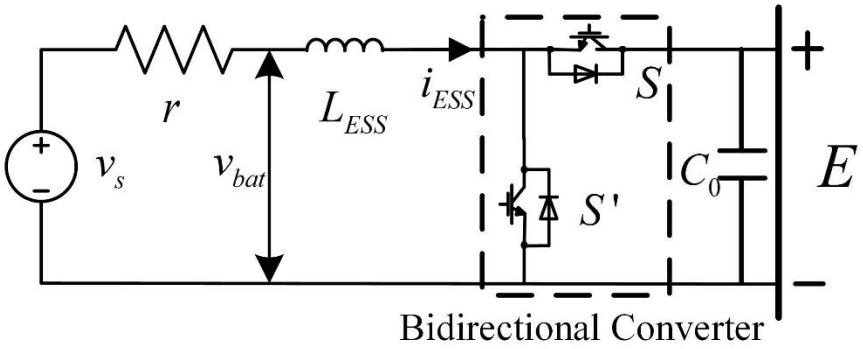

Fig. 3.6 Typology of the energy storage system (ESS)

The dynamic function of the inductor is

$$L_{ESS}\frac{di_{ESS}}{dt} = v_s - i_{ESS}r - Ed_{ESS} \tag{3.6}$$

where r is the internal resistance of the DC source, and its value is extremely small. Therefore, the value of the v_{bat} can be replaced by $E.d_{ESS}$ represents the duty ratio of the bidirectional converter. A dual-PI controller is designed for ESS to absorb the surplus power from the PV generation and discharge to compensate for the insufficient power on the load side. Tracking the current loop is the internal loop. The dynamic function is as follows

$$\begin{cases} v_L d_{ESS} = -K_{pi}(i_{ESSr} - i_{ESS}) - K_{ii}e_i \\ \dfrac{de_i}{dt} = i_{ESSr} - i_{ESS} \end{cases} \tag{3.7}$$

where i_{ESSr} represents the reference value of the i_{ESS}. K_{pi} and K_{ii} represent the gains of the current controller. The dynamic function of the capacitor is

$$C_0\frac{dE}{dt} = i_{pv}d_{pv} + i_{ESS}d_{ESS} - i_{in}d \tag{3.8}$$

The difference between the injected current from the solar PV panel and the input current of the boost converter is considered as an external constant disturbance applied to the DC link. Therefore, the energy dynamic function of the capacitor C_0 is

$$\frac{dW_{C_o}}{dt} = i_{ESS}E + \Delta P, \Delta P = P_{PV} - P_0 \tag{3.9}$$

The reference value of the i_{ESS} can be designed as

$$\begin{cases} i_{ESSr} = \dfrac{1}{v_{bat}}(K_{pv}(W_{C_o r} - W_{C_0}) + K_{iv}e_v) \\ \dfrac{de_v}{dt} = W_{C_o r} - W_{C_0} \end{cases} \tag{3.10}$$

where v_{bat} represents the output voltage of the DC voltage source. $W_{C_0 r}$ represents the reference value of the energy of the capacitor. K_{pv} and K_{iv} represent the gains of the voltage controller.

3.3 Backstepping Control Based on Disturbance Observer

A nonlinear control method combined with an NDO is proposed in this Section. This controller can effectively regulate the output voltage with the CPL. Fig. 3.7 shows the overall control of the observer-based backstepping control.

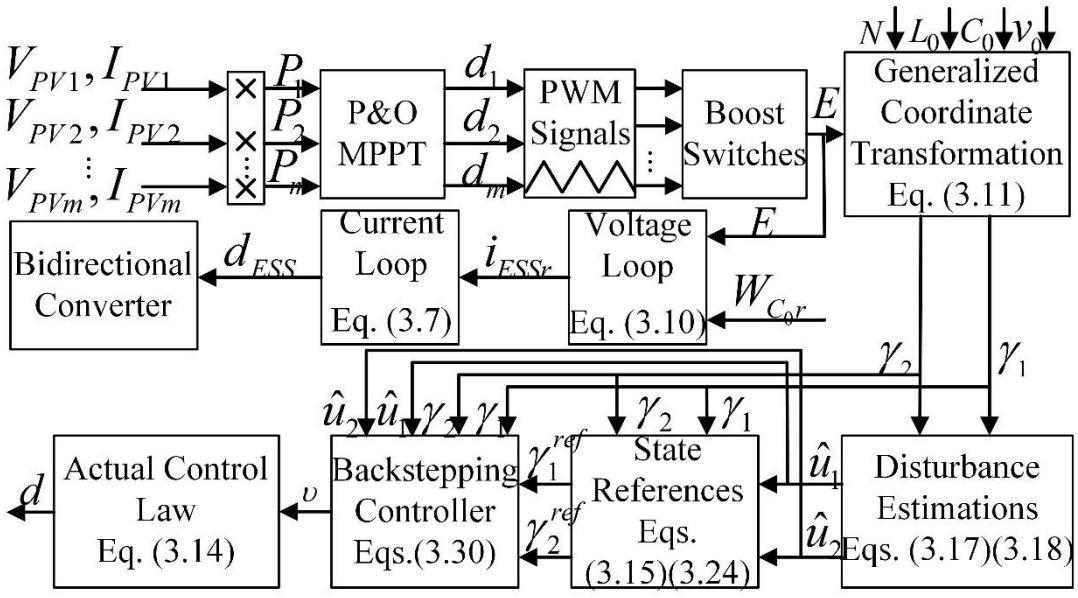

Fig. 3.7 Overall observer-based backstepping control diagram

3.3.1 Coordinate Form Transformation

Assume γ_1 as the total energy stored in the system, and γ_2 is the input power of

the MBC. The system dynamic states can be illustrated by

$$\begin{cases} \gamma_1 = \frac{1}{2} L i_{in}^2 + \frac{2N-1}{2} C (\frac{v_0}{N})^2 \\ \gamma_2 = E i_{in} \end{cases} \tag{3.11}$$

The derivatives of the dynamic states are

$$\begin{cases} \gamma_1' = L i_{in} i_{in}' + \frac{2N-1}{N^2} C v_0 v_0' \\ \gamma_2' = E i_{in}' \end{cases} \tag{3.12}$$

A simplified expression can be defined

$$\begin{cases} \gamma_1' = \gamma_2 + u_1 \\ \gamma_2' = \upsilon + u_2 \end{cases} \tag{3.13}$$

where u_1 is the unmeasured disturbance, u_2 represents the unknown disturbance, and υ is an intermediate control variable. By combining Eqs. (3.3), (3.11), and (3.12), the duty cycle *d* in Eq. (3.3) is derived as

$$d = 1 - \frac{NE}{v_0} + \frac{NL\upsilon}{E v_0} \tag{3.14}$$

Back to the original control objective is to track the output voltage of MBC v_0 to the DC bus voltage v_0^{ref}. This regulation requirement can be transformed to enforce γ_1 and γ_2 to their reference value.

$$\gamma_1^{ref} = \frac{1}{2} L (\frac{P_0^{ref}}{E})^2 + \frac{1}{2} (2N-1) C (\frac{v_0^{ref}}{N})^2 \tag{3.15}$$

where γ_1^{ref} is the reference value of γ_1, and the reference value of γ_2 is given in the next subsection.

3.3.2 High-Order NDO Design

This part constructs a high-order NDO to estimate the disturbances and uncertainties for improving the control dynamics. There are two assumptions that can be made since the disturbances and uncertainties (i.e., u_1 and u_2) are brought mainly by power disturbances and uncertainty of circuits.

Assumption 1: The load power is unknown, but the nominal circuit parameters, including measured input voltage *E*, nominal inductance *L*, and nominal capacitance *C* are known.

Assumption 2: The disturbances $u_r(t), r=1,2$ and their extended order derivatives $u_r'(t)$ are bounded.

$$\sup_{t>0}\left|u_r(t)\right| \le \delta, \sup_{t>0}\left|u_r'(t)\right| \le \delta \tag{3.16}$$

where δ is a known positive constant.

According to [102], the NDO can be designed as

$$\begin{cases} \hat{u}_1 = m_{11} + h_{11}\gamma_1, m_{11}' = -h_{11}(\gamma_2 + \hat{u}_1) + \hat{u}_1' \\ \hat{u}_1' = m_{12} + h_{12}\gamma_1, m_{12}' = -h_{12}(\gamma_2 + \hat{u}_1) \end{cases} \tag{3.17}$$

$$\begin{cases} \hat{u}_2 = m_{21} + h_{21}\gamma_2, m_{21}' = -h_{21}(\upsilon + \hat{u}_2) + \hat{u}_2' \\ \hat{u}_2' = m_{22} + h_{22}\gamma_2, m_{22}' = -h_{22}(\upsilon + \hat{u}_2) \end{cases} \tag{3.18}$$

where $h_{ij}(i=1,2; j=1,2)$ are positive adjustable high-order NDO gains to be designed. m_{ij} are the additional variables. Δu_i and $\Delta u_i'$ can be defined as the observation errors of u_i and u_i'. These errors and their dynamics can be expressed as

$$\begin{cases} \Delta u_i = u_i - \hat{u}_i, (\Delta u_i)' = -h_{i1}\Delta u_i + \Delta u_i' \\ \Delta u_i' = u_i' - \hat{u}_i', (\Delta u_i')' = -h_{i2}\Delta u_i + u_i'' \end{cases} \tag{3.19}$$

According to the above assumption, since u_i'' is bounded by δ, it is possible to find suitable $h_{i1} > 0$ and $h_{i2} > 0$ to ensure the stability of Δu_i. Generally, because $\Delta L \ll L$ and $\Delta C \ll C$, it is reasonable to consider $P_0 = -u_1, P_0^{ref} = -\hat{u}_1$.

3.3.3 NDO-based Backstepping Controller Design

In this part, a backstepping controller is proposed to regulate the MBC. The design procedure of the NDO-based controller includes two steps.

Step 1: The expression of the dynamic state error e_1 is

$$e_1 = \gamma_1 - \gamma_1^{ref} \tag{3.20}$$

A Lyapunov function can be established:

$$V_1 = \frac{1}{2}e_1^2 + \frac{1}{2}\Delta u_1^2 \tag{3.21}$$

The derivative of V_1 is

$$\begin{aligned} V_1' &= e_1 e_1' + \Delta u_1 (\Delta u_1)' \\ &= e_1(\gamma_2 + u_1 - \gamma_1^{ref\prime}) + \Delta u_1 (\Delta u_1)' \end{aligned} \tag{3.22}$$

The reference of γ_2 needs to stabilize the function. Hence, the second tracking error variable can be designed

$$e_2 = k_1 e_1 + e_1' - \Delta u_1 \tag{3.23}$$

where k_1 is a positive constant. To expand Eq. (3.23) and combine Eq. (3.13) and Eq. (3.19). The reference of γ_2 can get

$$\begin{aligned} \gamma_2 - \gamma_2^{ref} &= k_1 e_1 + \gamma_1 - \gamma_1^{ref} - \Delta u_1 \\ \gamma_1' - u_1 - \gamma_2^{ref} &= k_1 e_1 + \gamma_1 - \gamma_1^{ref} - \Delta u_1 \\ \gamma_2^{ref} &= -k_1 e_1 - \hat{u}_1 + \gamma_1^{ref\prime} \end{aligned} \tag{3.24}$$

Eq. (3.17) and Eq. (3.19) can be further derived as

$$\begin{aligned} \Delta u_1 (\Delta u_1)' &= \Delta u_1 (u_1' - (\hat{u})') \\ &= \Delta u_1 (u_1' - h_{11}\Delta u_1 - \hat{u}_1') \\ &= -h_{11}\Delta u_1^2 + \Delta u_1 \Delta u_1' \end{aligned} \tag{3.25}$$

Therefore, the derivative of V_1 can be rewritten as

$$V_1' = -k_1 e_1^2 + e_1 e_2 + e_1 \Delta u_1 - h_{11}\Delta u_1^2 + \Delta u_1 \Delta u_1' \tag{3.26}$$

Step 2: The second augmented Lyapunov function V_2 can be selected as:

$$V_2 = \frac{1}{2}e_1^2 + \frac{1}{2}e_2^2 + \frac{1}{2}\Delta u_1^2 + \frac{1}{2}\Delta u_2^2 \tag{3.27}$$

The derivative of V_2 is

$$\begin{aligned} V_2' &= V_1' + e_2 e_2' + \Delta u_2 (\Delta u_2)' \\ &= V_1' + e_2(\upsilon + u_2 - \gamma_2^{ref\prime}) + \Delta u_2 (\Delta u_2)' \\ &= V_1' + e_2(\upsilon + u_2 + k_1 e_1' + \hat{u}_1' - \gamma_1^{ref\prime\prime}) + \Delta u_2 (\Delta u_2)' \end{aligned} \tag{3.28}$$

Combining Eq. (3.23) and Eq. (3.24), the expression can be derived as

$$\begin{aligned} V_2' = {} & e_2(\upsilon + u_2 + k_1(e_2 - k_1 e_1 + \Delta u_1) + (\hat{u}_1)' - \gamma_1^{ref\prime\prime}) \\ & + \Delta u_2 (\Delta u_2)' + V_1' \end{aligned} \tag{3.29}$$

Similarly, the intermediate control signal υ can be designed

$$\upsilon = -k_2 e_2 - \hat{u}_2 + \gamma_1^{ref\prime\prime} \tag{3.30}$$

where k_2 is a positive constant. Substituting Eq. (3.30) into Eq. (3.29)

$$\begin{aligned} V_2' = & -k_1 e_1^2 + (k_1 - k_2) e_2^2 + (1 - k_1^2) e_1 e_2 \\ & + (e_1 + (k_1 + h_{11}) e_2) \Delta u_1 + e_2 (\Delta u_2 + \hat{u}_1') \\ & - h_{11} \Delta u_1^2 - h_{21} \Delta u_2^2 + \Delta u_1 \Delta u_1' + \Delta u_2 \Delta u_2' \end{aligned} \tag{3.31}$$

3.3.4 Large-Signal Stability Analysis

Applying the basic inequality $ab \le 1/2(a^2 + b^2)$ to Eq. (3.31), the inequality form of the derivative of V_2 is

$$\begin{aligned} V_2' \le & -\frac{1}{2}(k_1 - 1) e_1^2 \\ & - \frac{1}{2}[2k_2 - (1 - k_1^2)^2 - 3k_1 - h_{11} - 2] e_2^2 \\ & - \frac{1}{2}(h_{11} - k_1 - 2) \Delta u_1^2 - (h_{21} - 1) \Delta u_2^2 \\ & + \frac{1}{2}(\Delta u_1'^2 + \Delta u_2'^2 + \hat{u}_1'^2) \end{aligned} \tag{3.32}$$

It is possible to select the proper parameters to make V_2 stable for a finite period of time. According to Eq. (3.16), there is an upper bound M of the expression $1/2(\Delta u_1'^2 + \Delta u_2'^2 + \hat{u}_1'^2)$. Therefore, Eq. (3.32) can be rewritten as

$$V_2' \le -\omega V_2 + M \tag{3.33}$$

where ω can be set the minimum coefficient among the four variables $e_1^2, e_2^2, \Delta u_1^2, \Delta u_2^2$ in Eq. (3.32). It can define a four-dimensional set of real numbers as $\Psi = \{Z \in R^4 \mid V(Z) \le M/\omega\}$. Thus, for any $Z \notin \Psi$, they will satisfy $V(Z) > M/\omega$. Then the following inequality must hold

$$V' \le -\omega V + M < 0 \tag{3.34}$$

According to the Lyapunov stability principle, the closed-loop system is globally asymptotically stable with the variables at steady states. The large-signal stability of the proposed control is ensured.

3.4 Simulation Results

This section simulates and verifies the effectiveness of the proposed controller in dealing with CPL changes and PV panel output power changes. At the same time, the dynamic characteristics of the proposed controller are compared with those of the traditional dual-loop PI controller to verify the superiority of the proposed method.

3.4.1 Parameter Setting

Simulations in a 350 V DC MG are performed to verify the effectiveness of the proposed control scheme. The basic parameters of the simulated system are shown in Table 3-1. Three scenarios are simulated, respectively.

Table 3-1 350V DC MG System Parameters

Parameter	Symbol	Value
Switching frequency	f_s/kHz	20
Inductor	L/mH	0.6
Capacitor	C /μF	800
Resistance	R_0/Ω	1000
voltage reference	V_{ref}/V	350
CPL	P_{CPL}/W	3000
Irritation	Ir/W/m^2	1000
Temperature	T/℃	25

3.4.2 Verification of the Proposed Strategy

1) **CPL changes:** The first simulation is conducted to evaluate whether this control strategy can effectively control the output voltage in the face of severe fluctuations in CPL and sustain the PV panels at MPP. The tested environmental conditions are 1000 W/m² and 25℃. Fig. 3.8 depicts the performance of the controller dealing with the variation of the CPL. According to the P-V curve of the PV panel, the theoretical maximum power is 1750W. CPL reference shifted from 3 kW to 3.2 kW at 1.0s and then decreased to 2.6 kW at 2.0s, and finally jumped to 3.2kW at 3.0s. The proposed NDO-backstepping controller keeps the DC-bus tightly around its setpoint,

with below 1% overshoot and below 0.1s settling time.

In order to increase the fairness of the comparison, when adjusting the dual-PI controller parameters, it is ensured that the control effects of the two controllers are equivalent when the CPL changes for the first time. The overshoot is 4V and the settling time is 0.5s. Compared to the PI controller, the proposed controller has a smaller overshoot and shorter settling time. It is obvious that the proposed controller is significantly better than the traditional dual-loop PI controller when the CPL undergoes more drastic changes.

The curves of the power of the PV overlap. It is worth noting that no matter whether the proposed controller or the traditional dual-loop PI controller is used, the PV panels maintained their operation at the MPP throughout the whole period. This simulation result indicates that the proposed DC MG architecture and backstepping controller can effectively cope with sudden changes in CPL without causing significant obstacles to the energy harvesting of PV panels.

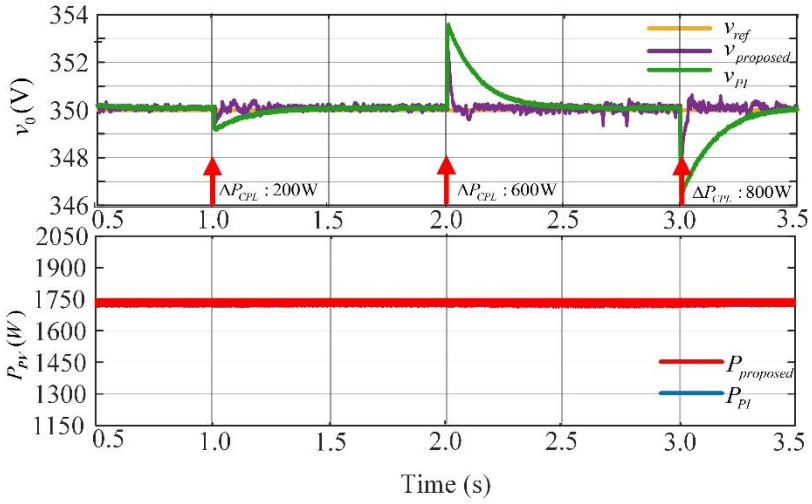

Fig. 3.8 Simulation results of the CPL variations

2) **PV Panels under irradiance change:** Another simulation is conducted to evaluate the performance of the DC MG system under conditions that PV panels experience fluctuations of irradiance levels, assessing whether each panel can operate at the MPP and whether there is any influence of the DC high voltage, which is important for voltage sensitive load equipment. Fig. 3.9 illustrates the result of the bus voltage and the harvested PV energy. According to the P-V curves, the theoretical

maximum power output of the panels is 1750 W and 1575 W, respectively. The irradiance adjusts from 1000 W/m^2 to 900 W/m^2 at 2.0s. For the proposed controller and dual-PI controller, the voltage of the high voltage bus has less impact under irradiance changes. This simulation result verifies the effectiveness of the ESS to absorb the excess power and compensate for the lack of power.

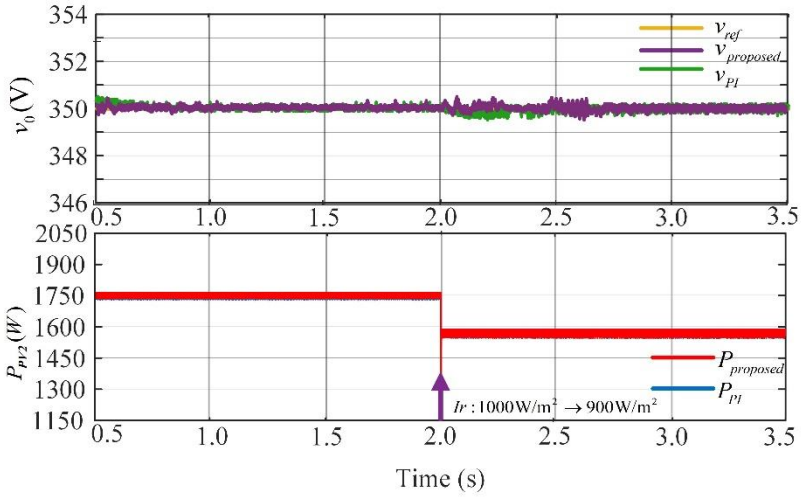

Fig. 3.9 Simulation results of the CPL variations with different irradiance conditions

3.5 Conclusion

This chapter presents a novel architecture of the DC MG with an effective nonlinear control strategy for ensuring voltage stability in the DC bus with CPLs. This architecture also maximizes energy harvesting from PV systems by using an ESS. The proposed backstepping controller with an NDO demonstrates robust performance in handling the challenges posed by fluctuating CPLs. The control method's ability to stabilize the bus voltage under dynamic conditions enables efficient integration of renewable energy into DC MGs, offering a promising solution for energy efficiency improvements. The simulation results validate the effectiveness of the controller, suggesting its potential for real-world applications in renewable energy-powered DC MGs. It is worth mentioning that the proposed control scheme can achieve the simultaneous functionalities of dynamic maximum energy harvesting and robust bus voltage regulation.

Chapter 4 Robust Model Predictive Control for Onboard Interleaved Multilevel Boost DC-DC Converter in DC Shipboard Microgrids

4.1 Introduction

DC microgrids (MGs) are gaining increasing industrial applications due to their convenient incorporation of various distributed energy resources (DERs), such as distributed generators (DGs), renewable energy sources (RESs), and energy storage systems (ESSs). Considering that DC MGs have a simple control architecture and are free of synchronization, they are widely applied in electric transportation systems, smart homes, electric aircraft, and shipboards [103]. Many studies have reported that DC systems can achieve better performance in terms of system efficiency, operational flexibility, component size, etc. [42, 104] than AC systems. In particular, DC systems are emerging as a promising technology for future shipboard applications. They enable the seamless integration of electronic loads, renewable energy sources, battery storage, and other advanced energy appliances without the need for complex synchronization or P/Q balancing. This results in key benefits such as reduced distribution losses, simplified control requirements, higher scalability, and improved user-friendliness. Furthermore, advancements in power electronics have made it convenient for DC systems to easily integrate AC appliances via inverters, offering high controllability and enhanced power supply flexibility. By introducing DC power systems on board, ships can reduce the fuel consumption of traditional diesel generators, improve electrical performance such as voltage stability, and minimize harmonic distortion, ultimately enhancing overall power quality. A typical DC shipboard microgrid (SMG) can be depicted in Fig. 4.1 [105, 106]. Different energy sources and loads can be hosted in DC SMGs, including PVs, batteries, fuel cells, DC generators, propulsion motors, and LEDs [107]. According to the recently released guideline “DC Power Distribution Systems for Marine and Offshore Applications” by

the American Bureau of Shipping (ABS), the recommended continuous voltage variation for DC power distribution systems shall remain within ±10%, with voltage ripple kept below 10%. These guidelines also emphasize minimizing the impact of abnormal conditions, such as sudden load changes and transient overvoltages, to ensure the stability and reliability of electrical components [108].

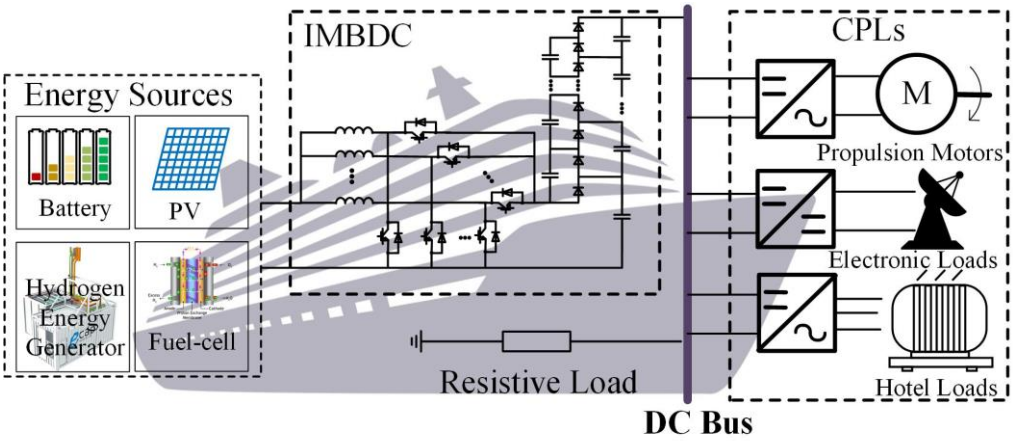

Fig. 4.1 A typical IMBDC-interfaced DC SMG

Considering the low and varying terminal voltages of DERs, suitable interfacing converters are necessary for adapting the DERs to the common DC bus. The conventional boost converter (CBC) is an acceptable solution. However, due to the inevitable parasitic impedance, its actual voltage gain is limited. Besides, it is difficult for CBC to achieve low current ripple and high power density simultaneously when interfacing fuel cells and batteries [108, 109]. Several other types of boost converters have been reported to overcome these defects. As one of the potential solutions, the interleaved boost converter (IBC) has been proposed in [97, 109, 110] to reduce input current ripples and increase the power capacity. The interleaved parallel structure can attenuate the input current ripple as low as 1.18%, effectively [110]. The interleaved structure facilitates the use of small-sized inductors without degrading the power quality, consequently improving the power density. A DC-DC multilevel boost converter (MBC), connected to a group of capacitors at the output terminal, is a suitable alternative to increase the voltage conversion ratio [90]. In this way, a high voltage gain and low capacitor voltage stress can be easily achieved by utilizing the switched-capacitor network. In view of the pros and cons of the boost circuit

topologies, an interleaved multilevel boost DC-DC converter (IMBDC), featuring the merits of IBC and MBC, is proposed as a suitable boost converter for interfacing different DERs in this work.

One of the primary advantages of DC systems is their flexibility as power hubs, capable of integrating diverse power sources such as fuel cells, batteries, and renewable energy systems. However, ship operations impose stringent requirements on system stability. Considering the dynamic operational environment of ships, the integration of renewable energy sources and the extensive use of power conversion interfaces in shipboard systems collectively pose significant challenges to the stability of DC shipboard microgrids (SMGs). In SMGs, different loads, including propulsion motors, shipboard hotel loads, and other electronic equipment, draw constant power as per system commands, which can be deemed as a constant power load (CPL) [111]. They are generally responsible for navigation, communication, passenger safety, etc., which is critical for the safe operation of SMGs. It is important to maintain a stable DC bus voltage for their reliable power supply. However, considering the high non-linearity and negative impedance of CPLs, the large fluctuation of the DERs and migration of the system operating condition, as well as other large-signal disturbances, will easily destabilize the DC bus voltage [112]. Therefore, it is necessary to explore a robust control strategy to maintain the bus voltage stability of the DC SMGs against large possible disturbances.

Many active and passive control strategies have been reported to stabilize the bus voltage against the detrimental effects of CPLs [17, 113]. Adding passive elements like resistors [17], capacitors [18], or LC filters [19] can increase the DC MG system's damping. However, deployments of extra physical components will increase costs and induce extra power loss. Unlike passive control, active damping schemes [92, 113] can emulate the functions of the passive components via the modification of control loops, consequently replacing the passive components with equivalent virtual impedances. The active and passive damping control can be categorized into linear control methods. They can only guarantee DC MG system stability in a small range around the system's pre-designed equilibriums. The stability of the DC MG system

can easily be jeopardized when encountering large-signal disturbances, such as significant variations of DER and CPL setting points.

Alternatively, the nonlinear approach takes into account the intrinsic nonlinearity of switched converters and can hence enhance the DC MGs' stability margin, effectively [114]. Common non-linear approaches, including passivity-based control (PBC), sliding mode control (SMC), Takagi-Sugeno (TS) fuzzy control, backstepping control, etc., have been reported to stabilize the bus voltage of CPL-integrated DC MGs [22, 81, 87, 115-118]. In [115], a model-free intelligent single input interval type 2 fuzzy PI controller (iSIT2-FPI) is designed based on SMC, which is applied in a full-electric ferry (FEF) ship with RESs and ESSs. To solve the negative impedance-induced instabilities in DC MGs, a control strategy consists of an extended state observer (ESO), an intelligent single input interval type-2 fuzzy PI controller (iSIT2-FPI) based on sliding mode control (SMC), and a model-free SMC controller. The ESO is used to estimate the uncertain dynamics of the system based on input-output parameters. The SMC controller is implemented to eliminate the estimation error of the ESO. Compared with conventional MPC controls, the iSIT2-FPI method shows better robustness and practicability. However, its intrinsic SMC schemes suffer from the voltage-chattering phenomenon. Besides, extra deployment of output current transducers is necessary in SMC, and this will raise the overall cost. To suppress the chattering, a composite robust discrete quasi-sliding mode control (DQSMC) has been reported in [116]. This approach introduces a robust DQSMC voltage controller with a discrete integral sliding surface and a second-order sliding mode disturbance observer for disturbance estimation and compensation. It can enhance the system’s robustness and alleviate inherent chattering. In [22], a TS fuzzy control law is used for regulating the current of the uncertain energy storage unit in a DC MG. The robust nonfragile controller utilizes digital approximations of continuous-time control laws. It can compensate for system uncertainties and unknown parameter variations. In [21, 118], backstepping controllers are proposed to stabilize the DC-DC converter system with CPLs. However, compared with the model predictive control (MPC) algorithm, its dynamic response is considerably slower. The MPC generates the control signal by

resolving an optimization problem that considers the nonlinearities of the system and future behavior over a time horizon. As a result, the MPC approach is particularly effective for stabilizing DC SMG with dynamically varying and sensitive loads, such as pulsed power loads (PPL) and CPLs [108, 119]. In view of these, there still lacks a new control scheme to achieve the offset-free tracking of reference values against fast-varying disturbances.

To remedy this research gap, a compound large-signal stabilizer is proposed for the IMBDC to regulate the DC SMG with a significant amount of CPLs. The key contributions can be summarized as follows:

1) **Generalized Reduced-Order Modeling:** A generalized reduced-order M-phase N-level IMBDC model is derived to simplify the follow-up large-signal stabilizer design.
2) **Fast and Precise Disturbance Estimation:** A high-order NDO is designed to estimate external disturbances and the output power of the IMBDC within a finite time, simultaneously. It can reduce the use of current sensors and contribute to fast dynamic responses.
3) **Fast Voltage Regulation:** An offset-free MPC stabilizer is designed to tackle the aforementioned challenges perceived in nonlinear studies. The combination of the developed model and high-order NDOs can ensure the large-signal stability of the DC MG system, considering the negative impacts of CPLs and system uncertainties.
4) **Inter-Phase Current Balance:** An inter-phase current balancing controller (IPCBC) is introduced to maintain equal current sharing among M-parallel inductors, benefiting from decreased heat loss and extended lifespan.

In the context of the DC SMG, renewable sources are primarily composed of PV units and ESSs, which align directly with the system components investigated in the preceding chapter. Based on these findings, this chapter shifts the focus toward advanced stabilization strategies. For this purpose, the PV–ESS subsystem is equivalently represented as a DC source, thereby enabling a focused investigation on the control of the IMBDC-interfaced DC bus under the influence of CPLs.

4.2 Reduced-order Modeling of an IMBDC-enabled DC SMG

The simplified topology of the M-phase N-level IMBDC in the shipboard SMG can be depicted in Fig. 4.2. The power electronic loads, such as adapter-interfaced motors and resistive loads, can be modeled as CPLs. The M-phase interleaved inductors, which are used to achieve low input current ripple and high power density, are located on the left side of the IMBDC. The right-hand-side N-level switched-capacitor circuit is used to boost the voltage gain at high conversion efficiency. The resistive load is denoted as R_0, while P_{CPL} is the power of the CPL.

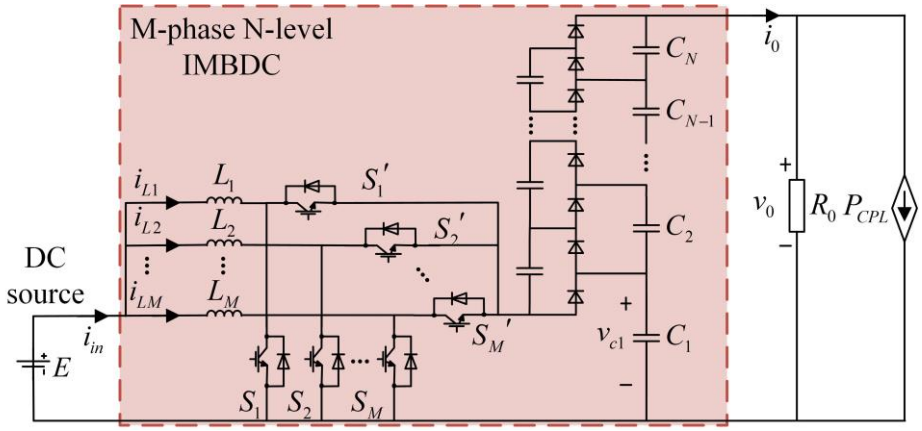

Fig. 4.2 The simplified topology of an IMBDC-enabled DC SMG

$$\begin{cases} L_1 \dfrac{di_{L1}}{dt} = E - (1-d_1)\dfrac{v_o}{N} \\ L_2 \dfrac{di_{L2}}{dt} = E - (1-d_2)\dfrac{v_o}{N} \\ \ddots \qquad \ddots \qquad \ddots \\ L_M \dfrac{di_{LM}}{dt} = E - (1-d_M)\dfrac{v_o}{N} \\ C\dfrac{dv_o}{dt} = \dfrac{N}{1+(\sum_{m=1}^{M} d_m)/M}\left[\sum_{m=1}^{M}(1-d_m)i_{Lm} - i_o\right] \end{cases} \tag{4.1}$$

where M and N are the numbers of the input inductors and output capacitors. i_{Lm} is the current flowing through the m-phase inductor L_m, (m = 1, 2, ⋯, M) and v_0 represents the output voltage. Besides, E and d_m, (m = 1, 2, ⋯, M) represent the converter input voltage and duty ratio of the m-th phase switch S_m. i_0 is the output current and it

equals to $v_0/R_0 + P_{CPL}/v_0$.

Practically, the configurations of all phases are identical and the same duty ratios (d=d_m, m =1, 2, ···, M) are applied with $2\pi/M$ phase shifts. In the circuit, all inductors are equal $L_1 = L_2 = \cdots = L_0$ and all capacitors are equal $C_1 = C_2 = \cdots = C$. Consequently, the reduced-order model for M-phase N-level IMBDC can be obtained from (4.1) as

$$\begin{cases} L_{eq}\dfrac{di_{in}}{dt} = E - (1-d)\dfrac{v_o}{N} \\ C\dfrac{dv_o}{dt} = \dfrac{N}{1+d}\left[(1-d)i_{in} - i_o\right] \end{cases} \tag{4.2}$$

where $i_{in} = \sum_{m=1}^{M} i_{Lm}$ is the total input current and $L_{eq} = L_0/M$ is the equivalent input inductor.

In the long-term dynamic operations, circuit component properties, including capacitance and inductance, will inevitably migrate from their nominal values. As these inherent uncertainties are difficult to quantify, it is nearly impossible to acquire the exact values online. Without loss of generality, the uncertainties of the inductor and capacitor can be considered as disturbances in modeling. Therefore, the reduced-order model of the IMBDC can be summarised as:

$$\begin{cases} (L_{eq} + \Delta L)\dfrac{di_{in}}{dt} = E - (1-d)\dfrac{v_o}{N} \\ (C + \Delta C)\dfrac{dv_o}{dt} = \dfrac{N}{1+d}\left[(1-d)i_{in} - i_o\right] \end{cases} \tag{4.3}$$

where ΔL and ΔC are the uncertainties in inductance and capacitance, respectively. Moreover, the output power of the IMBDC can be given by

$$P_L = v_o^2 / R_0 + P_{CPL} \tag{4.4}$$

Letting the output voltage v_0 equal to the reference voltage v_0^{ref} , the reference of P_L^{ref} is

$$P_L^{\text{ref}} = \left(v_o^{\text{ref}}\right)^2 / R_0 + P_{CPL} \tag{4.5}$$

4.3 The Proposed Offset-free Model Predictive Stabilizer Design

In this section, the proposed compound large-signal stabilization controller is introduced. It synthesizes high-order NDOs and MPC algorithms to monitor and regulate the output voltage of the M-phase N-level IMBDC.

4.3.1 Coordinate Form Transformation

For the IMBDC system, the original state variables represented in Eq. (4.2) can be transformed into a collection of coordinates through the subsequent transformation.

$$\begin{cases} x_1 = \frac{1}{2} L_{eq} i_{in}^2 + \frac{1}{2}(2N-1) C \left(\frac{v_o}{N} \right)^2 \\ x_2 = E i_{in} \end{cases} \tag{4.6}$$

The dynamics of x_1 and x_2 can be expressed as

$$\begin{cases} \dot{x}_1 = L_{eq} i_{in} \dot{i}_{in} + \frac{2N-1}{N^2} C v_o \dot{v}_o \\ \dot{x}_2 = E \dot{i}_{in} \end{cases} \tag{4.7}$$

By defining that

$$\begin{cases} \dot{x}_1 = x_2 + u_1 \\ \dot{x}_2 = \gamma + u_2 \end{cases} \tag{4.8}$$

Substituting Eqs. (4.3), (4.7) into Eq. (4.8), the model expressed in Eq. (4.7) can be reformulated to be uniform as

$$\begin{cases} \gamma = \frac{E}{L_{eq}} [E - (1-d) \frac{v_o}{N}] \\ u_1 = -(1-d) \frac{v_o i_{in}}{N} - \frac{\Delta L i_{in}}{L_{eq} + \Delta L} \left[E - (1-d) \frac{v_o}{N} \right] \\ + \frac{2N-1}{N(1+d)} \frac{C v_o}{C + \Delta C} \left[(1-d) i_{in} - i_o \right] \\ u_2 = -\frac{\Delta L}{L_{eq}(L_{eq} + \Delta L)} \left[E^2 - (1-d) \frac{E v_o}{N} \right] \end{cases} \tag{4.9}$$

Specifically, the u_1 and u_2 is from:

$$
\begin{aligned}
u_1 &= \dot{x}_1 - x_2 \\
&= L_{eq} i_{in} \dot{i}_{in} + \frac{2N-1}{N^2} C v_o \dot{v}_o - E i_{in} \\
&= L_{eq} i_{in} \frac{1}{L_{eq} + \Delta L} [E - (1-d)\frac{v_o}{N}] - E i_{in} \\
&\quad + \frac{2N-1}{N^2} C v_o \frac{1}{C + \Delta C} \frac{N}{1+d} [(1-d) i_{in} - i_o] \\
&= -(1-d)\frac{v_o i_{in}}{N} - \frac{\Delta L}{L_{eq} + \Delta L} [E - (1-d)\frac{v_o}{N}] \\
&\quad + \frac{2N-1}{N(1+d)} \frac{C v_o}{C + \Delta C} [(1-d) i_{in} - i_o]
\end{aligned}
\tag{4.10}
$$

and

$$
\begin{aligned}
u_2 &= \dot{x}_2 - \gamma \\
&= E \frac{1}{L_{eq} + \Delta L} [E - (1-d)\frac{v_o}{N}] - \frac{E}{L_{eq}} [E - (1-d)\frac{v_o}{N}] \\
&= \frac{-\Delta L}{L_{eq}(L_{eq} + \Delta L)} [E^2 - (1-d)\frac{E v_o}{N}]
\end{aligned}
\tag{4.11}
$$

In Eqs. (4.8), (4.9), and (4.11), γ is the intermediate control signal. u_1 and u_2 are two unmeasurable disturbances.

The duty ratio d can be derived from γ as

$$
d = 1 - \frac{NE}{v_o} + \frac{NL\gamma}{MEv_o} \tag{4.12}
$$

By employing the newly defined dynamic states x_1 and x_2, the original control objective of regulating v_0 to v_0^{ref} can be transformed to make x_1 and x_2 converge to their respective references x_1^{ref} and x_2^{ref}. According to Eqs. (4.5) and (4.6), x_1^{ref} and x_2^{ref} can be identified as

$$
\begin{cases}
x_1^{\text{ref}} = \dfrac{1}{2} L_{eq} \left(\dfrac{P_L^{\text{ref}}}{E} \right)^2 + \dfrac{1}{2}(2N-1) C \left(\dfrac{v_o^{\text{ref}}}{N} \right)^2 \\
x_2^{\text{ref}} = P_L^{\text{ref}}
\end{cases}
\tag{4.13}
$$

4.3.2 High-Order NDO Design

In this part, a high-order NDO is constructed to estimate the disturbances and

uncertainties for improving the control dynamics. The following assumptions can be made since the disturbances and uncertainties (i.e., u_1 and u_2) are brought mainly by power disturbances and the uncertainty of circuits.

Assumption 1: The load power is unknown, but the nominal circuit parameters, including input voltage *E*, nominal inductance L_0, and nominal capacitance C_0 are known.

Assumption 2: The disturbances $u_i(t), i = 1, 2$ are bounded

$$\sup_{t>0} \left| \frac{d^r u_i(t)}{dt^r} \right| \le \sigma, r = 0, 1, 2, 3 \tag{4.14}$$

where σ is a known positive constant.

Observed from Eq. (4.9), unmeasurable disturbances u_1 and u_2 have direct impacts on the system's nominal performance. The high-order NDO technique introduced in [102, 114] can be adopted to estimate u_1 and u_2 so that their negative consequences can be mitigated accordingly.

$$\begin{cases} \hat{u}_1 = g_{11} + l_{11} x_1, \dot{g}_{11} = -l_{11}(x_2 + \hat{u}_1) + \hat{\dot{u}}_1 \\ \hat{\dot{u}}_1 = g_{12} + l_{12} x_1, \dot{g}_{12} = -l_{12}(x_2 + \hat{u}_1) + \hat{\ddot{u}}_1 \\ \hat{\ddot{u}}_1 = g_{13} + l_{13} x_1, \dot{g}_{13} = -l_{13}(x_2 + \hat{u}_1) \end{cases} \tag{4.15}$$

$$\begin{cases} \hat{u}_2 = g_{21} + l_{21} x_2, \dot{g}_{21} = -l_{21}(\gamma + \hat{u}_2) + \hat{\dot{u}}_2 \\ \hat{\dot{u}}_2 = g_{22} + l_{22} x_2, \dot{g}_{22} = -l_{22}(\gamma + \hat{u}_2) + \hat{\ddot{u}}_2 \\ \hat{\ddot{u}}_2 = g_{23} + l_{23} x_2, \dot{g}_{23} = -l_{23}(\gamma + \hat{u}_2) \end{cases} \tag{4.16}$$

where $l_{ij} (i = 1, 2; j = 1, 2, 3)$ are positive adjustable high-order NDO gains to be designed. g_{ij} are the additional variables. $\tilde{u}_i$, $\tilde{\dot{u}}_i$, and $\tilde{\ddot{u}}_i$ can be defined as the observation errors of u_i, $\dot{u}_i$, and $\ddot{u}_i$. These errors and their dynamics can be expressed as

$$\begin{cases} \tilde{u}_i = u_i - \hat{u}_i, \dot{\tilde{u}}_i = -l_{i1} \tilde{u}_i + \tilde{\dot{u}}_i \\ \tilde{\dot{u}}_i = \dot{u}_i - \hat{\dot{u}}_i, \dot{\tilde{\dot{u}}}_i = -l_{i2} \tilde{u}_i + \tilde{\ddot{u}}_i \\ \tilde{\ddot{u}}_i = \ddot{u}_i - \hat{\ddot{u}}_i, \dot{\tilde{\ddot{u}}}_i = -l_{i3} \tilde{u}_i + \dddot{u}_i \end{cases} \tag{4.17}$$

According to Eq. (4.17), since $\dddot{u}_i$ is bounded by σ, it is possible to choose suitable $l_{i1}>0$, $l_{i2}>0$, and $l_{i3}>0$ to ensure the finite-time convergence of $\tilde{u}_i$. By observing that the high-order NDO can estimate $\tilde{u}_i$, $\dot{\tilde{u}}_i$, and $\ddot{\tilde{u}}_i$ simultaneously, it can be deduced that the estimation accuracy and dynamic responses of the adopted observers are better than those of common first-order NDO [97].

Generally, because $\Delta L \ll L_0$ and $\Delta C \ll C_0$, it is rational to consider $P_L = -u_1$. Based on Eqs. (4.5), (4.13), and (4.17), the estimations of x_1^{ref} and x_2^{ref} are given by

$$\begin{cases} \hat{x}_1^{\text{ref}} = \dfrac{1}{2} L_{eq} \left(\dfrac{-\hat{u}_1}{E} \right)^2 + \dfrac{2N-1}{2N^2} C \left(v_0^{\text{ref}} \right)^2 \\ \hat{x}_2^{\text{ref}} = -\dfrac{L_{eq}}{E^2} \hat{u}_1 \hat{\dot{u}}_1 \end{cases} \tag{4.18}$$

4.3.3 Offset-Free Model Predictive Stabilizer Design

Considering Eqs. (4.8), (4.9) and (4.18), the reference of the intermediate control signal γ^{ref} can be represented as:

$$\hat{\gamma}^{\text{ref}} = \dot{x}_2^{\text{ref}} = \frac{L_{eq}}{E} [(\hat{u}_1)^2 + \hat{u}_1 \cdot \hat{\ddot{u}}_1] \tag{4.19}$$

where $\hat{u}_1$ is the observed disturbance, $\hat{\dot{u}}_1$ and $\hat{\ddot{u}}_1$ are the observed values of the first and second derivatives of disturbance u_1, respectively. According to MPC, the general objective function can be described:

$$J = \sum_{i=1}^{P} \left[y(k+\Gamma_i) - w(k+\Gamma_i) \right]^2 + \sum_{j=1}^{M} \left[\Delta u(k+\Gamma_i - 1) \right]^2 \tag{4.20}$$

where $y(k+\Gamma_i)$ represents the target state at the time Γ_i, and $w(k+\Gamma_i)$ represents the target reference state at the time Γ_i. $\Delta u(k+\Gamma_i - 1)$ represents the difference between the reference control quantity and the actual control quantity. To simplify the cost function, this section uses the future output $y(t+\tau)$ as the target. Firstly, the Taylor series expansion is used to express $y(t+\tau)$.

$$y(t+\tau)=y(t)+\tau\dot{y}(t)+\frac{\tau^2}{2}\ddot{y}(t)+\frac{\tau^3}{6}\dddot{y}(t) \tag{4.21}$$

where τ is the prediction step size, with a range of $\tau\in(0,T)$. T is the predictive period. Combining Eq. (4.8) can be further expressed as:

$$y(t+\tau)=x_1+\tau x_2+\frac{\tau^2}{2}\gamma+\frac{\tau^3}{6}\dot{\gamma}=\begin{pmatrix}\bar{K} & \tilde{K}\end{pmatrix}\begin{pmatrix}X\\ Y\end{pmatrix} \tag{4.22}$$

where $\bar{K}=(1,\tau)$, $\tilde{K}=(\tau^2/2,\tau^3/6)$, $X=(x_1,x_2)^{\mathrm{T}}$ and $Y=(\gamma,\dot{\gamma})^{\mathrm{T}}$.

Based on Eq. (4.22), the objective function is defined as:

$$\begin{aligned}J(t)&\triangleq\frac{1}{2}\int_0^T\left[y(t+\tau)-w(t+\tau)\right]^2d\tau\\&=\frac{1}{2}\begin{pmatrix}\Delta X^{\mathrm{T}} & \Delta Y^{\mathrm{T}}\end{pmatrix}\begin{pmatrix}K_1 & K_2\\ K_2^{\mathrm{T}} & K_3\end{pmatrix}\begin{pmatrix}\Delta X\\ \Delta Y\end{pmatrix}\end{aligned} \tag{4.23}$$

where $\Delta X=(x_1-x_1^{\mathrm{ref}},x_2-x_2^{\mathrm{ref}})$, $\Delta Y=(\gamma-\gamma^{\mathrm{ref}},\dot{\gamma}-\dot{\gamma}^{\mathrm{ref}})$. K_1, K_2 and K_3 can be expressed as

$$\begin{cases}K_1=\int_0^T\bar{K}^{\mathrm{T}}\bar{K}d\tau=\begin{pmatrix}1 & \tau\\ \tau & \tau^2\end{pmatrix}\\ K_2=\int_0^T\bar{K}^{\mathrm{T}}\tilde{K}d\tau=\begin{pmatrix}\tau^2/2 & \tau^3/6\\ \tau^3/2 & \tau^4/6\end{pmatrix}\\ K_3=\int_0^T\tilde{K}^{\mathrm{T}}\tilde{K}d\tau=\begin{pmatrix}\tau^4/4 & \tau^5/12\\ \tau^5/12 & \tau^6/36\end{pmatrix}\end{cases} \tag{4.24}$$

The optimal solution of this cost function can be obtained by taking a partial derivative of $J(t)$ with respect to Y^{T}, i.e.,

$$\frac{\partial J}{\partial Y^{\mathrm{T}}}=\frac{1}{2}\frac{\partial\Delta Y^{\mathrm{T}}}{\partial Y^{\mathrm{T}}}\left(K_2^{\mathrm{T}}\Delta X+K_3\Delta Y\right)=0 \tag{4.25}$$

where $\partial\Delta Y^{\mathrm{T}}/\partial Y^{\mathrm{T}}$ is a non-singular part. Thus, the only solution is to let $K_2^T\Delta X+K_3\Delta Y=0$. It can be rewritten as:

$$Y=Y^{\mathrm{ref}}-K_3^{-1}K_2^{\mathrm{T}}(X-X^{\mathrm{ref}}) \tag{4.26}$$

By considering Eq. (4.12), the intermediate control signal γ directly affects d. According to Eq. (4.26), γ can be rewritten as

$$\gamma = \gamma^{\text{ref}} - k_0(x_1 - x_1^{\text{ref}}) - k_1(x_2 - x_2^{\text{ref}}) \tag{4.27}$$

where k_0 and k_1 are the values of the first row of the matrix $K_3^{-1}K_2^{\text{T}}$. By taking the disturbance into the MPC stabilizer, combined with Eq. (4.8), the intermediate control signal can be obtained.

$$\gamma = \gamma^{\text{ref}} - \hat{u}_2 - k_0(x_1 - x_1^{\text{ref}}) - k_1(x_2 - x_2^{\text{ref}} + \hat{u}_1) \tag{4.28}$$

By feeding the intermediate control signal γ to Eq. (4.12), the closed-loop control logic of the proposed large-signal stabilizer for the IMBDC system is accomplished.

According to Eqs. (4.18), (4.19), and (4.28), the MPC controller utilizes the disturbance values observed by the NDO to compute the real-time reference values for each state variable. Additionally, the system disturbance values $\hat{u}_1$ and $\hat{u}_2$ observed by the NDO are used to continuously adjust the control variables. This approach is essential for handling rapidly changing nonlinearities or external disturbances. The MPC controller can predict future behavior and optimize control actions based on this feedback to achieve offset-free control of the control target. By integrating a high-order NDO with the MPC, the control system can better adapt to unknown disturbances and circuit parameter drifts, significantly enhancing both the robustness and dynamic response performance of the system.

4.3.4 Large-Signal Stability Analysis

In this section, a rigorous Lyapunov's stability analysis is performed for the IMBDC system with the proposed MPC algorithm. According to Lyapunov's stability theorem, for any linear or nonlinear system, the system is globally asymptotically stable if a function can satisfy: for all x, $V(0)=0$; $V(x)>0$; $dV/dt<0$;

To establish a Lyapunov function V:

$$\begin{cases} V = \dfrac{1}{2}Z_1^2 + \dfrac{1}{2}Z_2^2 + \dfrac{1}{2}\tilde{u}_1^2\dfrac{1}{2}\tilde{u}_2^2 \\ Z_1 = x_1 - x_1^{\text{ref}} \\ Z_2 = x_2 - x_2^{\text{ref}} \\ Z_3 = \gamma - \gamma^{\text{ref}} \end{cases} \tag{4.29}$$

where Z_1 and Z_2 represent the difference between state value x_1 and x_2 and their reference values, respectively. By combining Eqs. (4.8), (4.17), and (4.28), the derivative of the Lyapunov function V can be derived as

$$\begin{aligned}\dot{V} &= Z_1 Z_2 + Z_2 Z_3 + Z_1 u_1 + Z_2 u_2 + \tilde{u}_1 \dot{\tilde{u}}_1 + \tilde{u}_2 \dot{\tilde{u}}_2 \\ &= \left(1-k_0\right) Z_1 Z_2 + Z_2 \tilde{u}_2 + Z_1 u_1 - k_1 Z_2^2 - k_1 Z_2 \hat{u}_1\end{aligned} \tag{4.30}$$

where Z_3 represents the difference between γ and its reference value. Since the value of Z_3 is very small, and our Z_3 will eventually converge to zero, in this case, we might as well assume that Z_3=0. Eq. (4.30) can be rewritten as:

$$\begin{aligned}\dot{V} = &\frac{k_0\left(k_0-1\right)}{k_1} Z_1{}^2 - k_1 Z_2{}^2 + Z_1 \tilde{u}_1 + Z_2 \tilde{u}_2 - \frac{1-k_0}{k_0} Z_2 \hat{u}_2 + \frac{1}{k_0} \hat{u}_1 \hat{u}_2 \\ &+2k_0 Z_1 \hat{u}_1 + k_1 \hat{u}_1{}^2 + \frac{1-k_0}{k_0 k_1} \hat{u}_2{}^2 - l_{11} \tilde{u}_1^2 - l_{21} \tilde{u}_2{}^2 + \tilde{u}_1 \dot{\hat{u}}_1 + \tilde{u}_2 \dot{\hat{u}}_2\end{aligned} \tag{4.31}$$

According to Young's inequality, $ab \le \frac{1}{2} a^2 + \frac{1}{2} b^2$, Eq. (4.29) can be rewritten as the following inequality.

$$\begin{aligned}\dot{V} &\le \left(\frac{k_0^2 - k_0}{k_1} + \frac{1}{2} + k_0\right) Z_1^2 + \left(\frac{1}{2k_0} - k_1\right) Z_2^2 + \left(1-l_{11}\right) \tilde{u}_1{}^2 + \left(1-l_{21}\right) \tilde{u}_2{}^2 + U \\ U &= \left(\frac{1}{2k_0} + k_0 + k_1\right) \hat{u}_1{}^2 + \left(\frac{2-k_0}{2k_0} + \frac{1-k_0}{k_0 k_1}\right) \hat{u}_2{}^2 + \frac{1}{2} \hat{u}_1{}^2 + \frac{1}{2} \hat{u}_2{}^2\end{aligned} \tag{4.32}$$

According to Eq. (4.14), the values of the disturbance observer have an upper bound. Obviously, U will also have a clear upper bound M. To make V stable for a finite period of time, the parameters need to satisfy:

$$\frac{k_0^2 - k_0}{k_1} + \frac{1}{2} + k_0 < 0, \frac{1}{2k_0} - k_1 < 0, 1 - l_{11} < 0, 1 - l_{21} < 0 \tag{4.33}$$

By selecting the stabilizer gains to satisfy Eq. (4.33) and ensure a sufficiently large ξ, the derivative of V can be rewritten:

$$\dot{V} \le -\frac{\xi}{2}\left(Z_1{}^2 + Z_2^2 + \tilde{u}_1^2 + \tilde{u}_2^2\right) + M \tag{4.34}$$

where $\xi = \min\left\{(k_0 - k_0^2)/k - 1/2 - k_0, -1/2k_0 + k_1, l_{11} - 1, l_{21} - 1\right\}$. We can conclude the Eq. (4.34) as

$$\dot{V} \le -\xi V + M \tag{4.35}$$

We can define a four-dimensional set of real numbers as $\Psi = \left\{ Z \in \mathbb{R}^4 \,|\, V(Z) \le M / \xi \right\}$. Thus, for any $Z \in \mathbb{R}^4 \setminus \Psi$, they will satisfy $V(Z) > M / \xi$. Then the following inequality must hold:

$$\dot{V}(Z) \le -\xi V + M < 0 \tag{4.36}$$

According to the Lyapunov stability principle, the closed-loop IMBDC system is asymptotically stable with the variables at steady states. Consequently, the DC bus voltage v_0 can track its reference value v_0^{ref} with negligible steady-state error. The large-signal stability of the proposed control is ensured.

4.3.5 Inter-Phase Current Balance Controller Design

Because only the lumped input current is utilized in the design of the observer-based MPC for the IMBDC, the inter-phase current imbalance may be caused by parameters and the duty ratio of each phase in practice. In the closed-loop IMBDC system, a straightforward IPCBC is used to address these problems. The main purpose is to enforce each phase's inductor current and to track its average value $i_{L,ave} = i_{in} / M = (\sum_{m=1}^{M} i_{Lm}) / M$. Traditionally, the inter-phase current balance is achieved by using PI controller [11]. However, in the electromagnetic timeframe, the CPL is susceptible to low frequency and subsynchronous oscillation. The current sharing performance can be enhanced by using proportional-resonance (PR) controllers. The IPCBC is designed as

$$d_m^{com} = k_p (i_{L,ave} - i_{Lm}) + \frac{k_r s}{s^2 + \omega_c^2} (i_{L,ave} - i_{Lm}), m \in [1, M] \tag{4.37}$$

where k_p and k_r represent the proportional and the resonant parameters, respectively. The proposed observer-based MPC is intended to have a control bandwidth that is substantially faster than the PR controller. The PR controller is frequently used for currents without low-frequency oscillation, and in this instance, ω_c=0. Consideration should be given to low-frequency oscillation with a frequency of less than 3 Hz for the IMBDC with high-density CPLs [120, 121]. The value of ω_c is chosen to be ω_c

=(1+3)/2=2 Hz in order to enhance capacity for these low-frequency components (1 Hz to 3 Hz). The IPCBC can be built to have a minimal impact on the stability of the system because of its sluggish response and tiny duty cycle modification by selecting a sufficiently low bandwidth and loop gains. Then, the final control law of each stage can be derived as

$$d_m = d + d_m^{com}, m \in [1, M] \tag{4.38}$$

Based on the above-mentioned design guideline, the control diagram of the proposed stabilizer is displayed in Fig. 4.3.

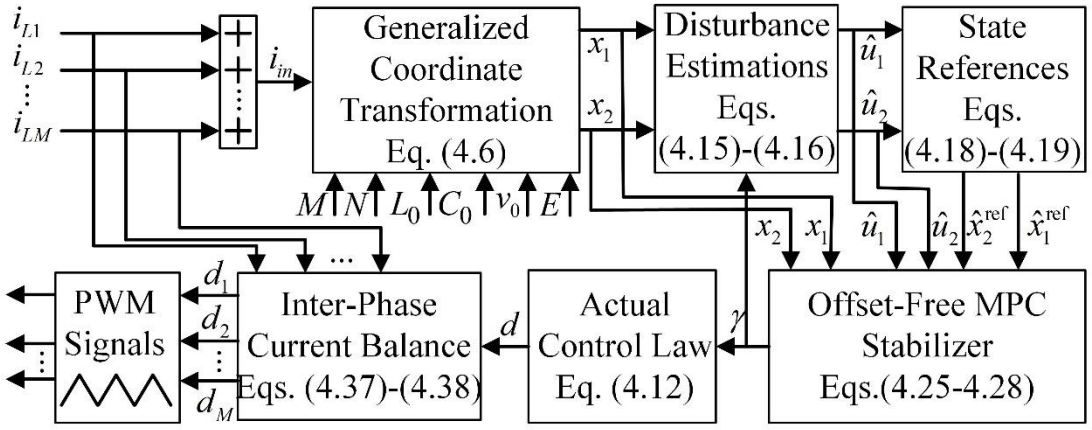

Fig. 4.3 Overall control diagram of the proposed stabilizer

4.4 Simulation Results

This section introduces a crucial control gain tuning guideline for the proposed stabilizer. The efficacy of the proposed control strategy is confirmed by several case studies.

4.4.1 Parameters Tuning Guideline

Since the proposed control consists of two high-order NDOs and one MPC stabilizer, both observer and MPC gains affect the dynamic performance of the regulated system. Thus, a critical parameter tuning guideline of the proposed compound stabilizer in the presence of a CPL step change (P_{CPL}=5 kW to P_{CPL}=10 kW at 0.50 s) is developed.

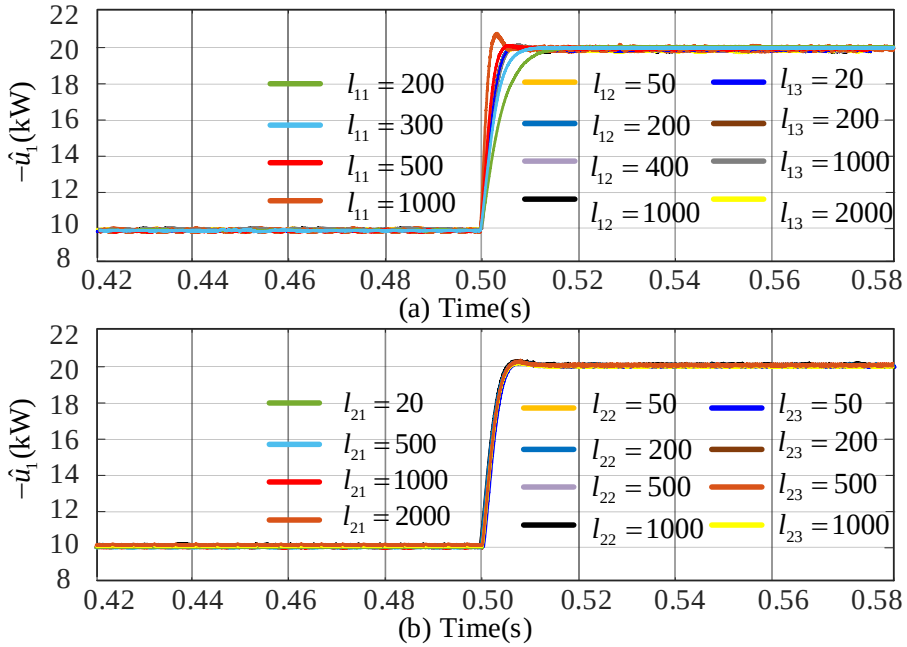

Fig. 4.4 Dynamic responses of the estimator $\hat{u}_1$ with various observer gains, (a) l_{11}, l_{12}, and l_{13}. (b) l_{21}, l_{22}, and l_{23}

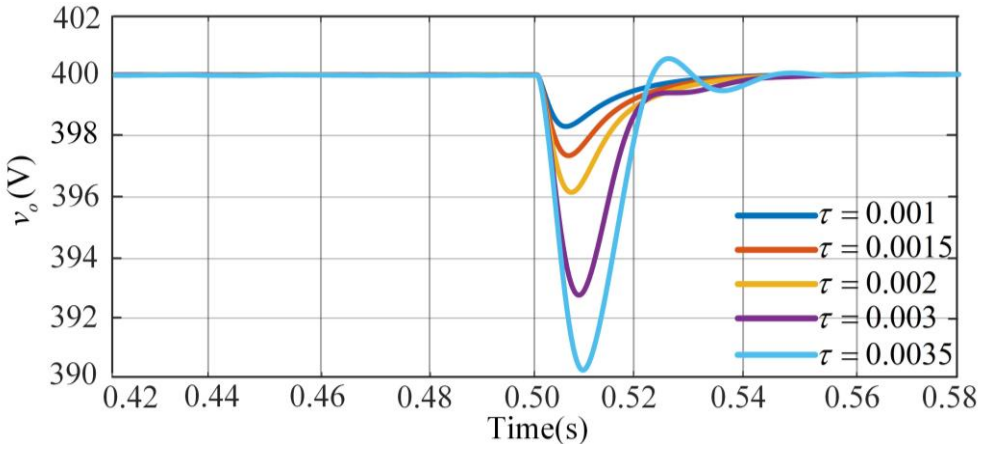

Fig. 4.5 Dynamic responses of the output voltage with various predictive periods

Fig. 4.4 depicts the dynamic responses of $\hat{u}_1$ with a 10-kW CPL step change. From Fig. 4.4 (a), it can be observed that the larger l_{11} is, the smaller the settling time of the observer. However, overly large l_{11} will result in the dynamic estimation response to have a significantly large overshoot. By trading off these two aspects, l_{11}=500 is selected. However, the observer's dynamic responses are not sensitive to the gains of l_{12} and l_{13}. In simulations, we set l_{12}=400 and l_{13}=200. Similarly, as shown in Fig. 4.4 (b), l_{21}, l_{22} and l_{23} have limited influence on the observer dynamic responses,

we configure l_{21}=500, l_{22}=200 and l_{23}=200.

The output voltage dynamics with respect to various MPC prediction periods are shown in Fig. 4.5. We configure the prediction step size of the MPC as τ=1.5 ms.

4.4.2 Proposed Control Strategy Verifications

1) **Effectiveness of IPCBC:** A comparison has been conducted to confirm the validity of the proposed IPCBC. We configure k_p=0.2 and k_r=8. P_{CPL} is changed from 2 kW to 3 kW at t=0.20 s. Fig. 4.6 (a) and Fig. 4.6 (b) show the output responses of the IMBDC system without and with IPCBCs, respectively. It is clear that the proposed IPCBC is capable of balancing the inter-phase inductor currents against significant CPL disturbance. Notably, the output voltage closely tracks its reference without any difference in both subfigures.

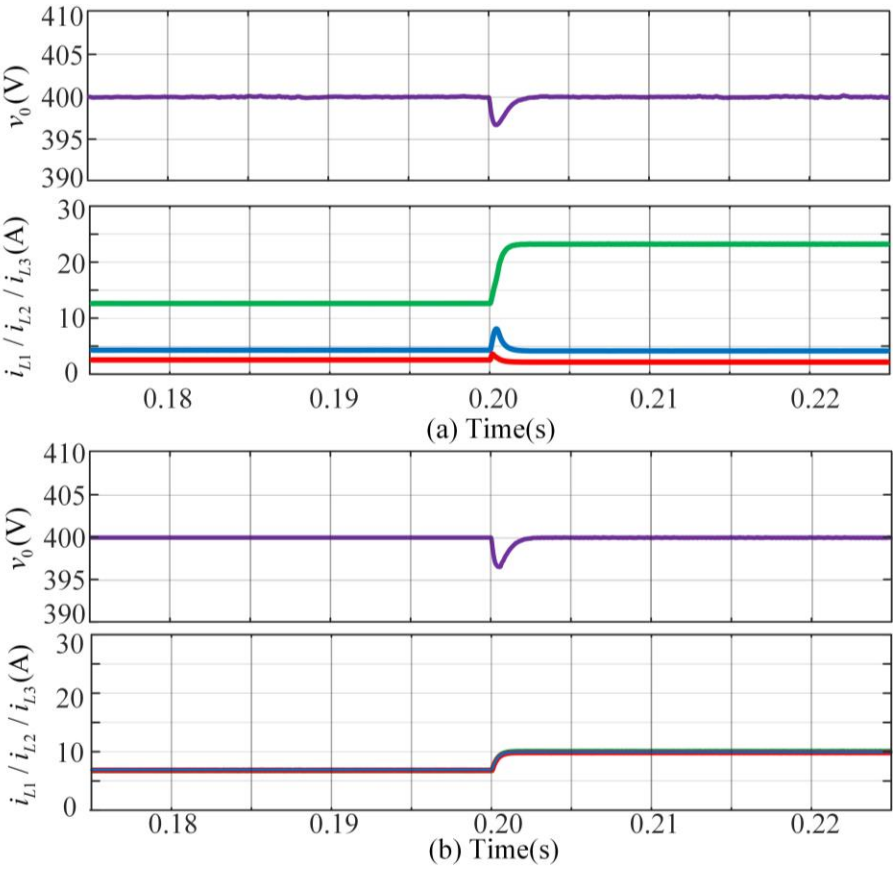

Fig. 4.6 Dynamic responses of a regulated IMBDC system (a) without IPCBCs, (b) with IPCBCs

2) **CPL Variations:** Fig. 4.7 depicts the dynamic responses of the IMBDC with the CPL variations. Initially, an 8 kW CPL is added to the system. Specifically, the CPL rises from 8 kW to 16 kW at 0.2 s while plunges to 12 kW at 0.3 s. It is noticed that the output voltage tracks its reference with a small settling time of 10 ms under each CPL variation. As shown in the three-phase inductor currents, the inter-phase current balance is achieved during the transients and steady states.

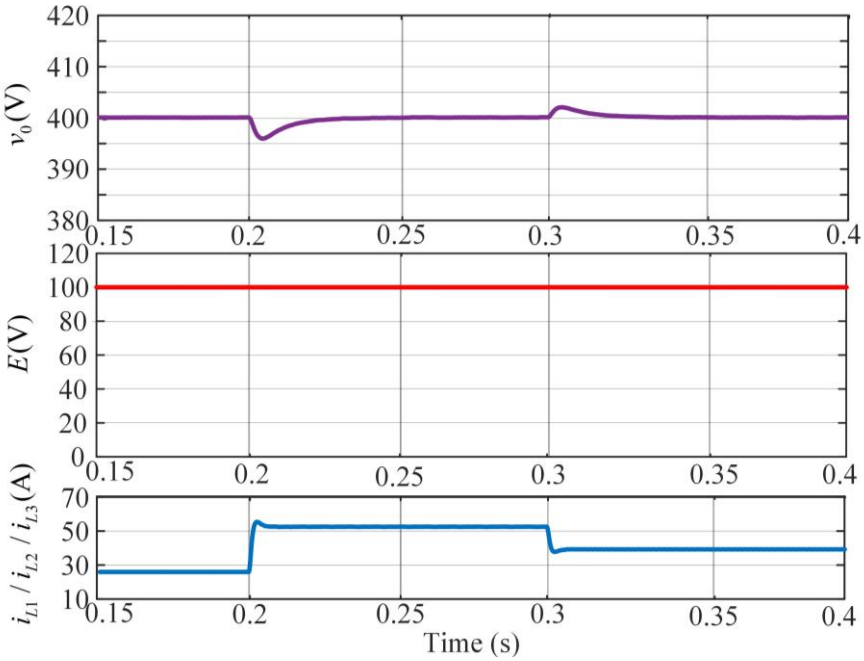

Fig. 4.7 Simulation results of the IMBDC with CPL variations

3) **Input Voltage Variations:** The dynamic responses of the IMBDC with respect to input voltage changes are shown in Fig. 4.8. In this case, the CPL is set as 8 kW. The input voltage drops from 100 V to 50 V at 0.20 s, then rises to 80 V at 0.3 s. It can be seen that the value of v_0 is precisely regulated at the reference with the rapid dynamic response (within 30 ms). Like the previous cases, the IPCBC likewise balances 3-phase inductor currents effectively.

4) **Output Voltage Reference Variations:** The IMBDC's dynamic responses with respect to output voltage reference variations are given in Fig. 4.9. The output voltage reference decreases from 400 V to 350 V at 0.20 s and then jumps to 450 V after 0.3 s, while the load condition is the same as the case

of Fig. 4.8. After a quick transient, the output voltage is firmly regulated to the latest output voltage reference. In the meantime, when the output voltage reference shifts, the 3-phase inductor currents are evenly balanced.

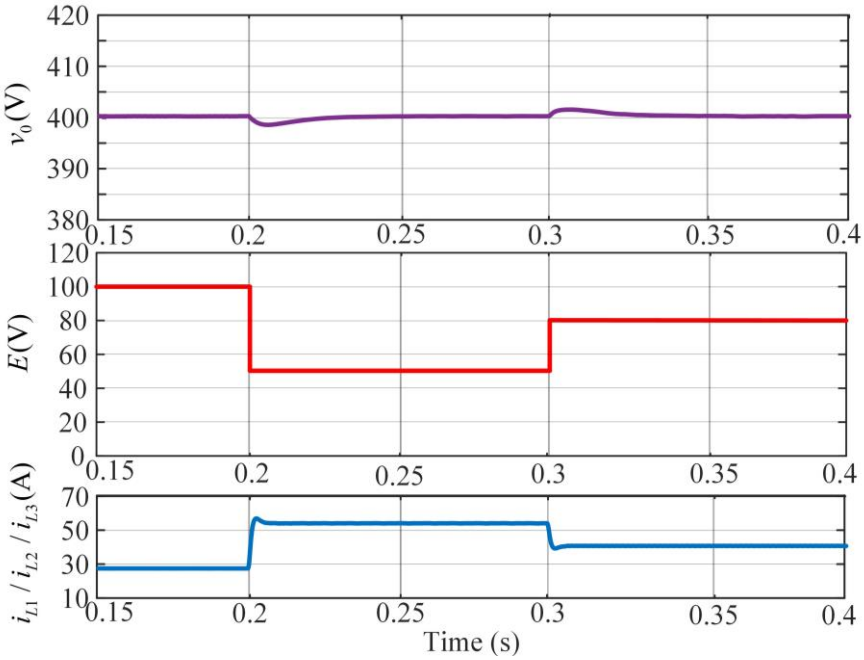

Fig. 4.8 Simulation results of the IMBDC with input voltage variations

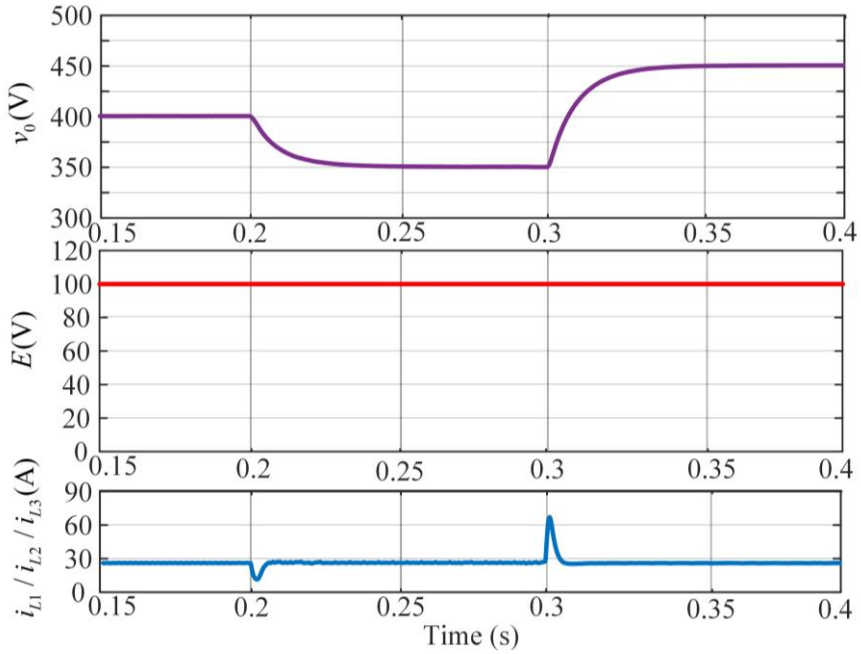

Fig. 4.9 Simulation results of the IMBDC with output voltage reference variations

4.4.3 Comparison with Linear and Nonlinear Controllers

Firstly, a comparative study between the proposed stabilizer and the traditional dual-PI controller is conducted to demonstrate the advantages of the proposed stabilizer in controlling the IMBDC system under large-signal disturbances. Fig. 4.10 depicts the dynamic responses of the IMBDC system controlled by the proposed high-order NDO-based MPC stabilizer. In this case, CPL varies from 5 kW to 50 kW. To ensure a fair comparison, the PI gains are tuned to have a similar dynamic response to that of the proposed scheme when the CPL is increased from 5 kW to 10 kW at 0.3s. In this case, k_{vp}=1 and k_{vi}=100 for the voltage loop and k_{ip}=1.5 and k_{ii}=100 for the current loop. When the CPL is increased from 10 kW to 30 kW at 0.5s, the PI controller can stabilize the DC bus voltage, but it exhibits a longer settling time and larger voltage oscillations during the transition, compared to the MPC-based stabilizer. Furthermore, when the CPL increases from 30 kW to 50 kW at 0.7s, the IMBDC system under the PI controller becomes unstable, while the system controlled by the proposed stabilizer maintains stability, with fast and accurate voltage regulation. These results demonstrate that the proposed stabilizer outperforms the traditional PI controller in terms of stability margin and dynamic response performance.

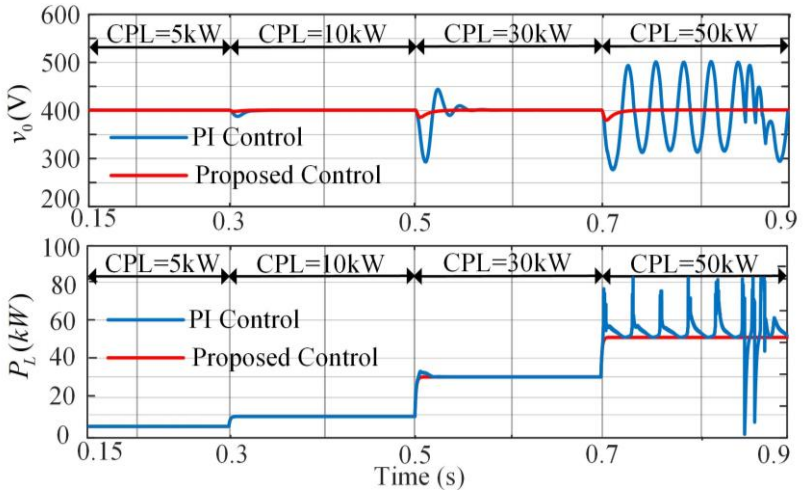

Fig. 4.10 Comparison study on dynamic responses of the IMBDC in the presence of large CPL variations

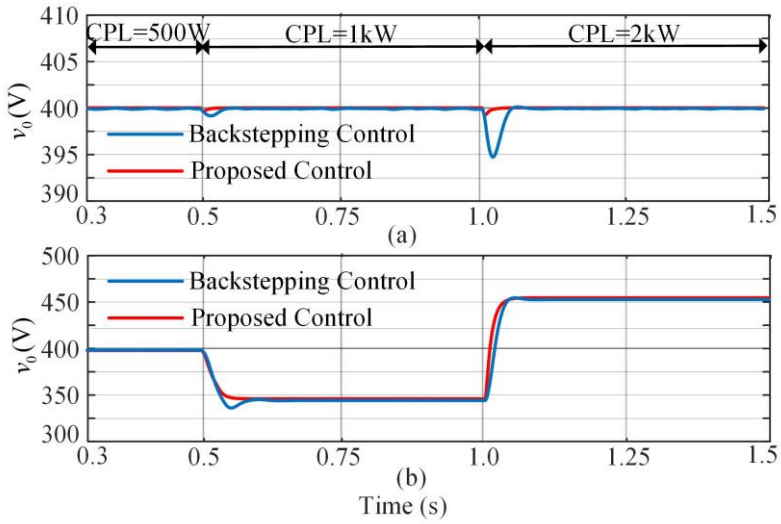

Fig. 4.11 Comparison of dynamic characteristics of the proposed controller and backstepping controller

Secondly, to demonstrate the superiority of the proposed control method over another nonlinear control scheme, another comparison is performed between the adaptive backstepping control and the proposed control scheme. For fairness, the same disturbance observer is used in both the backstepping controller and the proposed controller. The dynamic characteristics are compared under the same system disturbance to assess the performance of the two controllers. Fig. 4.11 (a) illustrates the dynamic behavior of the output voltage for both controllers when the CPL varies. At 0.5s, the CPL changes from 500W to 1kW and jumps to 2kW at 1.0s. Both controllers accurately track the output voltage, but the proposed method exhibits a smaller voltage deviation and shorter settling time compared to the backstepping controller. Specifically, under backstepping control the output voltage experiences a dip of approximately 5 V with a settling time of around 80 ms, whereas the proposed control limits the dip to less than 2 V and achieves a settling time of about 30 ms. Fig. 4.11 (b) presents the dynamic responses of the two controllers when the reference output voltage changes. At 0.5s, the output voltage reference changes from 400V to 350V and then to 450V at 1.0s. Although both controllers can track the changing output voltage reference value, the output voltage dynamic response of the system with the proposed controller is smoother as compared with that of the backstepping controller.

4.4.4 Sensitivity Analysis of the NDO

A simulation test is conducted to assess the sensitivity of the NDO in handling discrepancies between the actual and nominal values of inductance and capacitance in the circuit. In this test, the nominal values of the inductor and capacitor in the circuit are set to 500 mH and 1000 μF, respectively. To simulate potential parameter variations, the actual values of the inductor and capacitor are deviated by ±5%, ±10%, and ±20%. The reference output voltage is maintained at 400 V, with the input voltage fixed at 100 V, while the value of the CPL is adjusted dynamically. At t=0.5s, the CPL value increases from 500 W to 1 kW, then jumps to 2 kW at t=0.6s, and finally reaches 4 kW at t=0.7s. As shown in Fig. 4.12, the dynamic response of the output voltage is observed.

Fig. 4.12 (a) illustrates six scenarios in which the actual value of the capacitor deviates from its nominal value, while the inductor's actual value remains at its nominal value. In contrast, Fig. 4.12 (b) depicts six scenarios where the actual value of the inductor deviates from its nominal value, while the capacitor's actual value remains fixed. Fig. 4.12 demonstrates that the overshoot and settling time of the output voltage are not significantly affected, even when the actual values of the inductor and capacitor deviate substantially from their nominal values. This indicates that the NDO effectively detects disturbances and feeds them back to the MPC controller, maintaining stable voltage regulation under varying inductor and capacitor conditions. These results validate the NDO's effectiveness and highlight the proposed controller's high tolerance to significant parameter variations caused by environmental changes. These results demonstrate that the proposed NDO-based control can effectively mitigate the impact of parameter drift even under variations of 5%, 10%, and 20%. Considering that in harsh shipboard environments, parameter drift rarely exceeds 10%, this simulation study is sufficient to verify the robustness of the proposed method against practical uncertainties.

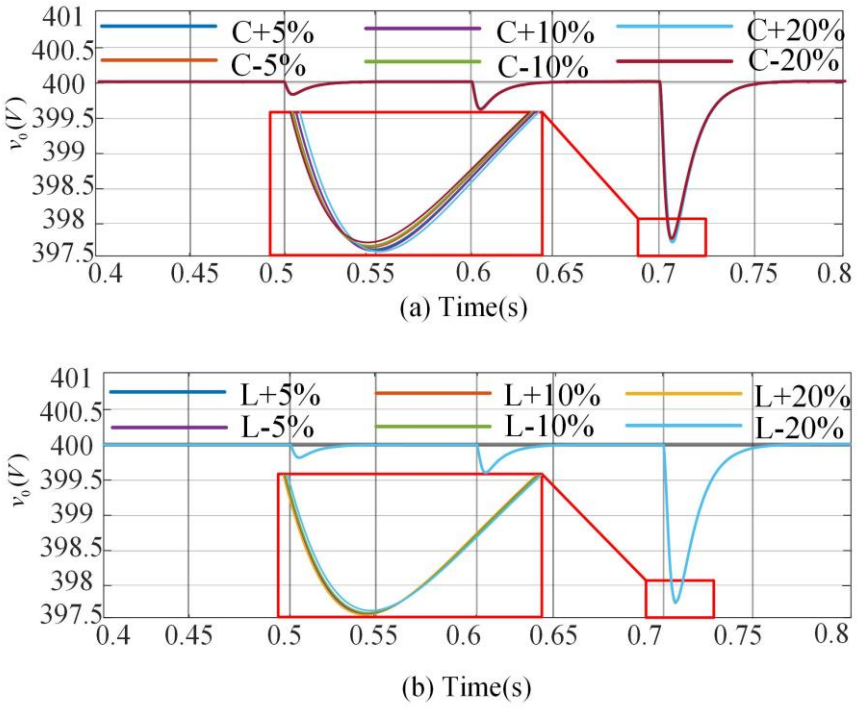

Fig. 4.12 Comparison of output voltage dynamic characteristics of *L* and *C* deviation from nominal values

4.5 Real-time Simulation Results

To verify the efficacy of the proposed stabilizer in practical applications, corresponding real-time simulation results are further obtained for the 3-phase 3-level IMBDC. The system setup is depicted in Fig. 4.13. The circuit parameters utilized in this work are summarized in Table 4-1. In the following figures of experimental results, E represents the input voltage; v_0 indicates the output voltage; i_{L1}, i_{L2}, and i_{L3} are the inductor currents. Similar to the previous simulations, pure CPL is also adopted in every experiment.

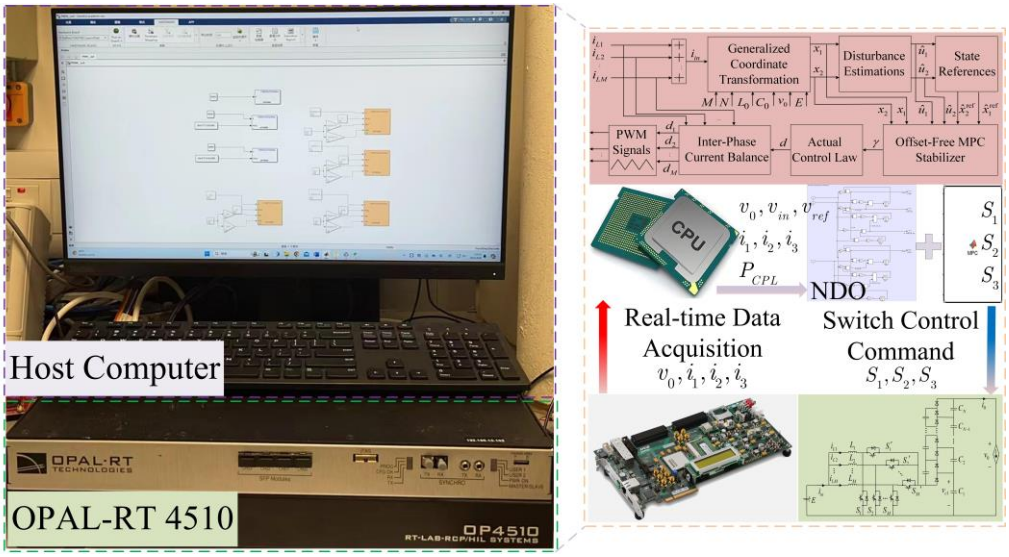

Fig. 4.13 Real-time experimental platform

Table 4-1 Realtime Simulation System Parameters

Symbol	Description	Values
f_s	Switching frequency	20 kHz
E	Input voltage	100 V
v_o^{ref}	Output voltage reference	400 V
L_0	Nominal inductance	0.33 mH
C_0	Nominal capacitance	1410 μF
P_{CPL}	Constant power load	2.5kW-8kW

1) **CPL Changes:** Fig. 4.14 depicts the real-time simulation results of the IMBDC with the CPL variations. In the initial state, CPL is set at 5 kW. At t_1=1.0s, t_2=1.75s, and t_3=2.5s, the CPLs are changed to 8 kW, 6 kW, and 6.1 kW, respectively. After the CPL step changes, the DC bus voltage rapidly reaches its reference 400 V (within 50 ms) with little steady-state inaccuracy. The three-phase inductor currents are successfully balanced in both transient and steady states. Meanwhile, the voltages of the two output capacitors are equalized, and their values are equal to half the output voltage. Hence, the capacitor's voltage stress can be reduced significantly.

2) **Input Voltage Changes:** The real-time simulation results of the IMBDC under changing input voltages are shown in Fig. 4.15. The 2.5-kW CPL is used in this experimental case. At t_1=0.28s, the input voltage is dropped

from 100 V to 50 V. It can be observed that the impact of input voltage disturbance can be eliminated within 50 ms. When the input voltage is further jumped from 50 V to 80 V at t_2=1.17s, the output voltage has a certain overshoot, but it takes a short transient period (within 50 ms) to be stabilized at its reference of 400 V. The inductor currents are evenly shared by the proposed IPCBCs all the time.

3) **Output Voltage Reference Changes:** Fig. 4.16 depicts the real-time simulation results of the IMBDC in the presence of output voltage reference variations. Also, the 5-kW CPL is used in this case. As shown in Fig. 4.16, the output voltage rapidly tracks its updated reference value within 25 ms as the output voltage reference changes from 400 V to 450 V at t_1=0.8s. The steady-state values of the three-phase inductor currents i_{L1}, i_{L2}, and i_{L3} remain constant in pure CPL conditions. Then, the output voltage reference abruptly rises from 450 V to 350 V at t_2=1.5s.

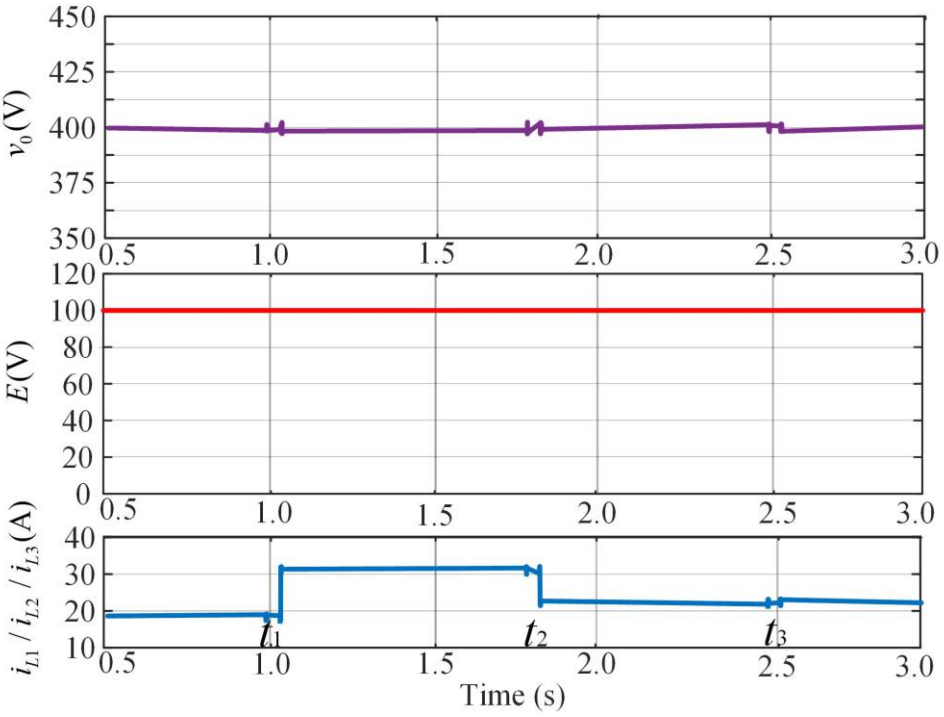

Fig. 4.14 Real-time simulation results of the regulated IMBDC of CPL changes

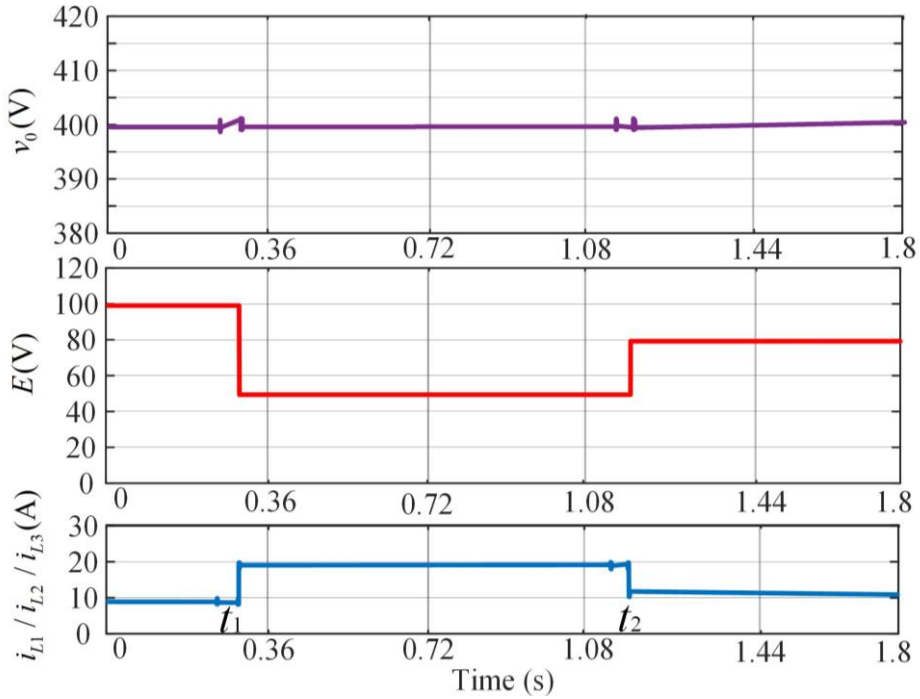

Fig. 4.15 Real-time simulation results of the regulated IMBDC in the presence of input voltage changes

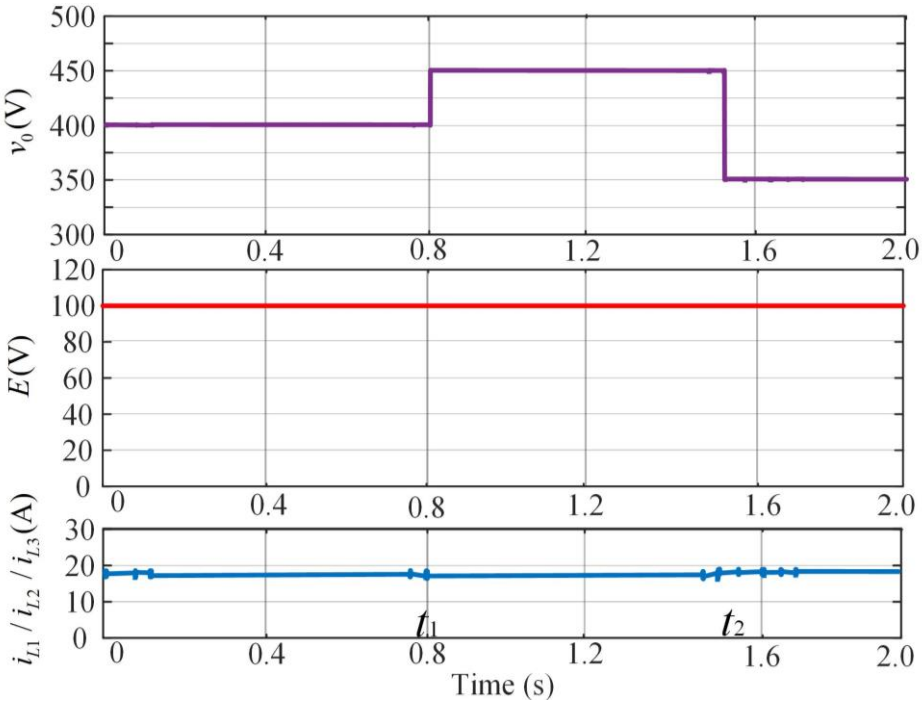

Fig. 4.16 Real-time simulation results of the regulated IMBDC in the presence of output voltage reference changes

From the above real-time simulation results, the proposed stabilizer can enable IMBDC to maintain an excellent stable margin against various large-signal disturbances, including CPL changes, input voltage variations, or output voltage deviations. These results validate the previous theoretical analysis and simulation

results.

4.6 Experimental Verification

To validate the practical performance of the proposed control method, an experimental IMBDC was built. Fig. 4.17 shows the platform, and Table 4-2 shows the parameters of the experiment.

Table 4-2 Experimental Platform Parameters

Symbol	Description	Values
f_s	Switching frequency	20 kHz
f_c	Controller frequency	25kHz
E	Input voltage	30-50 V
v_0^{ref}	Output voltage reference	90-120 V
L_0	Nominal inductance	0.5 mH
C_0	Nominal capacitance	1000 μF
P_{CPL}	Constant power load	30W/50W/80W

In this experiment, a 2-phase 2-level IMBDC is constructed. The RT-Unit, which has a TMS320C28377D as its computation core, is applied as the external controller to control the switches. To show the effectiveness of the proposed MPC stabilizer, three different operation scenarios are tested. In the respective scenario, both the dual-PI control and the proposed control scheme are applied to regulate the system.

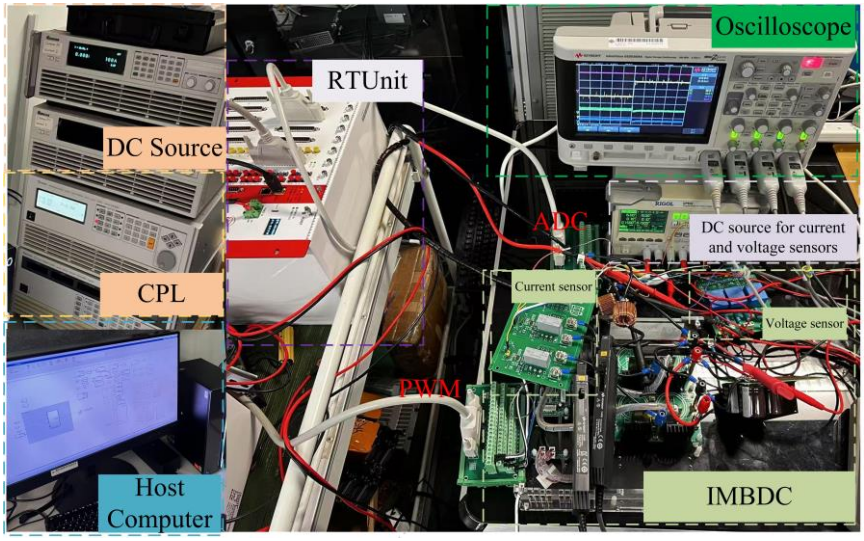

Fig. 4.17 Experimental platform of IMBDC

4.6.1 Scenario I

Fig. 4.18 shows the dynamic responses of the system under CPL variations. Initially, the CPL is set to 50 W, with an output voltage of 90V and an input voltage of 30V. The CPL then changes to 80 W and later to 30 W. Fig. 4.18(a) illustrates the dynamic response of the proposed controller when facing CPL variations. The settling time is only 5 ms. Additionally, the overshoot voltage is 1V, and the overshoot current is 0.2A. In Fig. 4.18(b), despite a larger CPL variation, the proposed controller continues to perform well, with a short settling time of 5 ms, a 1V overshoot in the output voltage, and a 0.2A overshoot inductor current. In contrast, the dual-PI controller shown in Fig. 4.18(c) stabilizes the output voltage, but the settling time increases significantly to 800 ms, the overshoot voltage reaches 12V, and the overshoot current is 0.5A. As the CPL variation becomes even larger, Fig. 4.18(d) demonstrates that the dual-PI controller's settling time further increases to 1000 ms, with the overshoot voltage rising to 20V and the overshoot current reaching 1A. These results clearly demonstrate that, compared to traditional dual-PI controllers, the proposed controller not only significantly reduces settling time but also nearly eliminates output voltage oscillations, demonstrating its better dynamic performance against CPL variations.

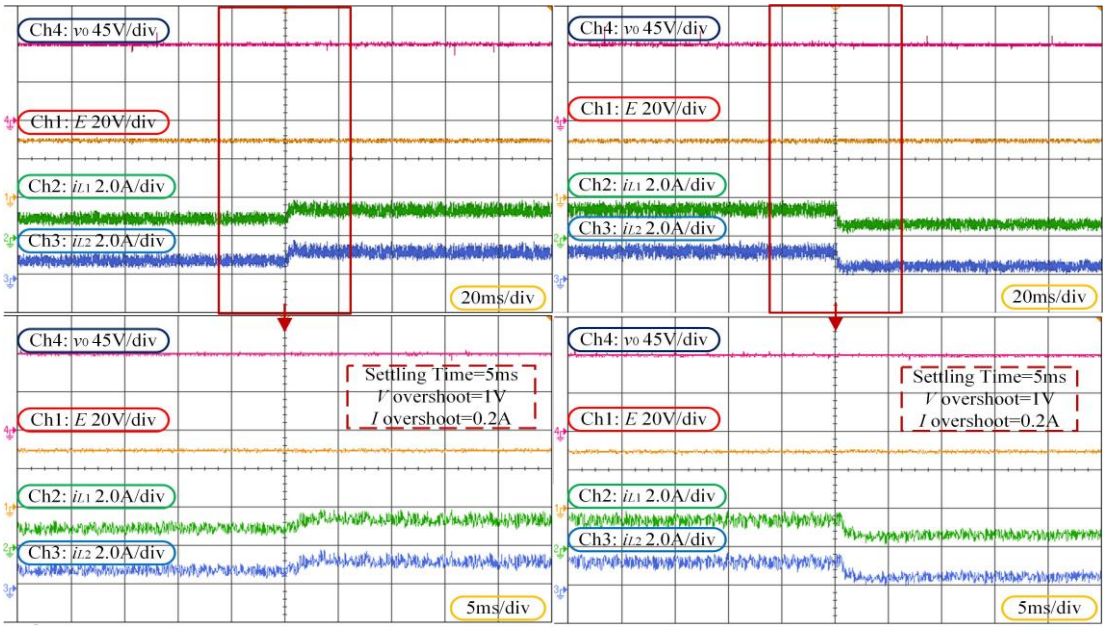

(a) proposed controller (b) proposed controller

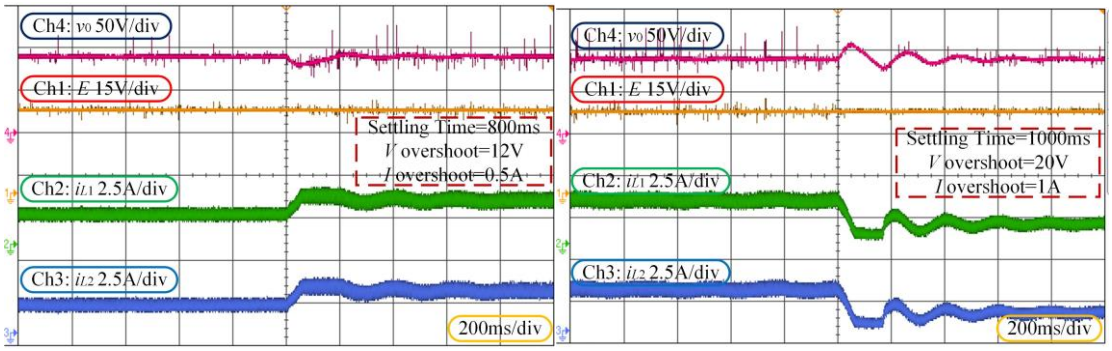

(c) dual-PI controller (d) dual-PI controller

Fig. 4.18 Dynamic response of the system with two controllers under CPL variations

4.6.2 Scenario II

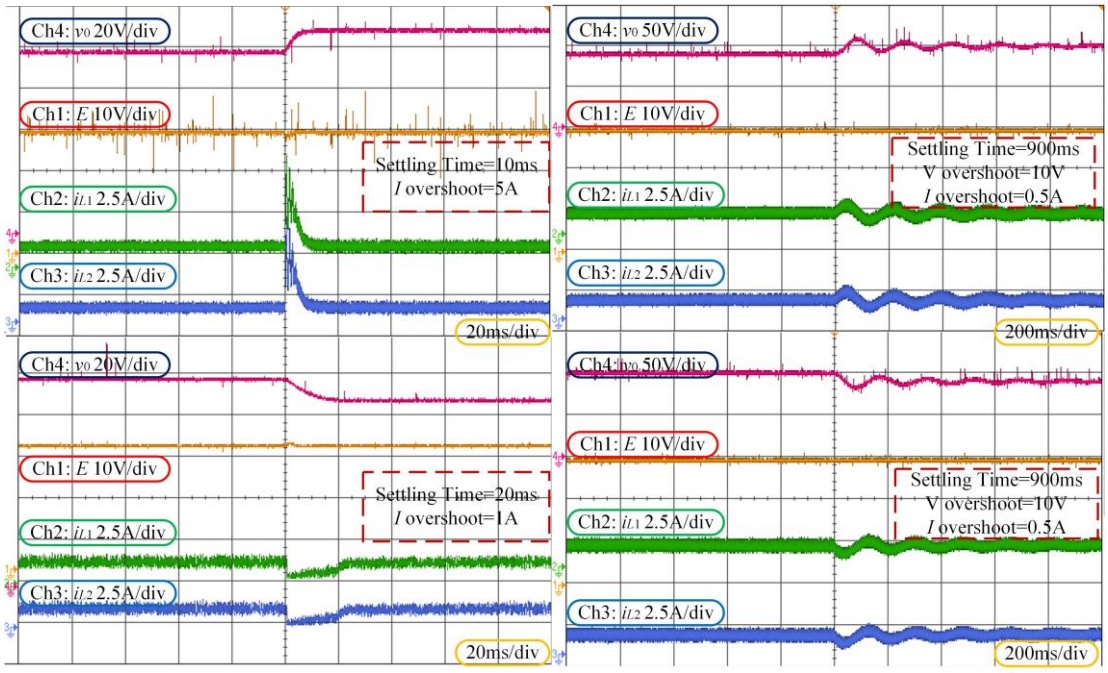

(a) proposed controller (b)dual-PI controller

Fig. 4.19 Dynamic response of the system with two controllers under the reference value of the output voltage variations

Fig. 4.19 shows the dynamic responses of the system when the output voltage reference changes. Initially, the CPL is set to 50 W, with an output voltage of 90V and an input voltage of 30V. The reference then jumps to 100V and later returns to 90V. Fig. 4.19(a) illustrates the dynamic response of the proposed controller when the

output voltage reference changes. The settling time is 10 ms, and there is no overshoot in the output voltage. When the reference voltage is rising, there is an overshoot inductor current of 5A, while when the reference voltage is falling, there is an overshoot inductor current of 1A. In Fig. 4.19(b), the dual-PI controller can also track the output voltage reference, but the settling time is 900 ms, the overshoot voltage reaches 10V, and the overshoot current is 0.5A. While the inductor current overshoot in the proposed controller is relatively large, it remains within an acceptable range. In practical applications, increasing the inductor value can help reduce the overshoot current. This is because the proposed controller quickly charges the capacitor to reach the desired output voltage reference. In summary, compared to the traditional dual-PI controller, the proposed controller not only significantly shortens the settling time but also exhibits almost no voltage overshoot.

4.6.3 Scenario III

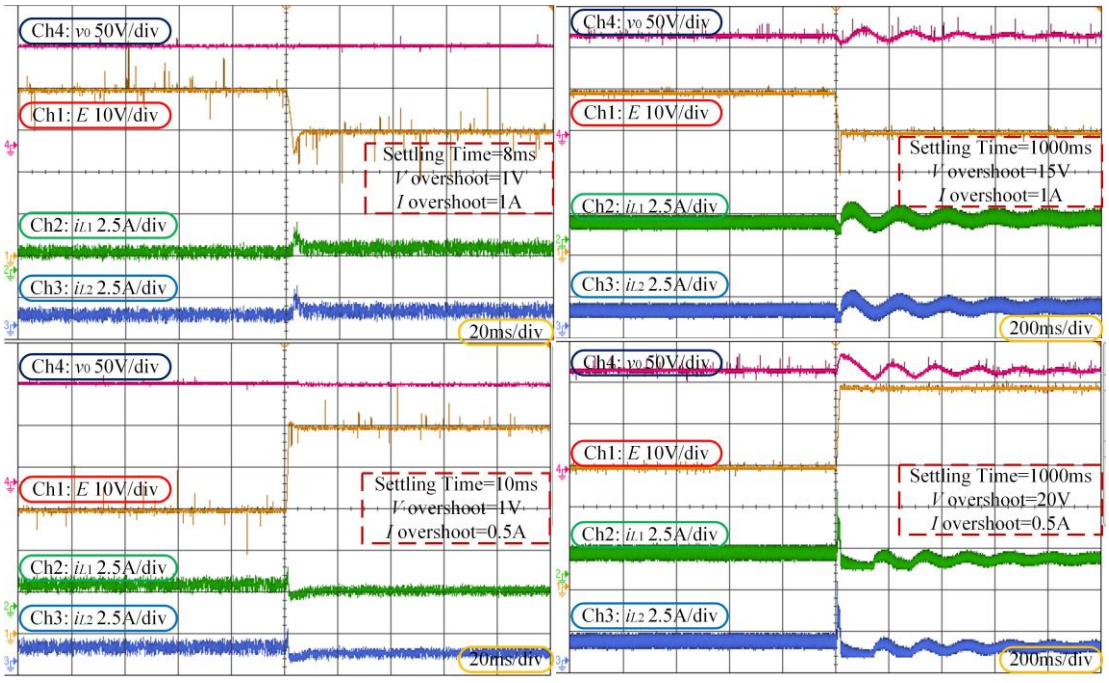

(a) proposed controller (b)dual-PI controller

Fig. 4.20 Dynamic response of the system with two controllers under input voltage variations

Fig. 4.20 shows the dynamic responses of the system under input voltage

variations. Initially, the CPL is set to 50 W, with an output voltage of 120V and an input voltage of 40V. The input voltage then changes to 30V and later jumps to 50V. Fig. 4.20(a) illustrates the dynamic response of the proposed controller to input voltage changes. The settling time is 8 ms and 10 ms. The output voltage overshoot is 1V. The overshoot current is 1A and 0.5A. In Fig. 4.20(b), although the dual-PI controller also stabilizes the system in response to input voltage fluctuations, the settling time is 1000 ms, the overshoot voltage reaches 15V to 20V, and the overshoot current is 1A and 0.5A. The overshoot inductor current is the same for both controllers. Overall, compared to the traditional dual-PI controller, the proposed controller offers a shorter settling time and a smaller output voltage overshoot.

Based on these results, the proposed stabilizer exhibits fast dynamic response, precise voltage tracking, and robust large-signal stability for the regulated IMBDC system. It effectively maintains the stability of the DC bus voltage even under large-signal CPL power variations, aligning with both theoretical analysis and simulation findings. The consistency of the inductor current values further verifies the effectiveness of IPCBC.

4.7 Conclusion

This chapter proposes a compound large-signal stabilization strategy for the IMBDC-interfaced DC SMG with high penetration of CPLs. A generalized reduced-order model of an M-phase N-level IMBDC is developed to simplify the design of the large-signal stabilizer. Using an MPC controller integrated with NDO, the impact of different system operating condition variations is simulated. Additionally, the proposed IPCBC ensures equal sharing of phase currents within the interleaved inductor network. It is certified that the proposed control scheme outperforms the conventional PI and back-stepping control to improve the dynamic performance of the system and stabilize the DC bus voltage of the IMBDC-powered DC SMG under large signal conditions. The NDO effectively observes model uncertainties, making the control scheme insensitive to variations in inductance and capacitance parameters.

It is especially valuable in offshore ship power systems with fluctuating environmental conditions. Hardware experimental results further confirm the proposed method's ability to handle CPL variations, output voltage references, and input voltage changes, ultimately enhancing the reliability and performance of the DC SMG.

Chapter 5 Conclusion and Future Works

5.1 Conclusion of the Thesis

This thesis presents innovative solutions to the challenges associated with controlling and operating DC MGs featuring high penetrations of RESs and CPLs. The key contributions are summarized as follows:

1) **A Review of DC MG architectures and applications:** A comprehensive review and analysis of DC MG architectures and applications domains is presented, covering recent advancements in system topologies, including single-bus, multi-bus, and reconfigurable structures, and their deployments in shipboard environments and data centers. This serves as a contextual foundation for understanding the evolving challenges in modern DC MGs.
2) **Nonlinear Control for PV-Powered DC MGs:** A backstepping controller integrated with an NDO is developed to effectively suppress voltage oscillations induced by CPLs, ensuring stable DC bus voltage and maintaining maximum energy harvesting under varying environmental irradiance and temperature. Simulation results demonstrate an obvious improvement in the dynamic response of bus voltage regulation compared to conventional dual-PI controllers.
3) **Robust Stabilization for Marine DC SMGs:** A compound stabilizer combining MPC and high-order NDOs is proposed for IMBDCs in SMGs. The strategy exhibits strong resilience against environmental disturbances, achieving rapid voltage recovery (settling time <10 ms) and effective inter-phase current balancing under large CPL fluctuations. Experimental validation shows a 50% reduction in settling time and minimal voltage overshoot compared to traditional linear controllers.

5.2 Future Research Directions

Building on the findings and limitations of this thesis, several promising research avenues can be explored to further advance DC MG technologies and renewable energy integration:

1) **Hybrid Energy System Coordination**

   Future research can investigate dynamic energy routing strategies in DC MGs with high penetration of multiple renewable sources, such as photovoltaic, wind, hydrogen, and supercapacitors. Event-triggered distributed control methods could be developed to resolve power-sharing conflicts and maintain transient stability across different time scales, ensuring optimal performance in highly dynamic environments.

2) **AI-Driven Predictive Control**

   Combining reinforcement learning (RL) techniques with model predictive control (MPC) provides a promising approach for dynamically optimizing prediction horizons and cost function weights. This integration will be able to adapt to rapid, CPL changes and intermittent renewable energy in real time, thereby enhancing the flexibility and intelligence of microgrid operation. At the same time, developing digital twin models of IMBDCs based on physical information neural networks can significantly improve fault prediction capabilities. These models will help detect parameter drift phenomena, such as inductor aging, at an early stage, enabling proactive control adjustments and extending system reliability and service life.

3) **Edge computing-energy collaborative scheduling**

   Optimizing workload distribution in data centers through spatiotemporal carbon intensity prediction is a key step towards green operations. Combining computing tasks with renewable energy generation peaks (such as solar noon and windy nights) can significantly improve energy efficiency and reduce the carbon footprint of large computing facilities. At the same time, non-real-time computing tasks can be orderly scheduled to be

calculated during renewable energy-rich periods to improve the utilization rate of renewable energy in data centers.

References

[1] I. R. E. A. (IRENA), "Renewable Capacity Highlights 2025," 2025. [Online]. Available: https://www.irena.org/-/media/Files/IRENA/Agency/Publication/2025/Mar/IRENA_DAT_RE_Capacity_Highlights_2025.pdf

[2] I. R. E. A. (IRENA), "Renewable capacity statistics 2025," 2025. [Online]. Available: https://www.irena.org/Publications/2025/Mar/Renewable-capacity-statistics-2025

[3] I. E. A. (IEA), "Renewables 2024," 2025. [Online]. Available: https://iea.blob.core.windows.net/assets/17033b62-07a5-4144-8dd0-651cdb6caa24/Renewables2024.pdf

[4] T. Dragičević, X. Lu, J. C. Vasquez, and J. M. Guerrero, "DC microgrids—Part I: A review of control strategies and stabilization techniques," *IEEE Transactions on power electronics*, vol. 31, no. 7, pp. 4876-4891, 2015.

[5] H. Lotfi and A. Khodaei, "AC versus DC microgrid planning," *IEEE transactions on smart grid*, vol. 8, no. 1, pp. 296-304, 2015.

[6] H. Kakigano, Y. Miura, and T. Ise, "Distribution voltage control for DC microgrids using fuzzy control and gain-scheduling technique," *IEEE transactions on power electronics*, vol. 28, no. 5, pp. 2246-2258, 2012.

[7] G. Van den Broeck, J. Stuyts, and J. Driesen, "A critical review of power quality standards and definitions applied to DC microgrids," *Applied energy*, vol. 229, pp. 281-288, 2018.

[8] T. Dragicevic, J. C. Vasquez, J. M. Guerrero, and D. Skrlec, "Advanced LVDC electrical power architectures and microgrids: A step toward a new generation of power distribution networks," *IEEE Electrification Magazine*, vol. 2, no. 1, pp. 54-65, 2014.

[9] T. Dragičević, X. Lu, J. C. Vasquez, and J. M. Guerrero, "DC microgrids—Part II: A review of power architectures, applications, and standardization issues," *IEEE transactions on power electronics*, vol. 31, no. 5, pp. 3528-3549, 2015.

[10] M. S. Alam *et al.*, "Renewable energy integration with DC microgrids: Challenges and opportunities," *Electric Power Systems Research*, vol. 234, p. 110548, 2024.

[11] T. Tanaka, K. Hirose, D. Marquet, B. Sonnenberg, and M. Szpek, "Analysis of wiring design for 380-VDC power distribution system at telecommunication sites," in *Intelec 2012*, 2012: IEEE, pp. 1-5.

[12] A. T. Elsayed, A. A. Mohamed, and O. A. Mohammed, "DC microgrids and distribution systems: An overview," *Electric power systems research*, vol. 119, pp. 407-417, 2015.

[13] J. J. Justo, F. Mwasilu, J. Lee, and J.-W. Jung, "AC-microgrids versus DC-microgrids with distributed energy resources: A review," *Renewable and sustainable energy reviews*, vol. 24, pp. 387-405, 2013.

[14] X. Lu, J. M. Guerrero, K. Sun, and J. C. Vasquez, "An improved droop control method for DC microgrids based on low bandwidth communication with DC bus voltage restoration and enhanced current sharing accuracy," *IEEE transactions on power electronics*, vol. 29, no. 4, pp. 1800-1812, 2013.

[15] J. Liu, W. Zhang, and G. Rizzoni, "Robust stability analysis of DC microgrids with constant power loads," *IEEE Transactions on Power Systems*, vol. 33, no. 1, pp. 851-860, 2017.

[16] S. Wen *et al.*, "Coordinated optimal energy management and voyage scheduling for all-electric ships based on predicted shore-side electricity price," *IEEE Transactions on Industry Applications*, vol. 57, no. 1, pp. 139-148, 2020.
[17] X. Zhang, Q.-C. Zhong, V. Kadirkamanathan, J. He, and J. Huang, "Source-side series-virtual-impedance control to improve the cascaded system stability and the dynamic performance of its source converter," *IEEE Transactions on Power Electronics*, vol. 34, no. 6, pp. 5854-5866, 2018.
[18] H. Wang, X. Ge, and Y.-C. Liu, "An active damping stabilization scheme for the suppression of the DC-link oscillation in metro traction drive system," *IEEE Transactions on Industry Applications*, vol. 54, no. 5, pp. 5113-5123, 2018.
[19] M. Wu and D. D.-C. Lu, "A novel stabilization method of LC input filter with constant power loads without load performance compromise in DC microgrids," *IEEE Transactions on industrial electronics*, vol. 62, no. 7, pp. 4552-4562, 2014.
[20] Y. Zhao, W. Qiao, and D. Ha, "A sliding-mode duty-ratio controller for DC/DC buck converters with constant power loads," *IEEE Transactions on industry Applications*, vol. 50, no. 2, pp. 1448-1458, 2013.
[21] X. Li, X. Zhang, W. Jiang, J. Wang, P. Wang, and X. Wu, "A novel assorted nonlinear stabilizer for DC–DC multilevel boost converter with constant power load in DC microgrid," *IEEE Transactions on Power Electronics*, vol. 35, no. 10, pp. 11181-11192, 2020.
[22] N. Vafamand, M. H. Khooban, T. Dragičević, F. Blaabjerg, and J. Boudjadar, "Robust non-fragile fuzzy control of uncertain DC microgrids feeding constant power loads," *IEEE Transactions on Power Electronics*, vol. 34, no. 11, pp. 11300-11308, 2019.
[23] R. H. Lasseter, "Microgrids," in *2002 IEEE power engineering society winter meeting. Conference proceedings (Cat. No. 02CH37309)*, 2002, vol. 1: IEEE, pp. 305-308.
[24] E. A. A. Coelho, P. C. Cortizo, and P. F. D. Garcia, "Small-signal stability for parallel-connected inverters in stand-alone AC supply systems," *IEEE Transactions on Industry Applications*, vol. 38, no. 2, pp. 533-542, 2002.
[25] S. Wang, Z. Liu, J. Liu, D. Boroyevich, and R. Burgos, "Small-signal modeling and stability prediction of parallel droop-controlled inverters based on terminal characteristics of individual inverters," *IEEE Transactions on Power Electronics*, vol. 35, no. 1, pp. 1045-1063, 2019.
[26] J. M. Guerrero, L. G. De Vicuna, J. Matas, M. Castilla, and J. Miret, "A wireless controller to enhance dynamic performance of parallel inverters in distributed generation systems," *IEEE Transactions on power electronics*, vol. 19, no. 5, pp. 1205-1213, 2004.
[27] M. A. Abusara, J. M. Guerrero, and S. M. Sharkh, "Line-interactive UPS for microgrids," *IEEE Transactions on Industrial Electronics*, vol. 61, no. 3, pp. 1292-1300, 2013.
[28] Q.-C. Zhong, "Robust droop controller for accurate proportional load sharing among inverters operated in parallel," *IEEE Transactions on industrial Electronics*, vol. 60, no. 4, pp. 1281-1290, 2011.
[29] P. Tian, X. Xiao, K. Wang, and R. Ding, "A hierarchical energy management system based on hierarchical optimization for microgrid community economic operation," *IEEE Transactions on Smart Grid*, vol. 7, no. 5, pp. 2230-2241, 2015.
[30] R. Bustos, L. G. Marín, A. Navas-Fonseca, L. Reyes-Chamorro, and D. Sáez, "Hierarchical energy management system for multi-microgrid coordination with demand-side management," *Applied Energy*, vol. 342, p. 121145, 2023.

[31] A. Pratt, P. Kumar, and T. V. Aldridge, "Evaluation of 400V DC distribution in telco and data centers to improve energy efficiency," in *INTELEC 07-29th International Telecommunications Energy Conference*, 2007: IEEE, pp. 32-39.
[32] Y. Ito, Y. Zhongqing, and H. Akagi, "DC microgrid based distribution power generation system," in *The 4th International Power Electronics and Motion Control Conference, 2004. IPEMC 2004.*, 2004, vol. 3: IEEE, pp. 1740-1745.
[33] T. R. Oliveira, W. W. A. G. Silva, and P. F. Donoso-Garcia, "Distributed secondary level control for energy storage management in DC microgrids," *IEEE Transactions on Smart Grid*, vol. 8, no. 6, pp. 2597-2607, 2016.
[34] K. Bharath, M. M. Krishnan, and P. Kanakasabapathy, "A review on DC microgrid control techniques, applications and trends," *Int. J. Renew. Energy Res*, vol. 9, no. 3, pp. 1328-1338, 2019.
[35] R. Kaur, V. Krishnasamy, and N. K. Kandasamy, "Optimal sizing of wind–PV-based DC microgrid for telecom power supply in remote areas," *IET Renewable Power Generation*, vol. 12, no. 7, pp. 859-866, 2018.
[36] D. Kumar, F. Zare, and A. Ghosh, "DC microgrid technology: system architectures, AC grid interfaces, grounding schemes, power quality, communication networks, applications, and standardizations aspects," *Ieee Access*, vol. 5, pp. 12230-12256, 2017.
[37] H. Kakigano, Y. Miura, T. Ise, and R. Uchida, "DC micro-grid for super high quality distribution—System configuration and control of distributed generations and energy storage devices," in *2006 37th IEEE Power Electronics Specialists Conference*, 2006: IEEE, pp. 1-7.
[38] C. Capasso and O. Veneri, "Experimental study of a DC charging station for full electric and plug in hybrid vehicles," *Applied energy*, vol. 152, pp. 131-142, 2015.
[39] D. Fregosi *et al.*, "A comparative study of DC and AC microgrids in commercial buildings across different climates and operating profiles," in *2015 IEEE First International Conference on DC Microgrids (ICDCM)*, 2015: IEEE, pp. 159-164.
[40] G. AlLee and W. Tschudi, "Edison redux: 380 Vdc brings reliability and efficiency to sustainable data centers," *IEEE Power and Energy Magazine*, vol. 10, no. 6, pp. 50-59, 2012.
[41] Z. Jin, G. Sulligoi, R. Cuzner, L. Meng, J. C. Vasquez, and J. M. Guerrero, "Next-generation shipboard dc power system: Introduction smart grid and dc microgrid technologies into maritime electrical netowrks," *IEEE Electrification Magazine*, vol. 4, no. 2, pp. 45-57, 2016.
[42] L. Xu *et al.*, "A review of DC shipboard microgrids—Part I: Power architectures, energy storage, and power converters," *IEEE Transactions on Power Electronics*, vol. 37, no. 5, pp. 5155-5172, 2021.
[43] N. Rashidirad, M. Hamzeh, K. Sheshyekani, and E. Afjei, "A simplified equivalent model for the analysis of low-frequency stability of multi-bus DC microgrids," *IEEE Transactions on Smart Grid*, vol. 9, no. 6, pp. 6170-6182, 2017.
[44] K. Nandini, N. Jayalakshmi, and V. K. Jadoun, "An overview of DC Microgrid with DC distribution system for DC loads," *Materials Today: Proceedings*, vol. 51, pp. 635-639, 2022.
[45] S.-K. Kim, J.-H. Jeon, C.-H. Cho, J.-B. Ahn, and S.-H. Kwon, "Dynamic modeling and control of a grid-connected hybrid generation system with versatile power transfer," *IEEE transactions on industrial electronics*, vol. 55, no. 4, pp. 1677-1688, 2008.
[46] M. Salato, A. Zolj, D. J. Becker, and B. Sonnenberg, "Power system architectures for 380V DC distribution in telecom datacenters," in *Intelec 2012*, 2012: IEEE, pp. 1-7.
[47] P. Singh and J. Lather, "Dynamic current sharing, voltage and SOC regulation for HESS

based DC microgrid using CPISMC technique," *Journal of Energy Storage*, vol. 30, p. 101509, 2020.
[48] Y. Mi *et al.*, "The coordinated control strategy for isolated DC microgrid based on adaptive storage adjustment without communication," *Applied Energy*, vol. 252, p. 113465, 2019.
[49] Y. Zeng, Q. Zhang, Y. Liu, X. Zhuang, and H. Guo, "Hierarchical cooperative control strategy for battery storage system in islanded DC microgrid," *IEEE Transactions on Power Systems*, vol. 37, no. 5, pp. 4028-4039, 2021.
[50] V. F. Pires, A. Cordeiro, C. Roncero-Clemente, S. Rivera, and T. Dragičević, "DC–DC converters for bipolar microgrid voltage balancing: A comprehensive review of architectures and topologies," *IEEE Journal of Emerging and Selected Topics in Power Electronics*, vol. 11, no. 1, pp. 981-998, 2022.
[51] M. Leng, G. Zhou, H. Li, G. Xu, F. Blaabjerg, and T. Dragičević, "Impedance-based stability evaluation for multibus DC microgrid without constraints on subsystems," *IEEE Transactions on Power Electronics*, vol. 37, no. 1, pp. 932-943, 2021.
[52] H. Faraji, S. M. Nosratabadi, and R. Hemmati, "AC unbalanced and DC load management in multi-bus residential microgrid integrated with hybrid capacity resources," *Energy*, vol. 252, p. 124070, 2022.
[53] R. S. Balog and P. T. Krein, "Bus selection in multibus DC microgrids," *IEEE Transactions on Power Electronics*, vol. 26, no. 3, pp. 860-867, 2010.
[54] J.-D. Park, J. Candelaria, L. Ma, and K. Dunn, "DC ring-bus microgrid fault protection and identification of fault location," *IEEE transactions on Power delivery*, vol. 28, no. 4, pp. 2574-2584, 2013.
[55] R. T. Pinto, P. Bauer, S. F. Rodrigues, E. J. Wiggelinkhuizen, J. Pierik, and B. Ferreira, "A novel distributed direct-voltage control strategy for grid integration of offshore wind energy systems through MTDC network," *IEEE Transactions on Industrial Electronics*, vol. 60, no. 6, pp. 2429-2441, 2012.
[56] W. Lu and B.-T. Ooi, "Optimal acquisition and aggregation of offshore wind power by multiterminal voltage-source HVDC," *IEEE Transactions on power delivery*, vol. 18, no. 1, pp. 201-206, 2003.
[57] R. M. Cuzner and G. Venkataramanan, "The status of DC micro-grid protection," in *2008 IEEE Industry Applications Society Annual Meeting*, 2008: IEEE, pp. 1-8.
[58] E. Tironi, M. Corti, and G. Ubezio, "Zonal electrical distribution systems in large ships: Topology and control," in *2015 AEIT International Annual Conference (AEIT)*, 2015: IEEE, pp. 1-6.
[59] Y. Xuan, X. Yang, W. Chen, T. Liu, and X. Hao, "A novel three-level CLLC resonant DC–DC converter for bidirectional EV charger in DC microgrids," *IEEE Transactions on Industrial Electronics*, vol. 68, no. 3, pp. 2334-2344, 2020.
[60] F. Perez, A. Iovine, G. Damm, L. Galai-Dol, and P. F. Ribeiro, "Stability analysis of a DC microgrid for a smart railway station integrating renewable sources," *IEEE Transactions on Control Systems Technology*, vol. 28, no. 5, pp. 1802-1816, 2019.
[61] L. Tarisciotti, A. Costabeber, L. Chen, A. Walker, and M. Galea, "Current-fed isolated DC/DC converter for future aerospace microgrids," *IEEE Transactions on Industry Applications*, vol. 55, no. 3, pp. 2823-2832, 2018.
[62] H. Yu, P. Lin, Y. Zeng, Q. Zhang, and Y. Wu, "Distributed Predefined-Time Droop-Free

Unified Control Scheme for Parallel Energy Storage Units in All-Electric Aircraft Onboard DC Microgrid," *IEEE Transactions on Power Electronics*, 2025.
[63] M. Mosayebi, S. M. Sadeghzadeh, M. Gheisarnejad, and M. H. Khooban, "Intelligent and fast model-free sliding mode control for shipboard DC microgrids," *IEEE Transactions on Transportation Electrification*, vol. 7, no. 3, pp. 1662-1671, 2020.
[64] G. Sulligoi, D. Bosich, A. Vicenzutti, and Y. Khersonsky, "Design of zonal electrical distribution systems for ships and oil platforms: Control systems and protections," *IEEE Transactions on Industry Applications*, vol. 56, no. 5, pp. 5656-5669, 2020.
[65] N. Blenkey. "Tests confirm fuel savings with ABB Onboard DC Grid." https://www.marinelog.com/news/tests-confirm-fuel-savings-with-abb-onboard-dc-grid/ (accessed.
[66] O. D. Grid, "Onboard DC Grid The step forward in Power Generation and Propulsion."
[67] Y. Liu, X. Wei, J. Xiao, Z. Liu, Y. Xu, and Y. Tian, "Energy consumption and emission mitigation prediction based on data center traffic and PUE for global data centers," *Global Energy Interconnection*, vol. 3, no. 3, pp. 272-282, 2020.
[68] S. S. IEA (2024) Thomas Spencer. "What the data centre and AI boom could mean for the energy sector." https://www.iea.org/commentaries/what-the-data-centre-and-ai-boom-could-mean-for-the-energy-sector (accessed.
[69] T. L. Vasques, P. Moura, and A. de Almeida, "A review on energy efficiency and demand response with focus on small and medium data centers," *Energy Efficiency*, vol. 12, pp. 1399-1428, 2019.
[70] V. Avelar, D. Azevedo, A. French, and E. N. Power, "PUE: a comprehensive examination of the metric," *White paper*, vol. 49, 2012.
[71] D. Salomonsson, L. Soder, and A. Sannino, "An adaptive control system for a DC microgrid for data centers," in *2007 IEEE Industry Applications Annual Meeting*, 2007: IEEE, pp. 2414-2421.
[72] P. T. Krein, "A discussion of data center power challenges across the system," in *2010 International Conference on Energy Aware Computing*, 2010: IEEE, pp. 1-3.
[73] "Alibaba Qiandao Lake Data Center." https://www.odcc.org.cn/auth/v-11019.html (accessed.
[74] Z. Liu, J. Li, M. Su, X. Liu, and L. Yuan, "Stability analysis of equilibrium of DC microgrid under distributed control," *IEEE Transactions on Power Systems*, vol. 39, no. 1, pp. 1058-1067, 2023.
[75] A. Emadi, A. Khaligh, C. H. Rivetta, and G. A. Williamson, "Constant power loads and negative impedance instability in automotive systems: definition, modeling, stability, and control of power electronic converters and motor drives," *IEEE Transactions on vehicular technology*, vol. 55, no. 4, pp. 1112-1125, 2006.
[76] S. Singh, A. R. Gautam, and D. Fulwani, "Constant power loads and their effects in DC distributed power systems: A review," *Renewable and Sustainable Energy Reviews*, vol. 72, pp. 407-421, 2017.
[77] N. Hou, L. Ding, P. Gunawardena, T. Wang, Y. Zhang, and Y. W. Li, "A partial power processing structure embedding renewable energy source and energy storage element for islanded DC microgrid," *IEEE Transactions on Power Electronics*, vol. 38, no. 3, pp. 4027-4039, 2022.
[78] X. Li *et al.*, "A robust autonomous sliding-mode control of renewable DC microgrids for decentralized power sharing considering large-signal stability," *Applied Energy*, vol. 339, p. 121019, 2023.

[79] M. Mosayebi, M. Gheisarnejad, and M. H. Khooban, "An intelligent sliding mode control for stabilization of parallel converters feeding CPLs in DC-microgrid," *IET Power Electronics,* vol. 15, no. 14, pp. 1596-1606, 2022.
[80] Z. Wang and J. Hu, "Composite sliding mode control for converters with unknown constant power load," *IEEE Transactions on Industry Applications,* vol. 60, no. 3, pp. 4098-4108, 2024.
[81] M. A. Hassan, E.-p. Li, X. Li, T. Li, C. Duan, and S. Chi, "Adaptive passivity-based control of DC–DC buck power converter with constant power load in DC microgrid systems," *IEEE Journal of Emerging and Selected Topics in Power Electronics,* vol. 7, no. 3, pp. 2029-2040, 2018.
[82] M. A. Hassan, C.-L. Su, J. Pou, D. Almakhles, T.-S. Zhan, and K.-Y. Lo, "Robust passivity-based control for interleaved bidirectional DC–DC power converter with constant power loads in DC shipboard microgrid," *IEEE Transactions on Transportation Electrification,* vol. 10, no. 2, pp. 3590-3602, 2023.
[83] Z. Zhang, P. Wang, J. Zhou, W. Wang, and D. Xu, "A Novel Passivity Model Predictive Control for Predefined-Time Feedforward Compensation in DC Microgrids Feeding Constant Power Loads," *IEEE Transactions on Power Electronics,* 2024.
[84] E. Kowsari, J. Zarei, R. Razavi-Far, M. Saif, T. Dragičević, and M.-H. Khooban, "A novel stochastic predictive stabilizer for DC microgrids feeding CPLs," *IEEE Journal of Emerging and Selected Topics in Power Electronics,* vol. 9, no. 2, pp. 1222-1232, 2020.
[85] Z. Karami, Q. Shafiee, Y. Khayat, M. Yaribeygi, T. Dragičević, and H. Bevrani, "Decentralized model predictive control of DC microgrids with constant power load," *IEEE Journal of Emerging and Selected Topics in Power Electronics,* vol. 9, no. 1, pp. 451-460, 2019.
[86] M. Zhang, Y. Li, F. Liu, L. Luo, Y. Cao, and M. Shahidehpour, "Voltage stability analysis and sliding-mode control method for rectifier in DC systems with constant power loads," *IEEE Journal of Emerging and Selected Topics in Power Electronics,* vol. 5, no. 4, pp. 1621-1630, 2017.
[87] N. Sarrafan, J. Zarei, R. Razavi-Far, M. Saif, and M.-H. Khooban, "A novel on-board DC/DC converter controller feeding uncertain constant power loads," *IEEE Journal of Emerging and Selected Topics in Power Electronics,* vol. 9, no. 2, pp. 1233-1240, 2020.
[88] Y. Gu, W. Li, and X. He, "Passivity-based control of DC microgrid for self-disciplined stabilization," *IEEE Transactions on Power Systems,* vol. 30, no. 5, pp. 2623-2632, 2014.
[89] H. Wu, V. Pickert, D. Giaouris, and B. Ji, "Nonlinear analysis and control of interleaved boost converter using real-time cycle to cycle variable slope compensation," *IEEE Transactions on Power Electronics,* vol. 32, no. 9, pp. 7256-7270, 2016.
[90] J. C. Rosas-Caro, J. M. Ramirez, F. Z. Peng, and A. Valderrabano, "A DC–DC multilevel boost converter," *IET Power Electronics,* vol. 3, no. 1, pp. 129-137, 2010.
[91] X. Su, M. Wang, Y. Wang, Z. Xu, and T. Wang, "An Adaptive Compensated Virtual Impedance Method for Oscillation Suppression in DC Distribution Power Systems," *IEEE Transactions on Industrial Electronics,* vol. 72, no. 5, p. 10, 2024.
[92] X. Lu, K. Sun, J. M. Guerrero, J. C. Vasquez, L. Huang, and J. Wang, "Stability enhancement based on virtual impedance for DC microgrids with constant power loads," *IEEE Transactions on Smart Grid,* vol. 6, no. 6, pp. 2770-2783, 2015.
[93] L. Herrera, W. Zhang, and J. Wang, "Stability analysis and controller design of DC microgrids with constant power loads," *IEEE Transactions on smart grid,* vol. 8, no. 2, pp. 881-888, 2015.
[94] M. Cespedes, L. Xing, and J. Sun, "Constant-power load system stabilization by passive

damping," *IEEE Transactions on Power Electronics*, vol. 26, no. 7, pp. 1832-1836, 2011.
[95] O. Lorzadeh, I. Lorzadeh, M. N. Soltani, and A. Hajizadeh, "Source-side virtual RC damper-based stabilization technique for cascaded systems in DC microgrids," *IEEE Transactions on Energy Conversion*, vol. 36, no. 3, pp. 1883-1895, 2021.
[96] H. Lin, H. S.-H. Chung, R. Shen, and Y. Xiang, "Enhancing stability of dc cascaded systems with CPLs using MPC combined with NI and accounting for parameter uncertainties," *IEEE Transactions on Power Electronics*, 2024.
[97] W. Jiang, X. Zhang, F. Guo, J. Chen, P. Wang, and L. H. Koh, "Large-signal stability of interleave boost converter system with constant power load using sliding-mode control," *IEEE Transactions on Industrial Electronics*, vol. 67, no. 11, pp. 9450-9459, 2019.
[98] Q. Guo, M. J. Carrizosa, A. Iovine, and A. Arzandé, "Dynamic feedback linearization and singular perturbation for a stabilizing controller for dc/dc boost converters: theory and experimental validation," *IEEE Transactions on Industrial Electronics*, 2023.
[99] P. Thounthong *et al.*, "Robust hamiltonian energy control based on lyapunov function for four-phase parallel fuel cell boost converter for DC microgrid applications," *IEEE Transactions on Sustainable Energy*, vol. 12, no. 3, pp. 1500-1511, 2021.
[100] R. Errouissi, H. Shareef, A. Viswambharan, and A. Wahyudie, "Disturbance-observer-based feedback linearization control for stabilization and accurate voltage tracking of a DC–DC boost converter," *IEEE Transactions on Industry Applications*, vol. 58, no. 5, pp. 6687-6700, 2022.
[101] Z. Liu *et al.*, "Existence and stability of equilibrium of DC Micro-grid under master-slave control," *IEEE Transactions on Power Systems*, vol. 37, no. 1, pp. 212-223, 2021.
[102] D. Ginoya, P. Shendge, and S. Phadke, "Sliding mode control for mismatched uncertain systems using an extended disturbance observer," *IEEE Transactions on Industrial Electronics*, vol. 61, no. 4, pp. 1983-1992, 2013.
[103] J. Jiang *et al.*, "A conservatism-free large signal stability analysis method for DC microgrid based on mixed potential theory," *IEEE Transactions on Power Electronics*, vol. 34, no. 11, pp. 11342-11351, 2019.
[104] A. Latorre, T. B. Soeiro, R. Geertsma, A. Coraddu, and H. Polinder, "Shipboard DC systems—A critical overview: Challenges in primary distribution, power-electronics-based protection, and power scalability," *IEEE Open Journal of the Industrial Electronics Society*, vol. 4, pp. 259-286, 2023.
[105] M. Kwon and S. Choi, "Control scheme for autonomous and smooth mode switching of bidirectional DC–DC converters in a DC microgrid," *IEEE Transactions on Power Electronics*, vol. 33, no. 8, pp. 7094-7104, 2017.
[106] Y. Gui, R. Han, J. M. Guerrero, J. C. Vasquez, B. Wei, and W. Kim, "Large-signal stability improvement of DC-DC converters in DC microgrid," *IEEE Transactions on Energy Conversion*, vol. 36, no. 3, pp. 2534-2544, 2021.
[107] S. Fang, Y. Wang, B. Gou, and Y. Xu, "Toward future green maritime transportation: An overview of seaport microgrids and all-electric ships," *IEEE Transactions on Vehicular Technology*, vol. 69, no. 1, pp. 207-219, 2019.
[108] D. Park and M. Zadeh, "Modeling and predictive control of shipboard hybrid DC power systems," *IEEE Transactions on Transportation Electrification*, vol. 7, no. 2, pp. 892-904, 2020.
[109] J. Chen *et al.*, "Multi-timescale Reward-based DRL Energy Management for Regenerative Braking Energy Storage System," *IEEE Transactions on Transportation Electrification*, 2025.

[110] Y. Gu and D. Zhang, "Interleaved boost converter with ripple cancellation network," *IEEE transactions on power electronics*, vol. 28, no. 8, pp. 3860-3869, 2012.
[111] M. A. Hassan *et al.*, "DC shipboard microgrids with constant power loads: A review of advanced nonlinear control strategies and stabilization techniques," *IEEE Transactions on Smart Grid*, vol. 13, no. 5, pp. 3422-3438, 2022.
[112] M. Gutierrez, P. A. Lindahl, and S. B. Leeb, "Constant power load modeling for a programmable impedance control strategy," *IEEE Transactions on Industrial Electronics*, vol. 69, no. 1, pp. 293-301, 2021.
[113] A. M. Rahimi and A. Emadi, "Active damping in DC/DC power electronic converters: A novel method to overcome the problems of constant power loads," *IEEE Transactions on Industrial Electronics*, vol. 56, no. 5, pp. 1428-1439, 2009.
[114] W. Jiang, M. Wang, X. Li, Z. Xu, X. Zhang, and X. Wu, "Autonomous finite-time backstepping control for decentralized economic power dispatch in DC microgrids toward large-signal stability," *IEEE Transactions on Industrial Electronics*, vol. 71, no. 3, pp. 2942-2954, 2023.
[115] M. H. Khooban, M. Gheisarnejad, H. Farsizadeh, A. Masoudian, and J. Boudjadar, "A new intelligent hybrid control approach for DC–DC converters in zero-emission ferry ships," *IEEE Transactions on Power Electronics*, vol. 35, no. 6, pp. 5832-5841, 2019.
[116] C. Zheng, T. Dragičević, J. Zhang, R. Chen, and F. Blaabjerg, "Composite robust quasi-sliding mode control of DC–DC buck converter with constant power loads," *IEEE Journal of Emerging and Selected Topics in Power Electronics*, vol. 9, no. 2, pp. 1455-1464, 2020.
[117] S. Singh, D. Fulwani, and V. Kumar, "Robust sliding-mode control of dc/dc boost converter feeding a constant power load," *IET Power Electronics*, vol. 8, no. 7, pp. 1230-1237, 2015.
[118] Q. Xu, C. Zhang, C. Wen, and P. Wang, "A novel composite nonlinear controller for stabilization of constant power load in DC microgrid," *IEEE Transactions on Smart Grid*, vol. 10, no. 1, pp. 752-761, 2017.
[119] M. M. Mardani, M. H. Khooban, A. Masoudian, and T. Dragičević, "Model predictive control of DC–DC converters to mitigate the effects of pulsed power loads in naval DC microgrids," *IEEE Transactions on Industrial Electronics*, vol. 66, no. 7, pp. 5676-5685, 2018.
[120] H. Wang, W. Mingli, and J. Sun, "Analysis of low-frequency oscillation in electric railways based on small-signal modeling of vehicle-grid system in dq frame," *IEEE Transactions on Power Electronics*, vol. 30, no. 9, pp. 5318-5330, 2015.
[121] R. Wang, Q. Sun, D. Ma, and Z. Liu, "The small-signal stability analysis of the droop-controlled converter in electromagnetic timescale," *IEEE Transactions on Sustainable Energy*, vol. 10, no. 3, pp. 1459-1469, 2019.